Design of thermoelectric (TE) modules based on TE materials of higher specific figure-of-merit and low-cost materials

Hee Seok Kim

A dissertation
submitted in partial fulfillment of the
requirements for the degree of

Doctor of Philosophy

University of Washington

2013

Reading Committee:

Minoru Taya, Chair

Jaehyun Chung

Joyce Cooper

Program Authorized to Offer Degree:
Mechanical Engineering

University of Washington

Abstract

Design of thermoelectric (TE) modules based on TE materials of higher specific figure-of-merit and low-cost materials

Hee Seok Kim

Chair of the Supervisory Committee:
Professor Minoru Taya
Mechanical Engineering

The efficiency of thermoelectric (TE) materials is determined by the dimensionless figure-of-merit (ZT) defined as $ZT = S^2\sigma T/\kappa$ where, S, σ, κ, and T are Seebeck coefficient, electrical conductivity, thermal conductivity, and absolute temperature, respectively. For weight-sensitive applications the specific figure of merit defined as ZT divided by mass density, should be emphasized. Since Mg_2Si for n-type and higher manganese silicide (HMS, $MnSi_{2-x}, x = 0.250 \sim 0.273$) for p-type TE alloys have low mass densities, they produce a TE module with a high specific power suitable for airborne applications. To improve ZT by reducing lattice thermal conductivity, nanostructures are formed by mechanical alloying and spark plasma sintering techniques. Two TE module designs are made, (1) a segmented π-shape TE module and (2) a segmented linear TE module. The segmented π-shaped TE generator (TEG) is composed of higher temperature segments made of n-type Mg_2Si and p-type HMS, and lower temperature segments of n-type and p-type Bi-Te based compounds. The specific power density was measured as 42.9 $[W/kg]$ under $500\,^{\circ}C$ temperature difference, which has a good agreement with analytical predictions. The linear-shaped TEG is composed of AlN-Cu composite electrode integrated into the combustion chamber wall made of Fe based shape memory alloy (Fe-SMA) by shrink-fit joining. The power output of the linear TEG is found to be 7% higher than that of the π-shaped TEG, and the specific power density is increased from 42.9 $[W/kg]$ to 89.3 $[W/kg]$ due to lighter weight of the linear design. The maximum shear stress of the linear TEG is reduced by 47% compared with the π-shaped TEG. As a result, the linear TEG proposed gives rise to better performance in terms of the specific power density, while it is more robust.

TABLE OF CONTENTS

LIST OF FIGURES

LIST OF TABLES

ACKNOWLEDGMENTS

I express sincere thanks and gratitude to my advisor Dr. Minoru Taya for giving me an opportunity on a thermoelectric research with his unconditional support, invaluable guidance, patience and motivation throughout my doctoral program. This research was supported by NASA-JPL (#1292175), AFOSR MURI to the University of Washington (FA9550-06-01-0326) and AFOSR DURIP (FA9550-09-01-0587).

I wish to say thanks to the former postdoctoral fellows in CIMS, Dr. Keiko Kikuchi, Dr. Miseon Choi, and Dr. Weishu Liu for guiding my research and helping me to develop my background, and Dr. Onur Namli for discussion about operations of the equipments in CIMS. I would like to thank a visiting scholar, Dr. Yasuo Kogo at Tokyo University of Science for his encouragement, and a visiting student, Mr. Akinori Ohta at Nippon University for his help of high temperature brazing.

I am thankful to Dr. Yoshinano Mishima and Dr. Yoshisato Kimura in Material Science Engineering at Tokyo Institute of Technology (TIT) for inviting me as a visiting researcher by a support of their Foreign Young Research Program, and also thankful to Dr. Yaw Wang Chai for training me how to operate TEM in TIT.

I would also thank to my family and my wife, Jae Won. Especially, my father always encourages me while he is fighting against cancers. Without them, my PhD degree could not be completed.

I will forever be thankful to my former college advisor, Dr. Ja Choon Koo. He is my best role model and enabled me to pursue a career in research.

I express my special gratitude to all my committee members, Dr. Jaehyun Chung, Dr. Joyce Cooper, and Dr. Christine Luscombe.

NOMENCLATURE

Roman symbols

A	Cross sectional area of TE segment
C_p	Specific heat capacity
d	Mass density
I	Electric current
K	Thermal conductance
K^M	Effective thermal conductance of a TE module
L	Length of TE leg
L_0	Lorentz number
m	Ratio of R_L to R_{tot}
N	The number of pairs of n-type and p-type TE legs
n	n-type
P	Output power
p	p-type
P_{max}	Maximum output power

Q	Heat flux
R_L	Load resistance
R_{TE}	Total electric resistance of TE materials
R_{th}	Thermal resistance
R_{tot}	Total electrical resistance of TE module
R_{tot}^M	Effective electrical resistance of 1-pair
R_w	Electric resistance of lead wires
S^M	Effective Seebeck coefficient of a TE module
T	Absolute temperature
T_{Af}	Austenite finish temperature
T_{As}	Austenite start temperature
T_C	Cold-side temperature
T_H	Hot-side temperature
T_{in}	Interface temperature between TE segments
T_{Mf}	Martensite finish temperature
T_{Ms}	Martensite start temperature
V_n	Voltage generated by n-type TE leg
V_{OC}	Open circuit voltage

V_p	Voltage generated by p-type TE leg
Z^M	Module figure of merit
ZT	Dimensionless figure of merit

Greek symbols

α	Thermal diffusivity
η	Efficiency of TE module
κ	Thermal conductivity
κ^E	Effective thermal conductivity of combined TE segments
κ_{el}	Thermal conductivity by electron
κ_{ph}	Thermal conductivity by phonon
Π	Peltier coefficient
ρ	Electrical resistivity
σ	Electrical conductivity
τ	Thomson coefficient

Subscript

1	TE segment of high temperature side
2	TE segment of low temperature side
c	Contact layer

i	i^{th} TE segment
n	n-type TE material
p	p-type TE material
sub	Substrate layer

ACRONYM

AlN	Aluminum Nitride
CTE	Coefficient of Thermal Expansion
DSC	Differential Scanning Calorimeter
EDS	Energy Dispersive Spectroscopy
FEA	Finite Element Analysis
FFT	Fast Fourier Transform
FIB	Focused Ion Beam
HMS	Higher Manganese Silicide
HRTEM	High Resolution Transmission Electron Microscope
IFFT	Inverse Tast Fourier Transform
LAST	Lead-Antimony-Silver-Tellurium based alloy
MA	Mechanical Alloying
MAV	Micro Aerial Vehicles

PCA	Process Control Agent
SAD	Selected Area Diffraction
SCCM	Standard Cubic Centimeter per Minute
SEM	Scanning Electron Microscope
SMA	Shape Memory Alloy
SPS	Spark Plasma Sintering
STEM	Scanning Transmission Electron Microscope
TAGS	Tellurium-Antimony-Germanium-Silver based alloy
TEG	Thermoelectric Generator
TEM	Transmission Electron Microscope
UAV	Unmanned Aerial Vehicles
WC	Tungsten Carbide
XRD	X-ray Diffraction

Chapter 1

INTRODUCTION

1.1 Basic phenomena

1.1.1 Seebeck effect

In 1821, Thomas Johann Seebeck found that a circuit made from two dissimilar metals with junctions at different temperatures would deflect a compass needle [1]. This is caused by a response to the magnetic field when current flows through the circuit, *i.e.*, the temperature difference produces electric potential which can drive an electric current in this closed circuit, which is known as Seebeck effect. Fig. 1.1 illustrates the open circuit composed of two dissimilar materials where temperature difference is applied at each junction. The open circuit voltage is given as,

$$V = \int_{T_C}^{T_H} (S_A(T) - S_B(T))\, dT \tag{1.1}$$

where, $S_A(T)$ and $S_B(T)$ are Seebeck coefficient of material A and B, respectively, in unit of Volt per Kelvin (V/K). Assuming that Seebeck coefficient is independent of temperature, Eq. 1.1 can be written as,

$$V = (S_A - S_B)(T_H - T_C) \tag{1.2}$$

Eq. 1.2 shows that an increase in the difference between Seebeck coefficients or a larger temperature difference will increase the open circuit voltage.

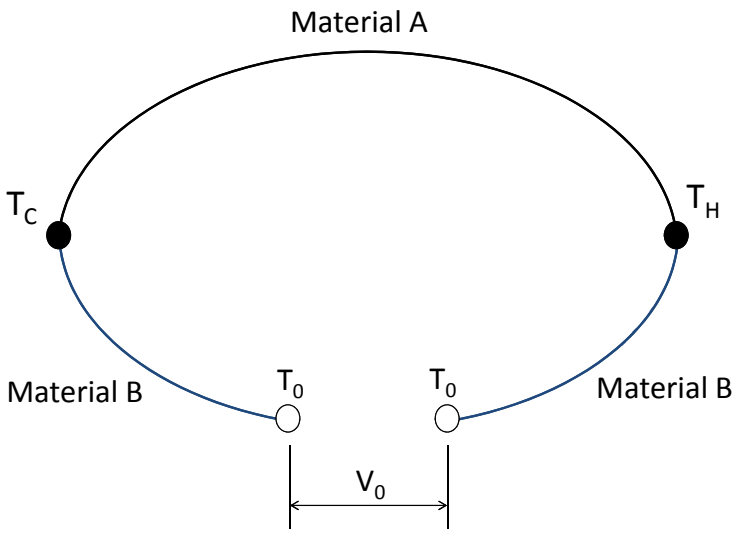

Figure 1.1: Seebeck effect: two dissimilar materials forms an open circuit

1.1.2 Peltier effect

In 1834, Jean Charles Athanase Peltier found that an electrical current would produce heating or cooling at the junction of two dissimilar metals [2]. The direction of the heat flow at junctions depends on the direction of the applied electric current. The heat absorbed or liberated at the junction is proportional to the electrical current. Fig. 1.2 shows a schematic figure of Peltier effect.

Assuming that the electrical resistance of a junction is ignored, the amount of Peltier heat liberated by the hot junction, q_H is given by,

$$q_H = (\Pi_A - \Pi_B)I = \Pi_{AB}I \tag{1.3}$$

where, Π_A and Π_B are the Peltier coefficient of material A and B, respectively, in unit

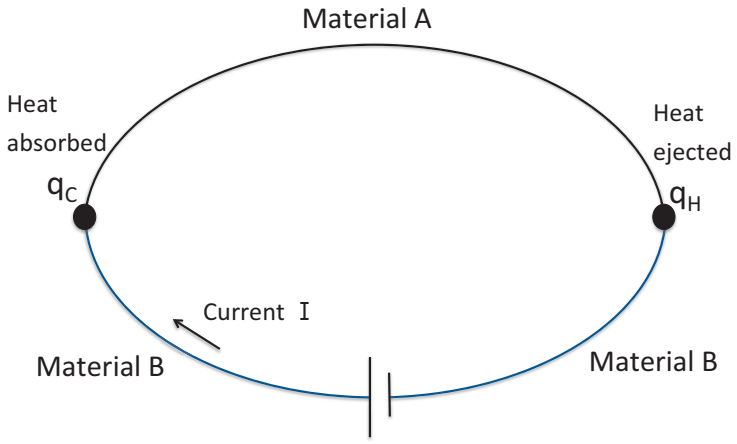

Figure 1.2: Peltier effect: two dissimilar materials are formed in a closed circuit

of Watt per Ampere (W/A).

1.1.3 Thomson effect

In 1855, William Thomson, who later became Lord Kelvin, described the interrelationship of Seebeck and Peltier effect, which is that the Seebeck coefficient is the ratio of Peltier coefficient to absolute temperature, see Eq. 1.4.

$$S_{AB} = \frac{\Pi_{AB}}{T} \tag{1.4}$$

The heat is absorbed or dissipated when current flows in a material with a temperature gradient as shown in Fig. 1.3, and it has two terms: Joule heating and Thomson heating, shown in Eq. 1.5 [3].

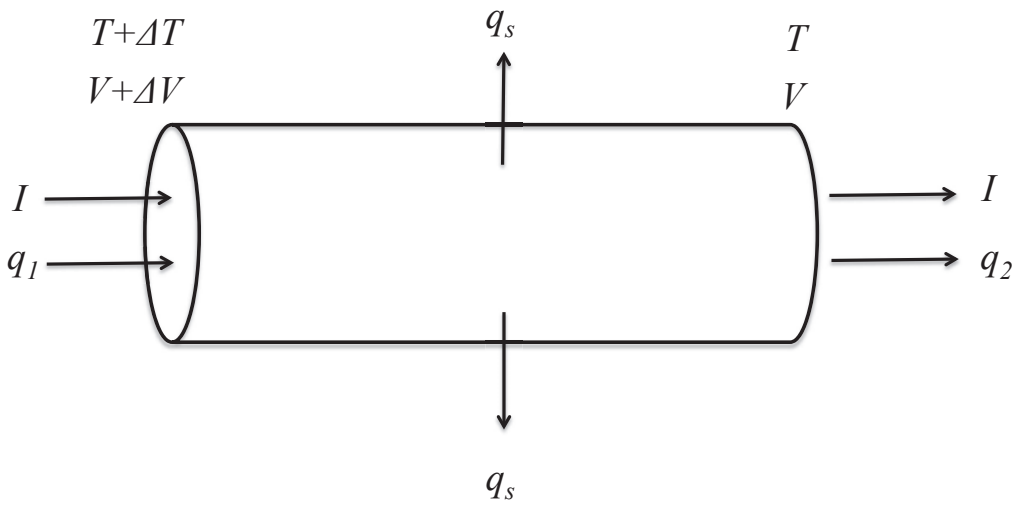

Figure 1.3: Thomson effect: A heat current and an electric current flowing in a homogeneous material in which there is a temperature gradient

$$q_s = I^2R - IT\frac{dS}{dT}\Delta T \tag{1.5}$$

The Thomson heat is proportional to both the electric current and the temperature gradient, so the proportional constant is defined as Thomson coefficient, τ shown in Eq. 1.6, and usually defined positive if heat must be added to keep temperature the same [3].

$$\tau = -T\frac{dS}{dT} \tag{1.6}$$

TE effects have been re-enlightened since Russian scientist, Abram Fedorovich Ioffe, developed the modern TE theory introducing semiconductor physics to improve TE performance [4]. H. Julian Goldsmid demonstrated $0\,^{\circ}C$ of cooling in 1954 by using Bi_2Te_3 based

TE compound [5], and showed that low lattice thermal conductivity (κ_{ph}) can improve the performance of TE materials by proper doping in semiconductors [6]. The research of bulk TE materials mainly followed the concept of 'Phonon Glass and Electron Crystal' which means that the phonon mean free path are as short as possible like in a glass while the electron mean free path are as long as possible like in a crystalline semiconductors [7].

1.2 Motivation

TE phenomena involve the direct conversion between thermal and electrical energy. Since TE energy conversion is all solid-state technology, it has unique advantages such as high reliability, no vibration and quiet operation [8]. With these advantages, TE devices have been used in a wide range of applications from temperature measurement to waste heat recovery and refrigeration [9, 10, 11]. A typical design of TE module device for power generation consists of n-type and p-type TE legs which are connected electrically in series and thermally in parallel as shown in Fig. 1.8 (a). The n-type and p-type TE legs are joined by metal electrodes, and the as-assembled series of $n-p$ TE legs are covered with ceramic plates on top and bottom, which are thermally conductor and electrically insulator to avoid a short circuit. The assembled TE module device is placed in between a heat source and a heat sink. The maximum efficiency of the TE generator (TEG) can be obtained when the external load resistance is matched with the internal resistance of TEG as [3],

$$\eta_{max} = \frac{T_H - T_C}{T_H} \frac{\sqrt{1+ZT_m}-1}{\sqrt{1+ZT_m}+\frac{T_C}{T_H}} \tag{1.7}$$

where, T_H and T_C are temperatures of a heat source (hot side) and a heat sink (cold side), respectively, and T_m is the average temperature of T_H and T_C. ZT_m is the efficiency of TE

materials at the average temperature, T_m. The efficiency of the TE materials is determined by the dimensionless figure-of-merit (ZT) defined as [3]

$$ZT = \frac{S^2\sigma}{\kappa}T \tag{1.8}$$

where, S, σ, κ, and T are the Seebeck coefficient, the electrical conductivity, the thermal conductivity which is a sum of lattice (κ_{ph}) and carrier (κ_{el}) component, and the absolute temperature at which the properties are measured, respectively. As shown in Eq. 1.7, since the maximum efficiency of TEG module is a function of ZT consisting of TE material properties, ZT is a key parameter for higher efficiency of a TE module device. To improve the ZT of TE materials, larger values of Seebeck coefficient and electrical conductivity are desired to maximize power factor ($S^2\sigma$), and lower thermal conductivity are required. However, it is difficult to control these physical properties independently because an increase of electrical conductivity usually decreases Seebeck coefficient, and increases thermal conductivity by Wiedemann-Franz law, $\kappa_{el} = L_0\sigma T$, where L_0, σ and T are Lorentz number, electrical conductivity and absolute temperature, respectively.

To enhance ZT, many approaches have been studied. New bulk TE materials have been studied such as Tl_9BiTe_6 [12], clathrate $(Ba,Sr)_8(Al,Ga)_{16}(Si,Ge,Sn)_{30}$ [13], PbTe-PbS [14], $CsBi_4Te_6$ [15], $AgPb_mSbTe_{2+m}$ (LAST) [16], $In_4Se_{3-\delta}$ [17], Tl-doped PbTe [18], $In_4Se_{3-x}Cl_{0.03}$ [19], $Cu_xBi_2Te_{2.7}Se_{0.3}$ [20], PbTe-SrTe [21], $Ba_uLa_vYb_wCo_4Sb_{12}$ [22], Cu ion liquid-like $Cu_{2-x}Se$ [23], $Cu_2Ga_xSn_{1-x}Se_3$ [24], and $(Ba,Sr,DD,Yb)_y(Fe_{1x}Ni_x)_4Sb_{12}$ [25]. Another approach is to reduce the dimension of materials. In order to increase power factor Hicks *et al.* suggested that the power factor ($S^2\sigma$) can be enhanced and κ_{ph} can be reduced by using the quantum-confinement effects [26, 27]. Dresselhaus *et al.* enlightens various low dimension systems including superlattice, nanowire, and quantum dots [28]. Recently, ZT enhancement was achieved in bulk nanocomposites consisting of three-dimensional nanograins [29, 30, 31] based on an idea of minimizing κ_{ph}. By generating a high den-

sity of grain boundary interfaces, phonon scatters more intensively than charge carries, which gives rise to decreasing κ_{ph}.

The ZT values of 2.0 in Lead-Antimony-Silver-Tellurium based material (LAST) [16], and 2.4 in Bi_2Te_3/Sb_2Te_3 supperlattice have been reported [32]. These alloys are good TE materials for energy conversion systems to harvest the waste heat energy from industries, civil activities, and transportation. However, the majority of research on thermoelectrics is aimed at increasing the ZT value without considering other factors such as the weight, cost-effectiveness, environmental damage, and ease of mass production. For weight sensitive applications like ground or air vehicles the specific figure of merit, defined as ZT divided by mass density, should be emphasized. In addition, many TE compounds use expensive materials such as the rare earth element Tellurium (Te), which is one of the key components in TE system, and Ag in the LAST alloy and Ge in Tellurium-Antimony-Germanium-Silver (TAGS) alloy, resulting in an increased cost of final device. Moreover, compounds consisting of Pb or Te are classified as toxic materials [33]. Regarding manufacturing, low-dimension systems using a thin film processing such as supperlattice or quantum dot technology have challenges to scale up module devices as well as the mass production. For these reasons, it is necessary to study bulk TE alloys based on light-weight and low-cost materials without toxic elements.

1.3 Design of TE materials

To design TE system to apply into the weight-sensitive applications such as Unmanned Aerial Vehicles (UAV) or Micro Aerial Vehicles (MAV), following factors should be considered.

- Intermediate target temperature range of the operation: $300 \sim 600\,^{\circ}C$
- Specific figure of merit: ZT/mass density

TE materials	Density $[g/cm^3]$	ZT	Specific ZT $[ZT/\text{density}]$	Cost [1998USD/kg]
Bi_2Te_3[35]	7.86	1.4 (at 100 °C)	0.178	91.2
Zn_4Sb_3[36]	6.08	1.3 (at 400 °C)	0.214	4.4
HMS[37]	5.24	0.47 (at 600 °C)	0.090	2.4
$AgPb_{18}SbTe_{20}$[16]	8.08	2.2 (at 527 °C)	0.272	59.9
$CoSb_{3-x}Te_x$[38]	7.62	0.93 (at 537 °C)	0.122	72.2
doped Mg_2Si[39]	2.36	1.08 (at 577 °C)	0.380	5.2
SiGe[31]	2.93	0.95 (at 800 °C)	0.324	586.3

Table 1.1: Specific figure-of-merit of bulk TE materials and material cost [1998USD/kg] estimated by using cost data in 1998

- cost-effectiveness
- non-toxicity

Fig. 1.4 shows the state-of-art TE alloys of n-type and p-type in terms of ZT at its operating temperature. Pb/Sb/Ag/Te (LAST), Pb-Te based alloys, Zn_4Sb_3, Co-Sb based alloy and Mg-Si alloys show high performance at the intermediate temperature range of $300 \sim 600\,°C$. These materials can be converted onto a figure in terms of mass density vs. maximum ZT, which is shown in Fig. 1.5 re-plotted based on Fig. 1.4. Most TE alloys having the best performance between $300\,°C$ and $600\,°C$ are heavy alloy systems while Mg-Si is positioned on the left side giving 2 to 3 $[g/cm^3]$ of mass density. Even though Mg-Si compound generates relatively low ZT performance compared with other heavy alloy systems, it can return a larger value of energy conversion performance per unit mass among them.

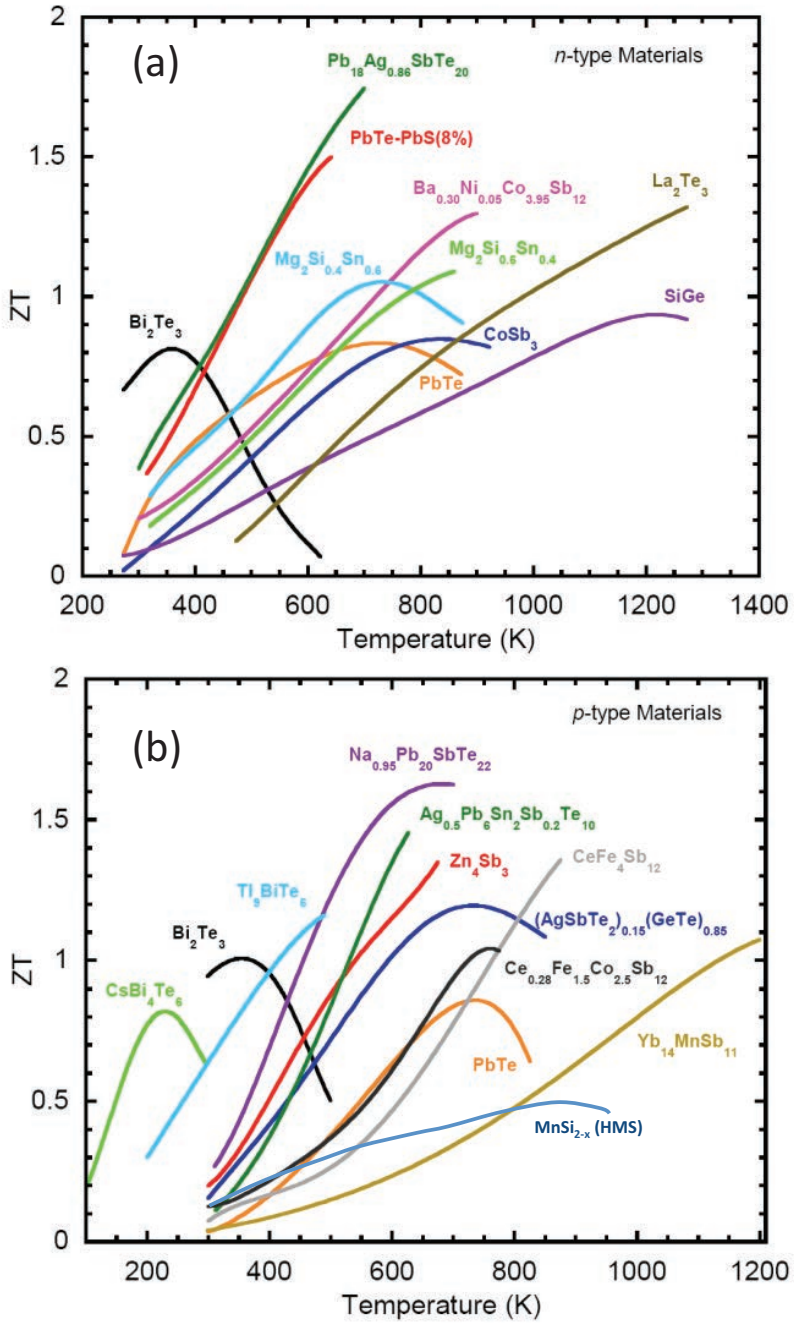

Figure 1.4: The state-of-art TE alloys with ZT vs. Temperature: (a) n-type and (b) p-type alloys [34]

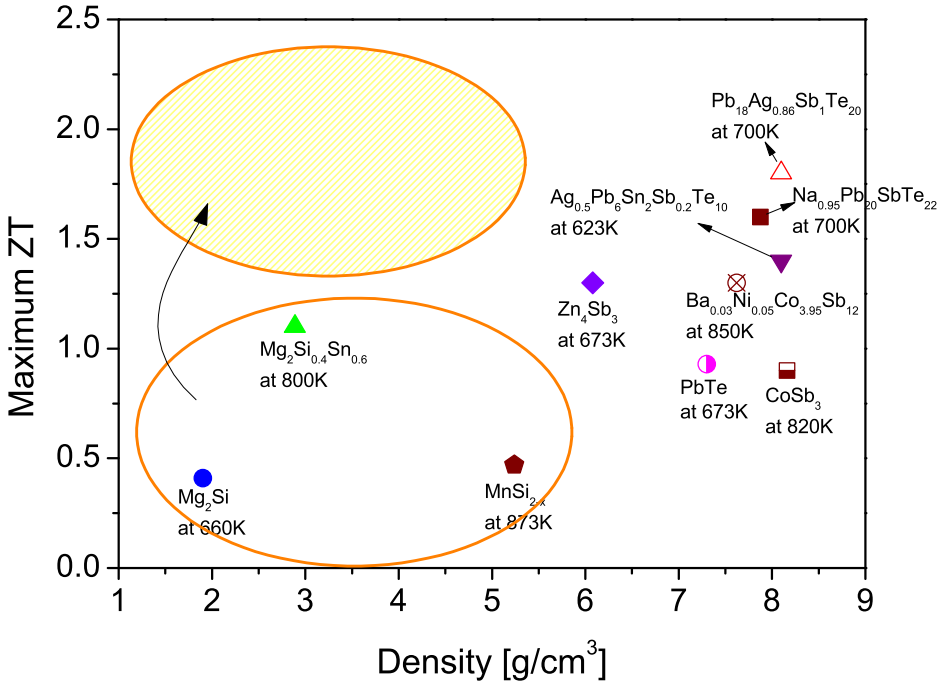

Figure 1.5: Mass density vs. maximum ZT of the state-of-art TE materials

Rank	Atom	Clarke No.	Rank	Atom	Clarke No.
2	Si	29.5	53	Ge	1.4×10^{-4}
8	Mg	1.87	59	Sb	5×10^{-5}
9	Mn	0.1	66	Ag	0.7×10^{-5}
19	Zn	8.3×10^{-3}	68	Bi	0.9×10^{-6}
33	Co	1.8×10^{-3}	70	Te	0.1×10^{-6}

Table 1.2: The list of popular TE elements with Clarke numbers [40]

Table 1.1 compares popular TE materials in terms of specific figure of merit [ZT/mass density] and cost [1998USD/g], where the cost data of each material in 1998 are used [41]. ZT value over 2 in $AgPb_{18}SbTe_{20}$ system is reported [16], but due to its high mass density ($8.08g/cm^3$) the specific figure-of-merit is lower than that of Mg_2Si and SiGe alloys which are light compounds with low density below 3 [g/cm^3]. Other common TE compounds such as Bi_2Te_3 and $CoSb_{3-x}Te_x$ have even lower specific figure-of-merit than Mg_2Si although their ZT are high values of 1.4 and 0.93, respectively. Thus, in terms of the specific figure-of-merit, Mg_2Si is suitable for intermediate temperature up to $600\,^{\circ}C$ and SiGe is good candidate working for high temperature applications at $1000\,^{\circ}C$.

As considering cost-effectiveness, the Clarke number can be a factor to judge its economic feasibility based on its abundance. Clarke number is the wt % of abundance in the crust on earth, so higher number indicates the possibility of reducing the cost of materials. Clarke number of each element commonly used in TE system is listed in Fig. 1.2. According to the Table 1.2, Si, Mg and Mn are in the group of most common element ranked in 2^{nd}, 8^{th} and 9^{th}, respectively, while key materials of high performance TE compounds such as Sb, Bi, Ag and Te are classified as less abundant elements with low Clarke index. It is true that the abundance is not the only critical parameter to decide the cost of raw materials because a purification process and handling procedure even including a political situation should be considered. Fig. 1.6 and Fig. 1.7 illustrate the unit cost fluctuating for last 40 years, where the cost data of each year are estimated by using 1998 US dollar values [41]. Mg, Zn and Si have been stable and as low as 5 [$\$/kg$] over 40 years while Sn, Bi and Sb have an increasing trend. In Fig. 1.7 (a), Te is expensive by a factor of 10 as compared to other materials shown in Fig. 1.6. The most expensive element used in TE compounds is Ge whose price trend is shown in Fig. 1.7 (b). Even though the abundance of Ge is more than Te and Bi, the price of Ge is much higher than those due to its complicated processing. Thus, Si based TE compounds such as Mg_2Si and higher manganese silicide (HMS) are the best candidates with regard to cost-effectiveness.

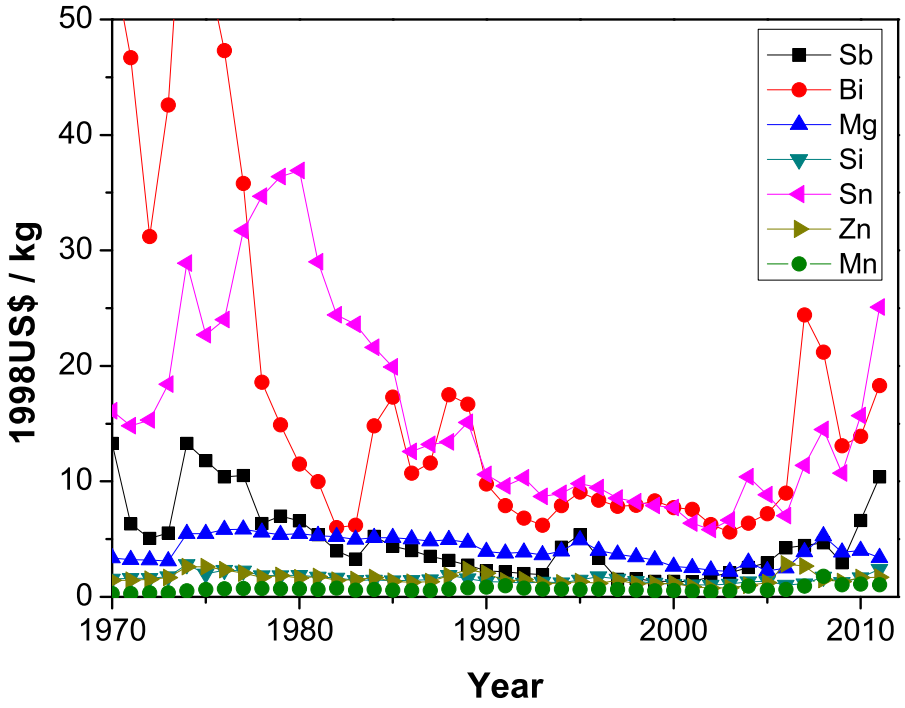

Figure 1.6: Commodity price of common TE materials, where the cost data of each year are adjusted to a base year of 1998

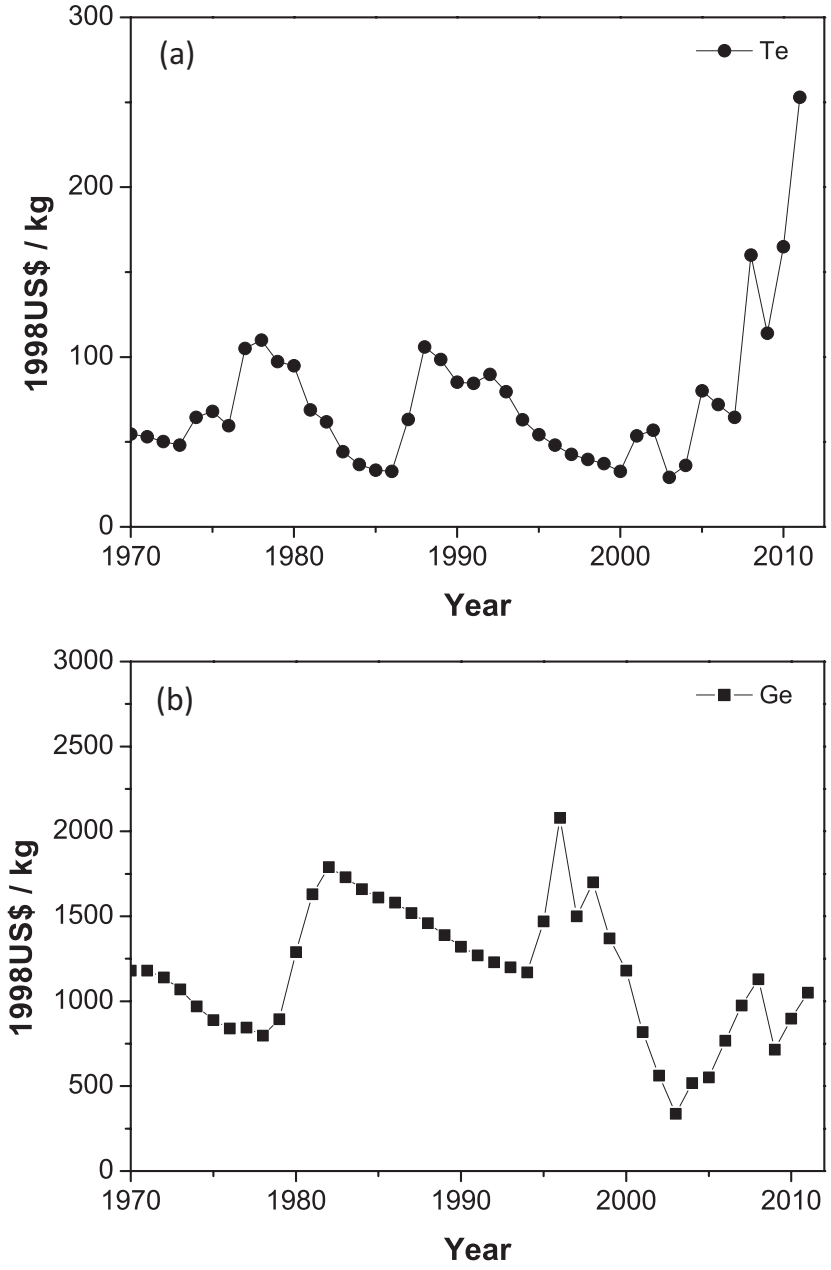

Figure 1.7: Commodity price of expensive elements: (a) Tellurium and (b) Germanium, where the cost data of each year are adjusted to a base year of 1998

Non-toxic system is one of the important requirements for the future energy recovery industry. Most TE systems returning high ZT values are a type of alloys including either Te or Pb shown in Fig. 1.4 and Table 1.1. Pb is well known toxic element, and it is also reported that Te compounds are classified as poison materials [33]. Non-toxic TE alloys working at the intermediate temperature range excluding both Te and Pb toxic elements are Mg_2Si, Zn_4Sb_3 and HMS compounds, which are also in the group showing high specific figure-of-merit and using low-cost based materials.

Considering all requirements discussed above, the most suitable TE compound for n-type is Mg_2Si. With regard to p-type compounds Zn_4Sb_3 and HMS can be a good candidates to assemble $n-p$ pair for TEG module device by using light-weight, cheap and toxic-free raw materials. However, El-Genk *et al.* [42] reported that the sublimation behavior of Sb occurred above $327\,^{\circ}C$, which degrades ZT performance. In addition, the cost of Sb as shown in Fig. 1.6 has an increasing trend recently. Therefore, Mg_2Si and HMS are the best TE materials as n-type and p-type, respectively, for the weight sensitive applications.

1.4 Design of TE generator module

Various types of TE modules are shown in Fig. 1.8. The conventional design is single-stage couples connecting electrically in series and thermally in parallel with π shape (Fig. 1.8 (a)). The typical TE module is made by connecting N pairs of n-type and p-type TE legs, which gives rise to the output voltage proportional to N. However, the use of single legs of TE materials in the module is inefficient to work at both high and low temperature side when a large temperature difference ΔT is applied, ($\Delta T = T_H - T_C$).

Harman [43] suggested the cascaded design shown in Fig. 1.8 (b), in which the bottom TE module generates electric power from the heat rejected by the top module. This design has a disadvantage for weight sensitive applications because an extra ceramic substrate and metal electrodes increase the total weight of the device. One way to improve the TE performance as well as to minimize the total weight of the device is the segmented design by

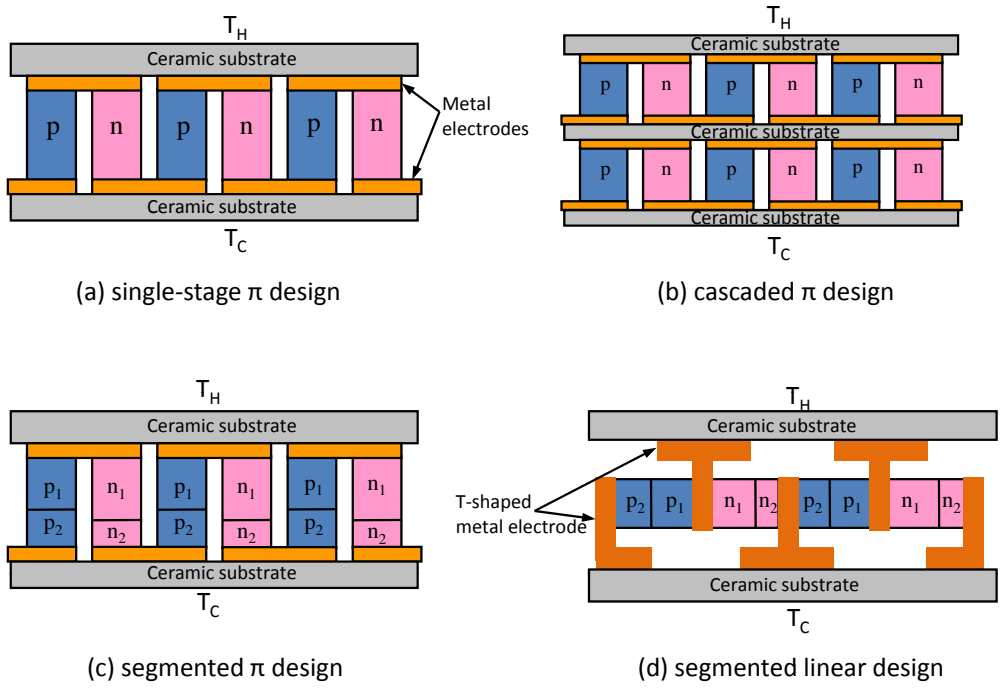

Figure 1.8: Various design concepts of TEG module device: (a) conventional single-stage π shaped module, (b) cascaded π shaped module, (c) segmented π shaped module, and (d) segmented linear module design

dividing the n-type and p-type legs into several segments of different TE materials [44, 45]. Fig. 1.8 (c) shows two-segmented TE module device, where the subscript 1 and 2 means TE materials working at high temperature and low temperature, respectively [3, 46]. However, the π shaped planar structure becomes unstable if the length of n-type and p-type TE column is not identical, which makes the module weak at high temperature environment. Stockholm [47] introduced a linear structure in which the length of each n-type and p-type can be varied. In addition, parasitic electrical resistance of the linear design can be reduced since its electric current flows in a straight line through the TE elements while the electric current in planer π shaped design passes alternatively up and down.

1.5 Research Plan

The objective of this study is to design TEG integrated into combustion engine system in UAV. For this application, n-type Mg_2Si and p-type HMS are incorporated into TEG modules to improve the UAV's efficiency since Si based Mg_2Si and HMS are not only cheap and non-toxic compounds, but also light-weight alloys with low mass density. This work consists of,

- Synthesizing nanostructred bulk n-type Mg_2Si to improve ZT performance
- Fabricating segmented π shaped TEG
- Designing an advanced segmented linear shaped TEG
- An innovative integration method using shrink-fit joining by using shape memory alloy

With regard to generating nanostructres in bulk TE materials, the advanced metallurgical route is carried out with the combination of high energy mechanical alloying (MA) process using planetary ball milling (PM100, Retsch) shown in Fig. 1.9 and rapid sintering process using spark plasma sintering (SPS) technique (Dr. Sinter 1020S, Sumitomo

Coal Mining Co., Ltd.) shown in Fig. 1.10. The high energy milling process generates nano sized alloyed particles, and forms sub-grain boundaries. To avoid any contamination and oxidation of as-processed nano particles, all handling of powders is carried out in a glove box system shown in Fig. 1.11. The strategy of this study to improve ZT value is the decreasing of thermal conductivity by the lattice component (κ_{ph}) since the thermal conductivity by carrier component (κ_{el}) and electrical conductivity are interdependent by Wiedemann-Franz law. Thanks to rapid sintering technique, SPS process suppresses the growing of grains during the solidification at high temperature, so the nanostructures in bulk TE materials enable phonon to scatter intensively through the compact grain boundaries, which results in decreasing the κ_{ph}.

To generate nanostructures, the effect of MA parameters such as ball composition, grinding medium selection, wet alloying condition, and milling speed and time are investigated, and then the optimization of SPS process is performed to obtain highly dense bulk materials and minimize grain growth. The characterization of micro/nano structures of the alloyed powders and bulk as-sintered materials is carried out via XRD/SEM/TEM. The thermal diffusivity and the specific heat capacity are measured simultaneously by laser flash measurement system (TC-9000, Ulvac-Rico, Fig. 1.12), and Seebeck coefficient and electrical conductivity are measured at the same time by four-point probe equipment (ZEM-3, Ulvac-Rico, Fig. 1.13). The optimization of MA and SPS process and characterization are shown in Chapter 2 in details.

Next, two-segmented π shaped TEG is fabricated based on Mg_2Si collaborating with Prof. Iida at Tokyo University of Science and HMS ($MnSi_{2-x}$, x=0.250∼0.273) collaborating with Prof. Itoh at Nagoya University for high temperature TE segments. The lower temperature TE legs of commercial Bi-Te based compounds (Tellurex Inc.) are used. Even though Bi-Te compounds are heavy alloy and including toxic element, they are utilized in this study as low temperature TE segments since no TE alloys are competitive with them working at room temperature. Contact resistance, a key factor in determining the output power of segmented TE module design, is studied. In addition, a more realistic model is dis-

Figure 1.9: Planetary ball milling equipment (PM100, Retsch)

Figure 1.10: Spark plasma sintering equipment (Dr. Sinter 1020S, Sumitomo Coal Mining Co., Ltd.)

Figure 1.11: box system at Ar atmosphere

cussed for the segmented TE module with all interface resistances being accounted for, and the analytical prediction is then compared with experimental data. All details of assembling two-pair π shaped TEG and testing its performance are described in Chapter 3.

Lastly, an innovative design based on the segmented linear TE structure is proposed to integrate TEG modules into a combustion engine system in UAV. The key part of the new TE design is T-shaped composite electrode composed of aluminum nitride (AlN) in a dovetail-shape at an upper portion and copper (Cu) block as a bottom part. The combined T-shaped electrode replaces Cu electrodes as well as large ceramic plates in π shaped TE design so that this linear design using the compositive T-shaped electrodes further reduces the total weight of the TE module device than that of the π shaped TE structure. Regarding an issue for integration into airborne applications, linear shaped TEG is directly embedded into the wall of combustion chamber by using Fe based shape memory alloy (Fe-SMA), which is explained in details in Chapter 4.

Figure 1.12: Laser flash measurement system: Thermal diffusivity and specific heat capacity are measured simultaneously (TC-9000, Ulvac-Rico)

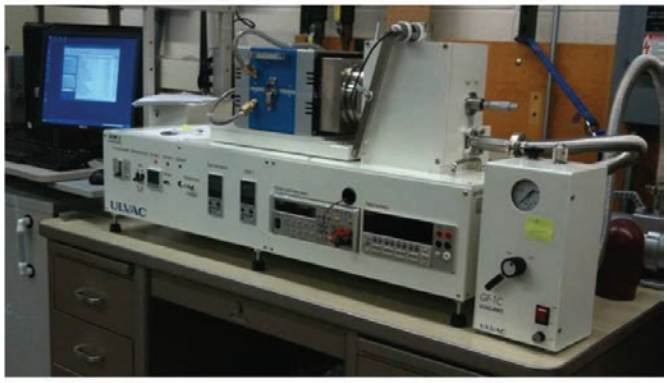

Figure 1.13: Four-point probe system: the measurement of Seebeck coefficient and electrical conductivity (ZEM-3, Ulvac-Rico)

Chapter 2

FABRICATION OF TE MATERIALS

In this chapter, the fabrication process of nanostructured Mg_2Si alloy and its characterization are described. The goal is the successful solidification of nanoparticles while minimizing grain growth to preserving their nanostructures. The first part of this chapter describes the strategy for ZT improvement by minimizing κ_{ph}, and the selection of processing route via MA and SPS compared with other methods. Both low-temperature alloying route and rapid sintering process are required since it is difficult to synthesize Mg_2Si alloy by the conventional direct melting method due to large difference of their melting point. In the second part, parametric study to optimize the processing conditions of MA and SPS is investigated. The last part discusses TE properties of bulk Mg_2Si based n-type materials.

2.1 Strategy for ZT improvement

In order to improve ZT value, reducing thermal conductivity is one of the promising strategies for bulk TE alloy system as mentioned in Chapter 1. This is required to reduce grain size up to nano scale to enhance phonon scattering intensively resulting in the reduction of κ_{ph}. However, conventional processing methods for bulk alloys have a difficulty in fabricating bulk TE materials because of growing grains during solidification process. It is investigated that bulk TE materials prepared via planetary ball milling [48], which enlightens the high energy MA technique generates large quantities of nanoparticles, and advanced hot-pressing technique can suppress the grain growth compared to traditional sintering method. The idea is that nanograins produced by high energy MA process and SPS technique can preserve a high density of grain boundary interfaces, which scatter phonon more effectively than charge carrier, and result in the reduction of the κ_{ph}. Based on this

Materials	Type	ZT	κ $[W/mK]$	Reference
$(Bi,Sb)_2Te_3$	p	1.4 at 100 °C	1.1	[29]
$Si_{80}Ge_{20}P_2$	n	1.3 at 900 °C	2.5	[30]
$Si_{80}Ge_{20}B_x$	p	0.95 at 800∼900 °C	2.5	[31]
$Bi_2(Te,Se)_3$	n	0.5 at 20 °C	1.0	[49]
$Yb_{0.35}Co_4Sb_{12}$	n	1.2 at 550 °C	1.52	[50]
$Fe_{1.5}Co_{2.5}Sb_{12}$	p	0.32 at 327 °C	2	[51]
$GaSb_{10}Te_{16.5}$	p	0.98 at 209 °C	1.0	[52]
$Ag_{0.8}Pb_{22}SbTe_{20}$	n	1.37 at 400 °C	0.9	[53]

Table 2.1: ZT values and thermal conductivities of some bulk nanocomposites

method, thermal conductivities of nanostructured bulk TE materials and their ZT values are listed in Table 2.1.

Various methods to fabricate TE materials based on Mg_2Si compound are shown in Fig. 2.1. A typical approach is that starting materials are directly alloyed by high temperature melting process, and then the processed ingot is transferred to bulk crystals grown by a vertical Bridgman method [54, 55] described in Fig. 2.1 (a), or synthesized alloy is obtained by a long time annealing process [56, 57], which is shown in Fig. 2.1 (b). However, it is difficult for this method to control the molar ratio of Mg and Si accurately because the boiling point of Mg is lower than the melting point of Si. It is also hard to prevent chemical reactions with constituents of crucibles, which degrades TE performance of contaminated alloy. For these reasons, the optimization of excessive Mg contents and a specific crucible to avoid contamination are required to use this method. To overcome disadvantages of high temperature melting methods, some direct reaction techniques has been studied such as

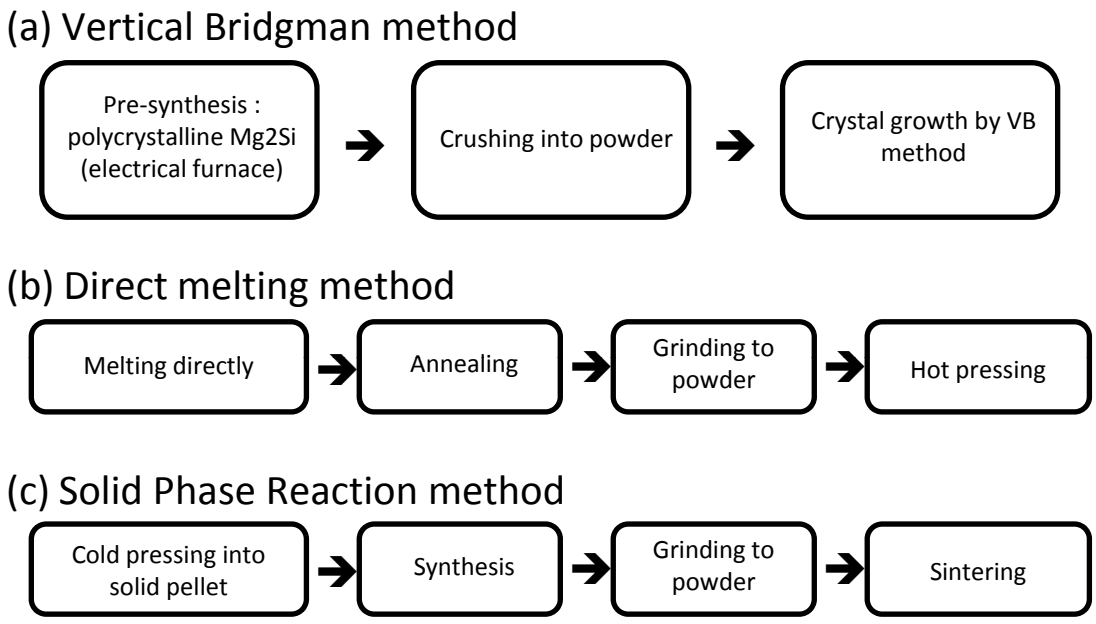

Figure 2.1: Various approaches for Mg_2Si synthesis: (a) vertical Bridgeman method, (b) typical direct melting route and (c) solid phase reaction method at lower temperature process

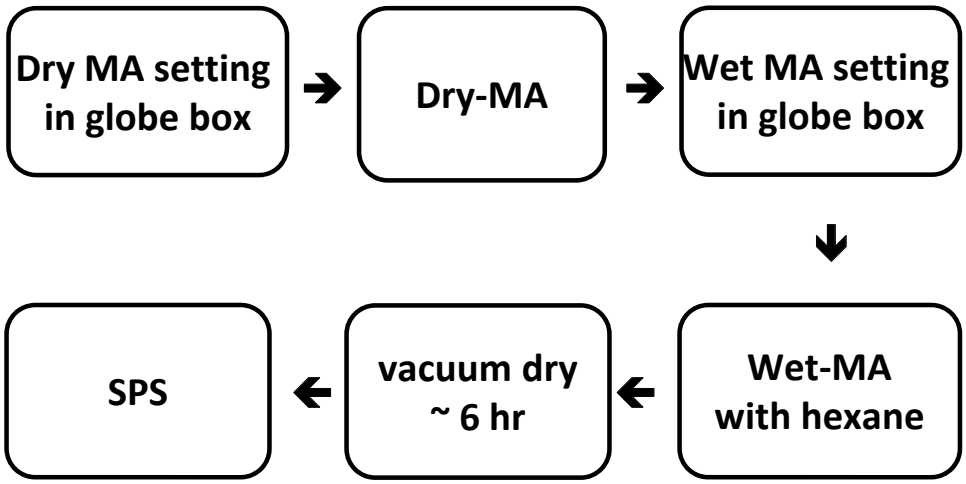

Figure 2.2: Overall processing route of fabrication procedure of nanostructured TE materials

liquid-solid reaction [56] and solid phase reaction [58]. Fig. 2.1 (c) shows typical steps for solid phase reaction technique. These direct reactions are carried out at lower temperature than that used in melting process shown in Fig. 2.1 (a) and (b), but they still need longer processing time and multi-steps to finalize the complete reaction. In addition, the volatilization of Mg is still inevitable due to its high vaporizing pressure, which makes it difficult to control the exact molar ratio in this method as well.

Since the synthesizing driven by high temperature method has challenges to produce Mg_2Si with the exact chemical compositions, the method by using mechanical force has been paid attention. The combination of high energy MA and SPS is a very promising technique because of the low temperature as well as rapid process. However, a few researches have been reported that the alloying of Mg_2Si via grinding technique followed by SPS process [59, 60] since fine magnesium particles are flammable elements when it is exposed to air. It is even more dangerous when nano sized powders are yielded by high energy MA

route. The glove box system is required to protect the flammable powers from oxidation and other contamination. Fig. 2.2 is an overall flow chart of the proposed process of synthesizing nanostructured TE alloys via MA combined with SPS process. All steps of alloying processing are carried out under Ar atmosphere. The alloyed powders after wet grinding process are dried in vacuum environment in the antechamber of glove box, and the assembly of graphite die and nanostructured alloyed power is also set in the glove box to prevent oxidation. The SPS process is performed in vacuum condition during the sintering.

2.2 Mechanical Alloy

There are many types of alloying techniques such as SPEX shaker mills, planetary ball mills, vertical rotating ball mill and attritor mills. In this study, the planetary type of ball mill is used and Fig. 2.3 shows the mechanism of its operation, which generates strong centrifuge forces to create impacts of high energy MA actions inside the container by introducing the opposite rotating directions of grinding jar and supporting disc. The loading of Mg and Si, and unloading of alloyed Mg_2Si powders in the milling jar with balls were carried out in the glove box system at Ar atmosphere to avoid oxidation of the starting materials, and then the milling jar was set in the planetary ball milling equipment at $350rpm$ for $25hr$ at dry condition followed by $250rpm$ for $3hr$ at wet grinding milling with hexane as process control agent (PCA). The oxygen-free n-hexane (C_6H_{12}) has an advantage to protect the material from oxidation. After finishing alloying process, the milled powder was transferred to the glove box and dried in vacuum environment in antechamber of the glove box for up to $6hr$, and then finally nanostructured TE powder was obtained. This alloying process is controlled by various parameters such as grinding medium, alloying atmosphere, control agents, alloying speed, alloying time, and ball composition, which are studied in the following sections.

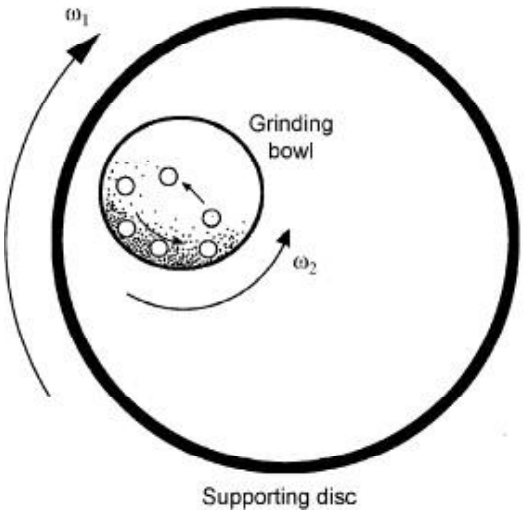

Figure 2.3: The schematic figure of planetary ball mill [61]

2.2.1 Grinding jar selection

In order to investigate the effect of base materials of grinding medium, MA processes with different types of jar and ball were carried out. Various types of jar and balls are available such as alumina, stainless steel, tungsten carbide, agate and zirconium oxide depending on its purpose and alloying elements. In this study of Mg_2Si alloying, three types of alloying medium has been tried for the suitable selection. Fig. 2.4 is XRD peak analysis of alloyed powders by using various types of grinding medium such as alumina, steel and tungsten carbide. Alumina and steel based alloy jar and balls are widely used for grinding and alloying process. However, Al_2O_3 peaks were detected in synthesized powder at $200rpm$ for $24hr$ (Fig. 2.4 (b)), and Fe peak was also observed in alloyed powder at $300rpm$ for $8hr$ (Fig. 2.4 (a)). These contaminations came from the reaction between particles and grinding medium due to the high energy induced by high rotating speed and longer alloying time. Fig. 2.5 is SEM image showing Fe contamination of sintered sample at which bright spot indicates metal contents of Fe coming from the stainless steel jar and balls. The MA using tungsten carbide (WC) jar and balls had no contamination after grinding shown in

Fig. 2.4 (c). Therefore, all MA processes in this study were carried out using WC medium under Ar atmosphere in the glove box.

2.2.2 The effect of wet alloying

Since the MA process with Mg and Si is ductile-brittle combination, the powder particles get more cold-welded each other due to the heavy plastic deformation. The complete alloying occurs usually when a balance is maintained between cold-welding and fracturing of particles [62]. In order to reduce the effect of cold-welding, wet alloying process is required with PCA such as stearic acid, hexane, methanol, and ethanol. The PCA adsorbs on the surface of the powder particles and minimizes cold-welding between powder particles and inhibits agglomeration, and it also lowers the surface tension of the solid material [62]. In this study, hexane was used as PCA because Mg and Si is significantly sensitive to oxygen, thus oxygen-free agent should be selected. Another reason why wet mechanical alloying was performed is due to the quantity of the alloyed powders obtained after MA process. Without wet alloying step, most milled particles after dry milling process stick to grind jar and balls, thus less than 50% of powders was obtained. On the other hand, $80 \sim 90\%$ of the initial power was returned after the wet alloying process. This is also important to obtain the exact composition ratio of alloyed compounds, since powder loss due to sticking to ball and jar causes inaccurate molar ratio of the milled alloy. Therefore, wet mechanical alloying process is required for not only the true alloying result, but also exact chemical composition.

2.2.3 The optimization of alloying conditions

To investigate the effects of MA process some important parameters should be considered:

- Alloying speed
- Alloying time

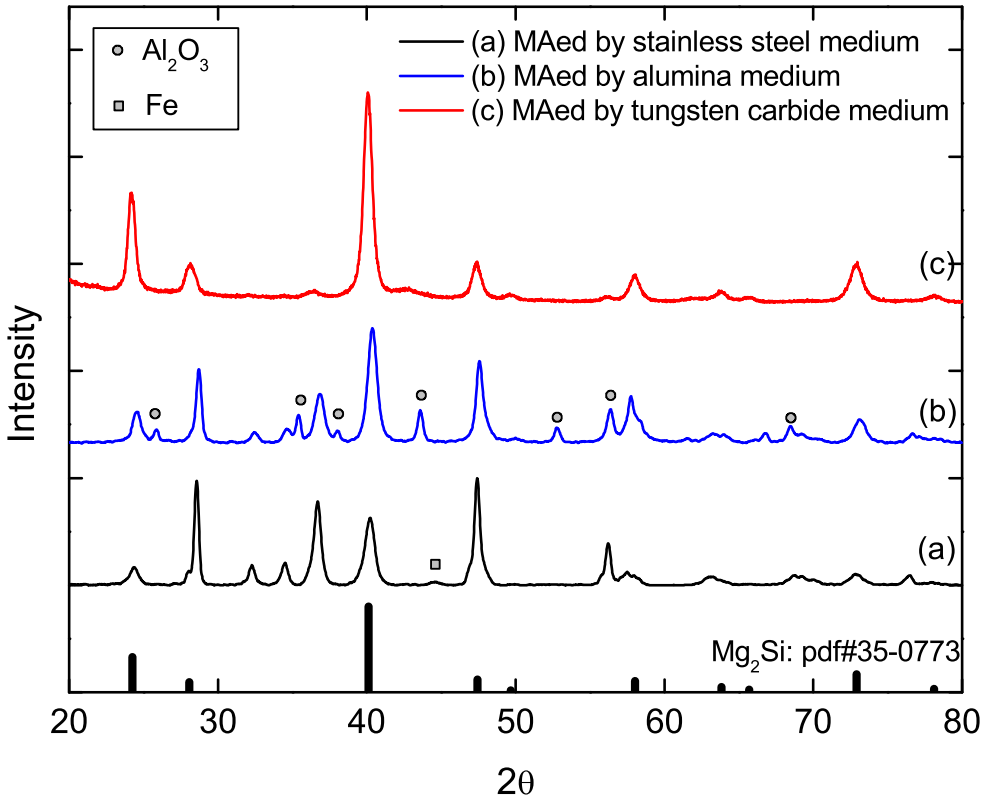

Figure 2.4: The XRD pattern of using various types of milling medium: (a) stainless steel, (b) alumina, and (c) tungsten carbide

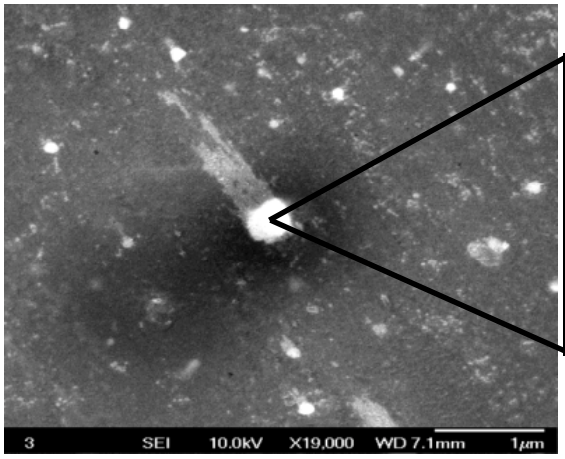

Atom	wt%	at%
Fe	36.44	21.70
Mg	28.99	39.65
Si	24.66	29.21
Ge	6.89	3.16

(a) (b)

Figure 2.5: Fe contamination in MA of stainless steel jar and balls: (a) SEM image of sintered Mg-Si-Ge and (b) EDS data of the surface

- The effect of ball composition

The processing speed (rpm) is one of the important factors for the complete alloying process. If it is low below the threshold speed, the process becomes a result of simple mixture, not alloyed compounds. However, too high speed can cause unwanted contamination from grinding medium materials. As described in the section 2.2.1 WC jar and balls were used, which has much less chance to contaminate TE powder from grinding materials since WC is much harder and stable material compared with others such as steel and alumina. In this study, alloying experiments were carried out at around $350rpm \sim 400rpm$ using WC jar and balls, at which no contamination was detected and fully alloyed Mg_2Si was obtained.

Usually, grinding balls with 10 mm diameter are widely used since smaller diameter below 10 mm are found to have not enough kinetic energy to alloy the bulk material, and too large balls can lead to a significant increase of contamination in the powder [48]. Table 2.2

Index	Starting Mat.	Speed	Time	Ball composition
MA-0	Mg_2Si, Bi	mixture		-
MA-1		$400rpm$	$5hr$	$10mm$ $(50ea)$
MA-2		$400rpm$	$15hr$	$10mm$ $(50ea)$
MA-3		$380rpm$	$15hr$	$6mm(80ea)$, $10mm(50ea)$, $15mm(2ea)$

Table 2.2: MA with various milling time and ball composition

and Fig. 2.6 describe the effect of ball size and its composition. In order to investigate the conditions of MA processing four different alloying processes were carried out. MA-0 is the mixture of Mg_2Si powder and Bi doping element, where the pre-synthesized Mg_2Si powders were offered by Union Material Inc. MA-1 is the alloying result at $400rpm$ for $5hr$ with monotonic ball composition of $10mm$ diameter. MA-2 is processed at the same condition as MA-1 except the milling time of $15hr$. MA-3 is carried out at $380rpm$ for $15hr$ with various size of milling balls such as $6mm$, $10mm$ and $15mm$, shown in Table 2.2. The described speed and time in this table is the dry alloying condition. Wet grindings were done under the same condition at $250rpm$ for $3hr$.

As to alloying time, XRD result of MA-1 to MA-2 in the Fig. 2.6 shows that according to the increase of milling time the XRD peak is getting wide, which is indicating small grains in particles since MA-2 introduced higher grinding energy than MA-1 by increasing milling time. Regarding MA-2 and MA-3, mixed ball composition generated more effective alloying energy so that grain size of milled powder of MA-3 condition was further decreased compared with that of MA-2. Fig. 2.6 (b) shows that the XRD peak of MA-3 become broaden than that of MA-2, which means the milled powder at the condition of mixed ball (MA-3) has finer grain than that at the monolithic ball composition (MA-2) even though MA-3 was carried out at $380rpm$ which is lower speed than MA-2. Therefore, the combination of various size of milling balls is more effective to generate higher milling energy enabling

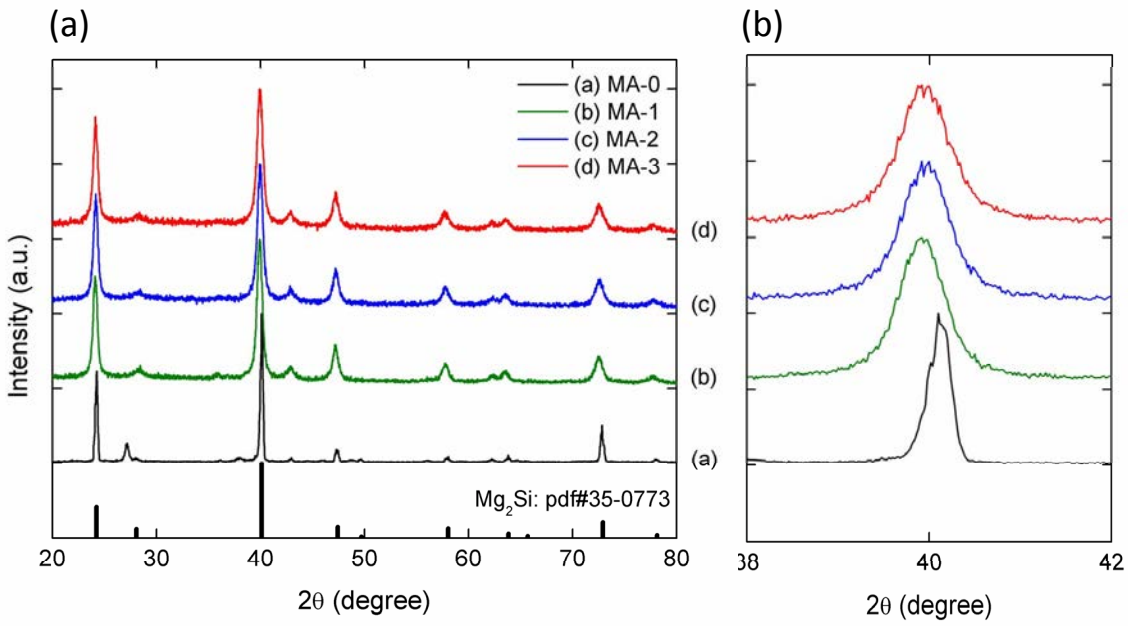

Figure 2.6: XRD result of various alloying conditions: (a) XRD peaks of different alloying conditions(MA-0∼MA-3) and (b) XRD peaks of specific angle to compare grain size of milled particles

particle and grain finer.

As a result, MA-3 has the largest alloying energy among them, which means that various size distribution of balls is effective than monotonic ball condition and longer milling time can generate fine particles and grains. However, it needs to be careful to determine the ball composition and alloying time. Too much milling time causes the agglomeration of powder on the bottom of the corner in the jar, which gives less chance to be completely alloyed.

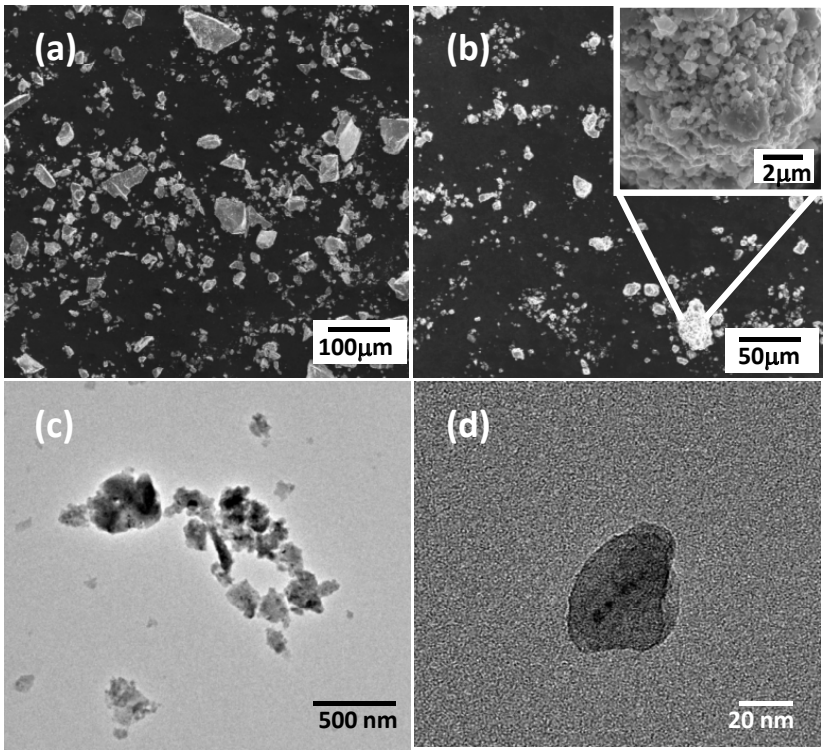

Figure 2.7: Microscope images of MAed powders: (a) MA-0 [SEM] (b) MA-2 [SEM] (c) MA-3 [TEM], and (d) nano sized particle obtained from MA-3 [TEM]

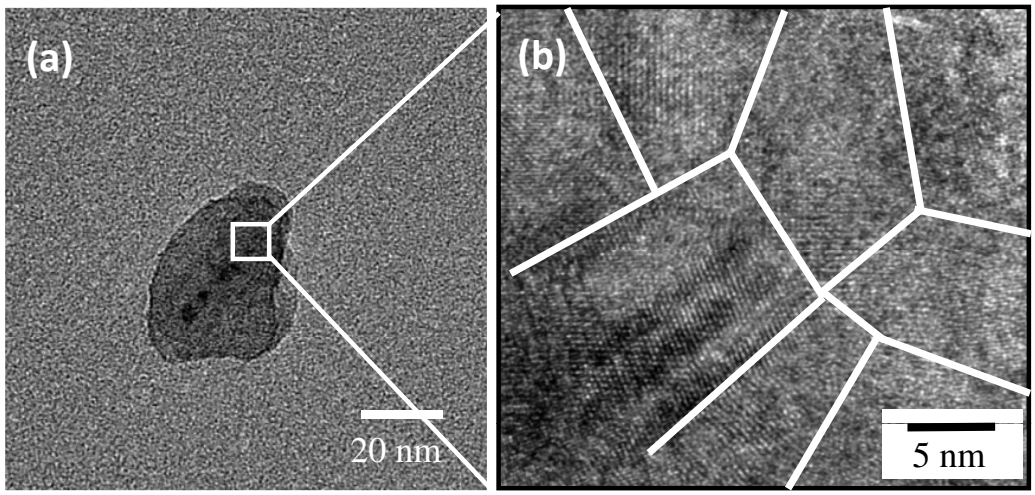

Figure 2.8: HRTEM images of n-type Mg_2Si: (a) a single nano-particle, and (b) grain boundaries with different orientation

2.2.4 Nanostructure of alloyed powder

Fig. 2.7 shows the microscopy images of mechanically alloyed particles of Mg_2Si according to different alloying conditions. Particle size was in the range of sub micron to hundred micron (Fig. 2.7 (a)) before alloying process. Along with the increment of alloying energy the size of as-milled particles became finer less than 20 μm at 400 rpm for 15 hr in MA-2 (2.7 (b)), and alloyed nanoparticles as small as 20 nm can be successfully obtained at $380rpm$ for $15hr$ with the combination of various ball size from $6mm$ to $15mm$ (2.7 (c) and (d)).

High resolution transmission electron microscopy (HRTEM) images in Fig. 2.8 (b) show that the grain boundaries are randomly oriented. These adjacent grains with random orientation enable more phonon scattering effectively, which gives rise to the reduction of κ_{ph}. Nanostructured grain boundaries of alloyed particles were generated by cold-welding process of the mechanical alloying, which produced dislocations, and then during further alloying process a number of dislocations formed fine grain boundaries in particles. Therefore, high energy MA process successfully yielded nano sized alloyed particles with range of 20 nm to 200 nm and sub boundary interfaces in the particles with sub nanometers. Alloyed nano powders of Mg_2Si was transferred to sintering steps to fabricate bulk solid disk specimen where SPS technology is contributed to minimizing grain growth during high temperature processing, which is discussed in the following section.

2.3 Spark Plasma Sintering (SPS)

SPS is a pressure sintering method based on high temperature plasma (spark plasma) generated by electrical discharge ON-OFF DC pulse energizing [63]. The key feature of SPS is a high thermal efficiency due to the direct heating of the graphite mold and stacked powder materials by the large spark pulse current. Fig 2.9 (a) shows the configuration of our SPS system. The process of SPS in the graphite mold can be described with 5 steps such as spark discharge, a local high temperature state, evaporation, melting, and necking.

From a spark discharge at the contact point of particles a local high temperature state is generated and then, evaporation and melting on the surface of powders occur, and necking is formed.

This noble sintering technique enables nano powders to be consolidated with a high densification and keep still nano sized grains due to rapid sintering procedure. The nano powders synthesized by MA process were set into graphite die, and compressed at a single-axis pressurization system in the chamber with vacuum state. During the sintering process carbon die set should be inspected frequently because nanopowder can be melt below its melting point at a certain condition or fracture of graphite die can be occurred by heavy pressure at high temperature.

2.3.1 Parametric study for SPS optimization

The key parameters of SPS process are soak temperature, soak time, applied pressure and heating/cooling rate, which should be optimized for high densification and minimization of grain growth. Among them, SPS temperature and time is most critical factors to produce compact bulk specimen and suppress grain growth. To investigate the effects of these factors, ten different SPS processes shown in Table 2.4 were carried out under the compressive pressure of $50MPa$ and the heating rate of $100\,^{\circ}C/min$ to see the impact of soak temperature and time on the experiments. In this parametric study, MAed SiGe powder alloyed by NASA-JPL was used.

At first, sintering process was designed from $600\,^{\circ}C$ in $5min$ and $10min$, and SPS temperature was increased by $50\,^{\circ}C$ up to $1000\,^{\circ}C$. Heating and cooling were carried out under vacuum condition. After the sintering process, density was measured by Archimedes's method after polishing. The result of density measurement shown in the Table 2.4 indicates that specimens processed at lower temperature than $800\,^{\circ}C$ were not solidified completely since soak temperatures were not enough to reach melting and necking stage in SPS. On the other hand, the difference of the process (8) and (9) are within 2% compared to the

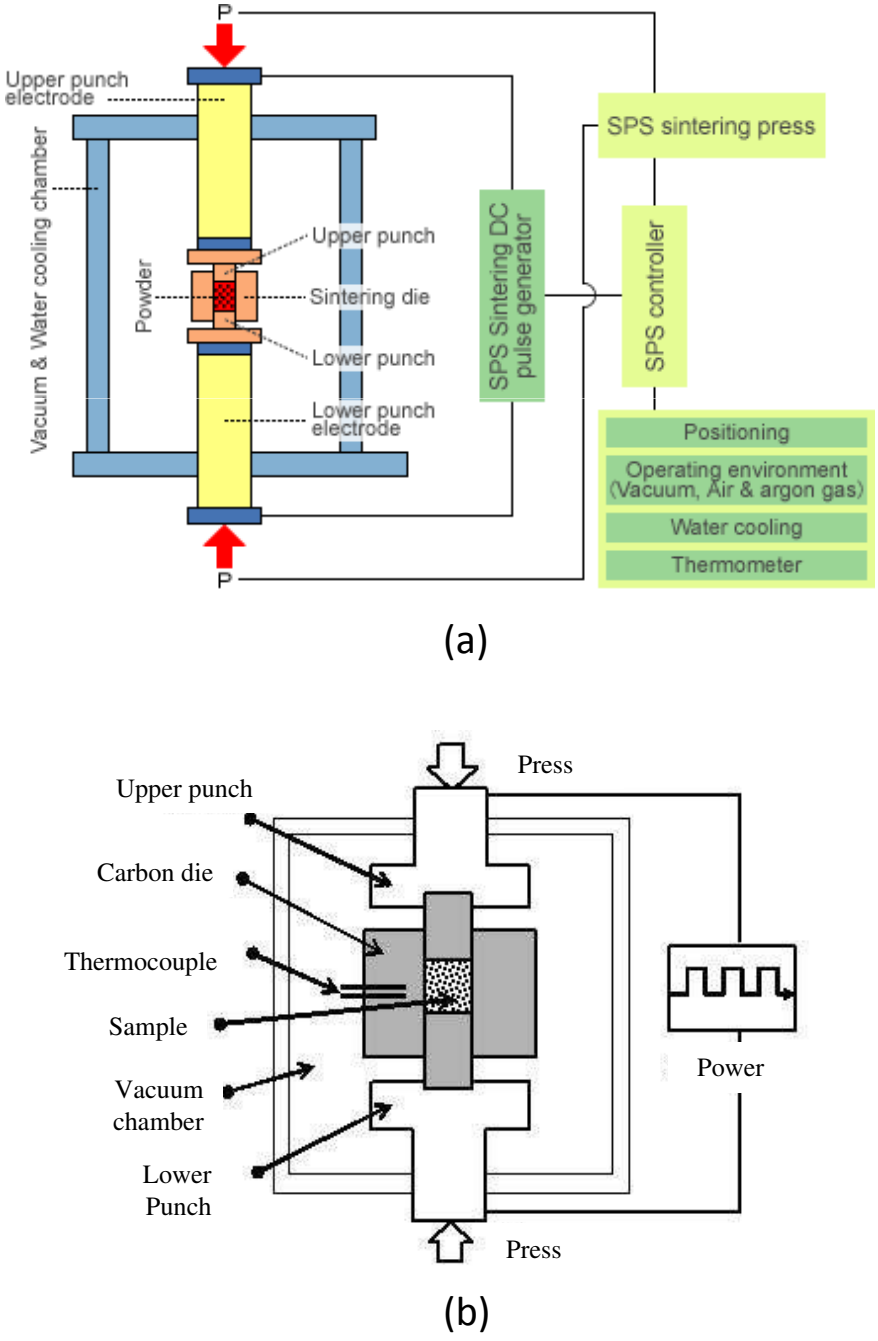

Figure 2.9: SPS system configuration: (a) overall SPS system, and (b) a graphite mold (shown in dark color) in the chamber

Temp. / Time	$600\,^{\circ}C$	$700\,^{\circ}C$	$750\,^{\circ}C$	$800\,^{\circ}C$	$850\,^{\circ}C$	$950\,^{\circ}C$	$1000\,^{\circ}C$
$5min$	(1)	(2)	(4)	(6)	(8)	(9)	(10)
$10min$	-	(3)	(5)	(7)	-	-	-

Table 2.3: Parameter combination of SPS

theoretical density.

Fig. 2.10 shows the effects of soak temperature and time for high densification. Soak temperature is more important parameter to synthesize compact bulk TE materials due to the increase of 5%, 7.4% and 14% of relative density value according to $100\,^{\circ}C$ increment of soak temperature from $600\,^{\circ}C$ to $900\,^{\circ}C$ respectively (Fig. 2.10 (a)) while the increase of soak time, $5min$ to $10min$, gives less than 3% increase of the measured density (Fig. 2.10 (b)). Therefore, we can conclude soak temperature is more sensitive parameter in SPS process to obtain highly compacted bulk material and the first factor to be decided for the complete process.

2.4 The characterization of TE Properties

In this section, TE properties of synthesized n-type Mg_2Si are discussed. The effect of excessive Mg components was also investigated, and a new doping element has been studied.

Regarding the measurements of TE properties, the Seebeck coefficient and electrical conductivity were measured by using a four-point probe measurement system (Ulvac-Rico, ZEM-3). The sample is prepared in the dimension of $2mm \times 2mm \times 10mm$ by cutting the sintered bulk cylinder into a rectangular bar by using diamond saw after the SPS process. The measurements were carried out from room temperature up to $600\,^{\circ}C$ in a partially-filled Helium environment. Thin carbon foils (75 μm thickness) were inserted into the contact

Index	$MPa - °C - min$	Measured density $[g/cm^3]$	Relative density [%]
(1)	50-600-5	2.31	78.8
(2)	50-700-5	2.42	82.8
(3)	50-700-10	2.46	83.8
(4)	50-750-5	2.53	86.2
(5)	50-750-10	2.53	86.3
(6)	50-800-5	2.61	88.9
(7)	50-800-10	2.68	91.5
(8)	50-850-5	2.97	101.3
(9)	50-950-5	2.98	101.6
(10)	50-1000-5	-	-

Table 2.4: Measured density of each SPS condition

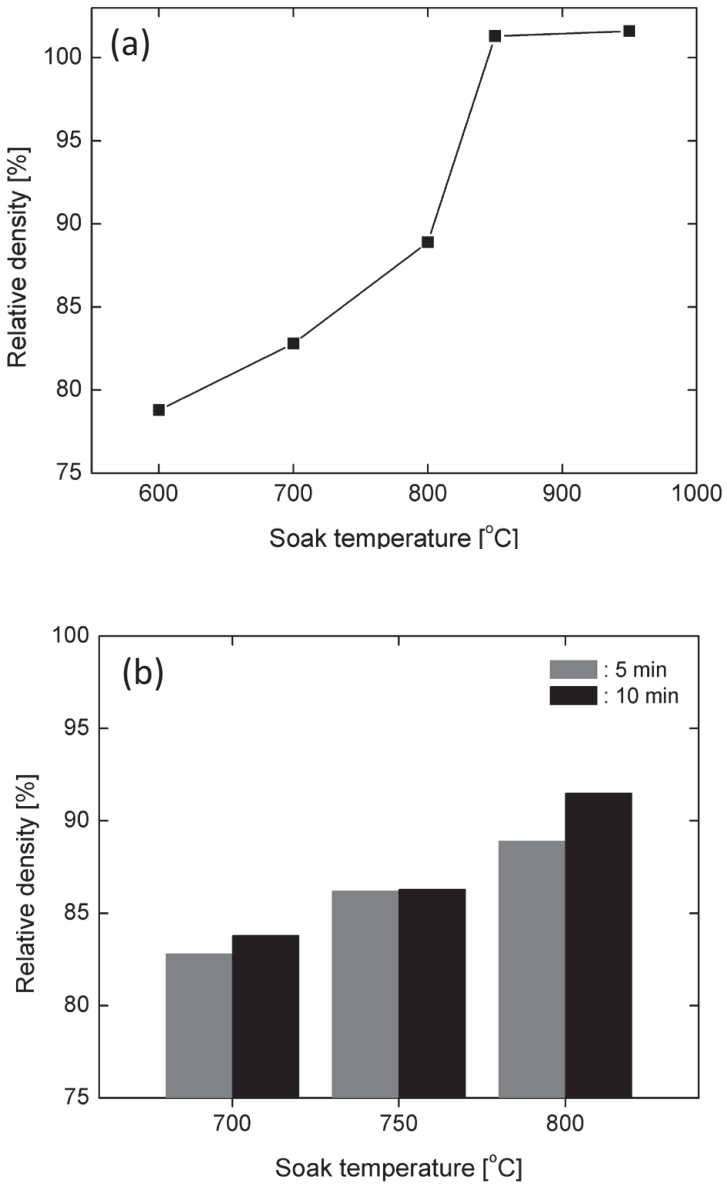

Figure 2.10: SPS effect: (a) relative density by the increment of soak temperature with $5min$ soak time and (b) relative density by the increment of soak time from 5 to $10min$ with the same soak temperature

interfaces of a sample surface and R-type thermocouples to avoid a reaction between Pt and Si during the measurement at high temperature.

For thermal conductivity measurements, a sample 10 mm in diameter and 1 mm thick is then prepared for the laser flash measurement system (Ulvac-Rico, TC-9000). This thin disk specimen was directly obtained by polishing the bulk disk after the SPS. This equipment measures the thermal diffusivity and specific heat capacity of the specimen simultaneously, and the measurements were carried out from room temperature to 600 $^{\circ}C$. The thermal conductivity $[W/(mK)]$ can be calculated from the relationship, $\kappa = \alpha \cdot C_p \cdot d$, where α, and C_p are thermal diffusivity $[m^2/s]$ and specific heat capacity $[J/(kgK)]$ respectively, which are measured by TC-9000, and d is mass density $[kg/m^3]$.

2.4.1 Bi doped Mg_2Si

The typical TE alloys based on solid solution of Mg_2B^{IV} compounds are Mg_2Si - Mg_2Ge, Mg_2Ge - Mg_2Sn, and Mg_2Si - Mg_2Sn. Compared to Si element, Ge and Sn have higher mass density, and Ge is very expensive element, so Mg_2Ge and Mg_2Sn compounds are not suitable for weight-sensitive applications. To meet the requirements of light-weight, non-toxic, and cost-effective TE alloy, doped Mg_2Si TE materials mentioned in Chapter 1.3 was studied.

It has been investigated that bismuth (Bi) is one of the promising doping element in Mg_2Si compound [54, 59]. One reason is that the density of Bi-doped Mg_2Si alloy ($2.2g/cm^3$) is lower than that of the ternary system such as $Mg_2Si_{0.4}Sn_{0.6}$ ($2.9g/cm^3$). Fukano *et.al.* [39] reported the optimized doping of Bi in Mg_2Si system, which was 3 $at\%$. Thus, this study fixed the doping condition as 3 $at\%$ of Bi. Based on 3 $at\%$ Bi doping, the effect of excessive Mg component was discussed.

Since Mg is ductile material, Mg sticks to grinding balls and wall of the jar during MA process. The loss of Mg disables to form the exact composition of Mg_2Si. In order to investigate the effect of excessive Mg to the TE properties, MA with three different cases, 0 $wt\%$, 2 $wt\%$ and 4 $wt\%$ of excessive Mg powder, was carried out by using Mg (99.9%),

Si (99.9%), and Bi (99.999%) powders as the starting materials in the size of 140 μm. MA processing was conducted in Ar atmosphere under $350rpm - 25hr$ of dry condition followed by $250rpm - 3hr$ of wet alloy, where hexane was used as a PCA. Fig. 2.11 (a) is XRD pattern of the early stage of MA after $5hr$ alloying. In this stage, the peak of alloyed Mg_2Si was detected, but most of Mg and Si remained as raw materials. After $25hr$ MA processing, completely alloyed Mg_2Si was obtained and its XRD pattern is shown in Fig. 2.11 (b). This alloyed powders were sintered by SPS under $80MPa - 800\,^{\circ}C - 3min$ in vacuum chamber. The XRD peak of as-sintered bulk Mg_2Si is shown in Fig. 2.11 (c). The electrical conductivity and Seebeck coefficient were measured simultaneously by a commercial equipment (ZEM-3, Ulvac-Rico), and thermal conductivity was obtained by measuring thermal diffusivity and specific heat capacity at the same time by a laser flash system (TC-9000, Ulvac-Rico) from room temperature up to $600\,^{\circ}C$.

Fig 2.12 shows the TE properties of electrical conductivity (a), Seebeck coefficient (b), thermal conductivity (c) and the figure-of-merit (d), in which 2% surplus of Mg gave the highest value of ZT, 0.44, but the variation of TE properties according to the amount of excessive Mg was within 3%. Based on the results, it is verified that two-step MA procedure with the combination of dry MA and wet MA gave rise to the exact molar ratio of Mg_2Si without losing Mg during MA process.

2.4.2 Bi-In doped Mg_2Si

In order to improve ZT, new doping element was investigated. Various n-type dopants in Mg_2Si system have been reported such as Al [60], La [58] and Sb [64]. However, Bi is still the most promising doping element among them for n-type [39]. A secondary doping material was considered to focus on the improvement of the electrical properties, while the thermal conductivity can be reduced by generating nano grain structures. The electrical properties of Mg_2Si with new dopants such as Co, Fe, Ni and In are shown in Fig. 2.13. Fe doped and In doped Mg_2Si show better electrical conductivity in Fig. 2.13 (a) at higher

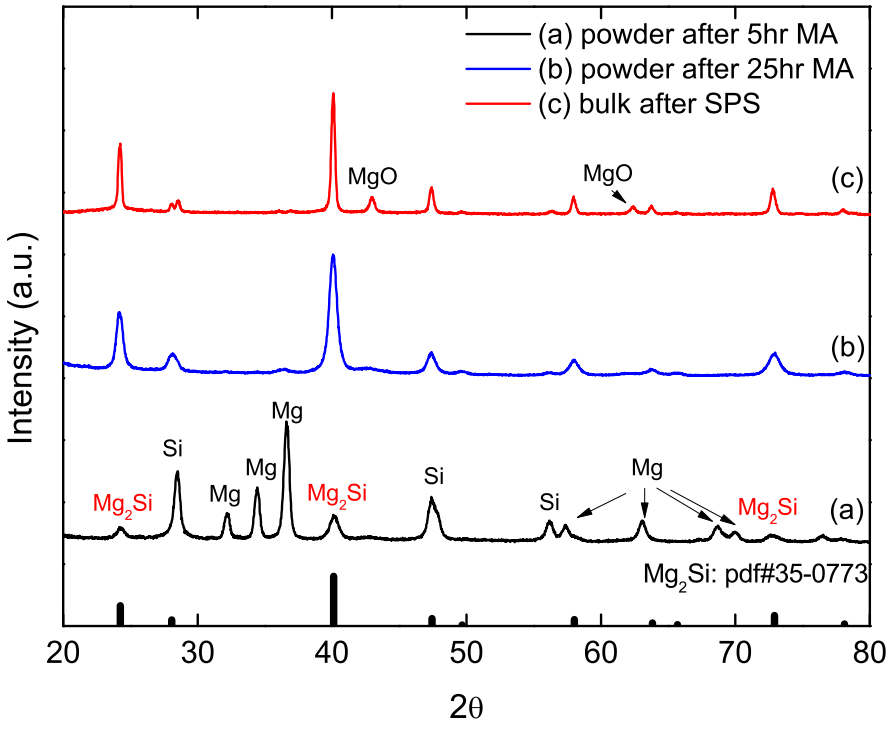

Figure 2.11: XRD peaks of alloyed powder and sintered bulk sample

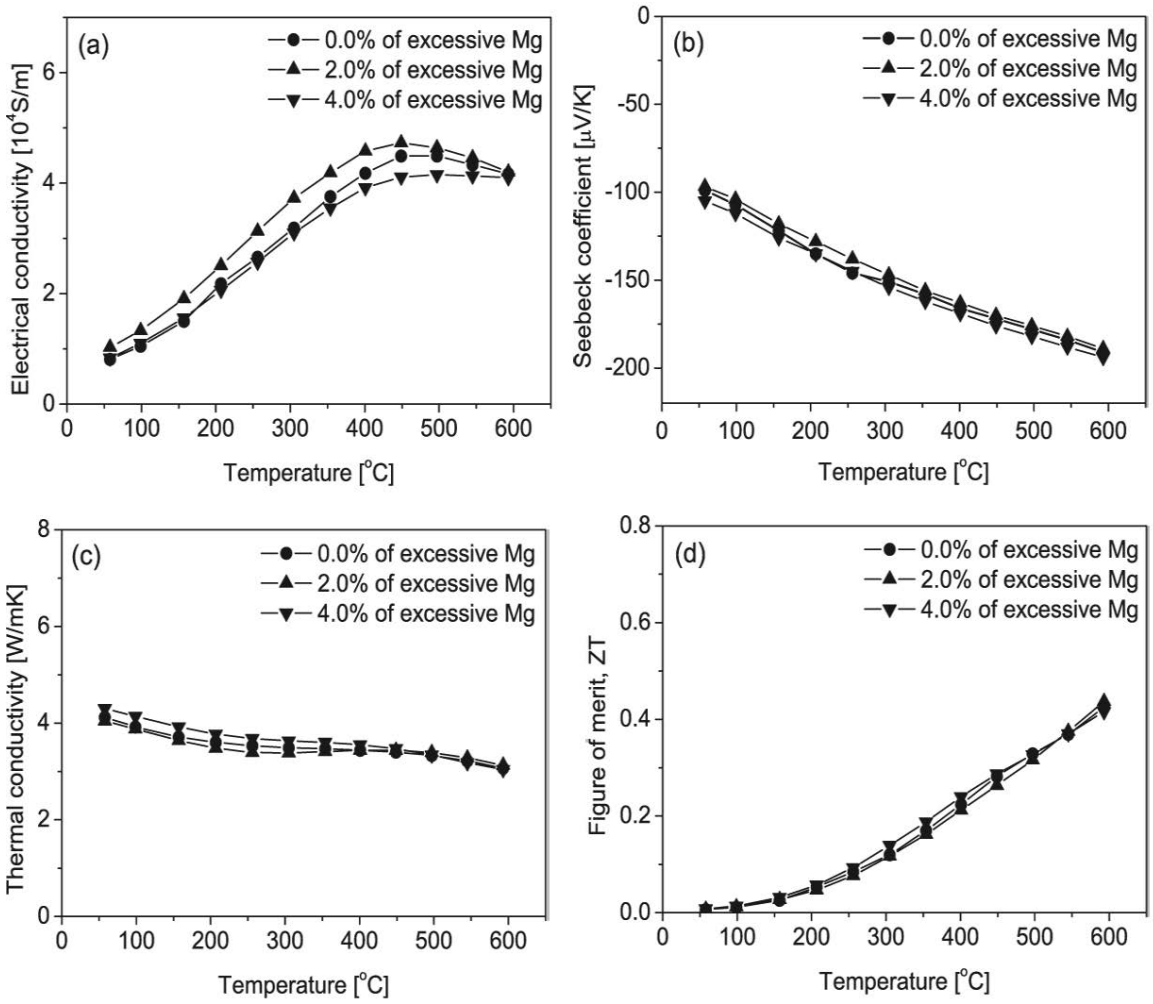

Figure 2.12: TE properties of 3 *at*% Bi doped Mg_2Si with excessive Mg powder: (a) electrical conductivity, (b) Seebeck coefficient, (c) thermal conductivity and (d) the figure-of-merit

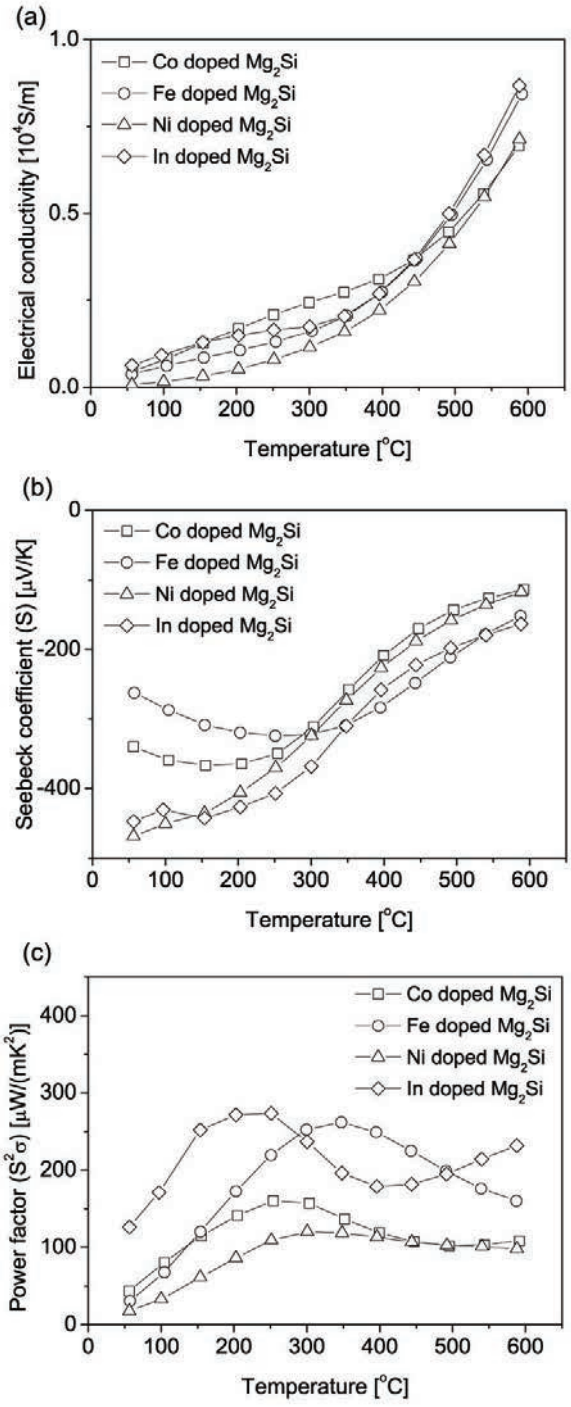

Figure 2.13: The investigation of new doping element to improve electrical properties: (a) electrical conductivity and (b) Seebeck coefficient

temperature range among others, and In doped Mg_2Si has larger value of Seebeck coefficient allover the measured temperature range in Fig. 2.13 (b). Power factor ($S^2\sigma$) was plotted in Fig. 2.13 (c) in which In and Fe are good candidates showing higher peaks compared to others. However, Fe is heavier material (higher mass density) and easier to be oxides than In, so In was selected as an additional dopant to Bi doped Mg_2Si. Both Bi and In doped Mg_2Si was synthesized with the same method of MA and SPS process while the alloying energy was increased by introducing higher speed and longer duration time on the wet grinding process, which is $325rpm$ for $5hr$. The measured TE properties of 3 $at\%$ Bi and 1 $at\%$ In doped Mg_2Si are shown in Fig. 2.14 compared with 3 $at\%$ Bi doped Mg_2Si.

Fig. 2.14 (a) and (b) shows electrical conductivity and Seebeck coefficient of the Bi doped and Bi-In doped Mg_2Si alloys. While Seebeck coefficient (2.14 (b)) is almost identical each other through the measured temperature range, electrical conductivity (2.14 (a)) of the bulk Bi-In doped Mg_2Si is increased by factor of 2 from room temperature to around $350\,^{\circ}C$ compared with Bi doped Mg_2Si, and the difference is getting smaller from $350\,^{\circ}C$ to $600\,^{\circ}C$. The enhancement of the electrical conductivity is due to the increase of carrier concentration by doping with In. The peaks of electrical conductivity appear on both alloys, which means that the conduction mechanism transforms from semiconductor-like to metal-like one with the increase of temperature, where electric conductivity is increasing at lower temperature because thermal excitation is predominant.

Fig. 2.14 (c) shows the temperature dependence of thermal conductivity, as compared with that of Bi doped Mg_2Si. It was decreased with increasing temperature through the whole measured range since phonon scattering at higher temperature is primary source of thermal resistance. In order to understand the contribution of thermal conductivity by lattice and electron components, the thermal conductivity by electron (κ_{el}) is calculated by using Wiedemann-Frnaz law, $\kappa_{el} = L_0\sigma T$, where L_0, σ and T are Lorentz number, electrical conductivity and absolute temperature, respectively. 2.45×10^{-8} $[V^2/K^2]$ was used as Lorentz number in this alloy assuming the degenerate semiconductor [54, 60, 65] even though Lorentz number for most thermoelectric materials is lower than that. κ_{ph} is

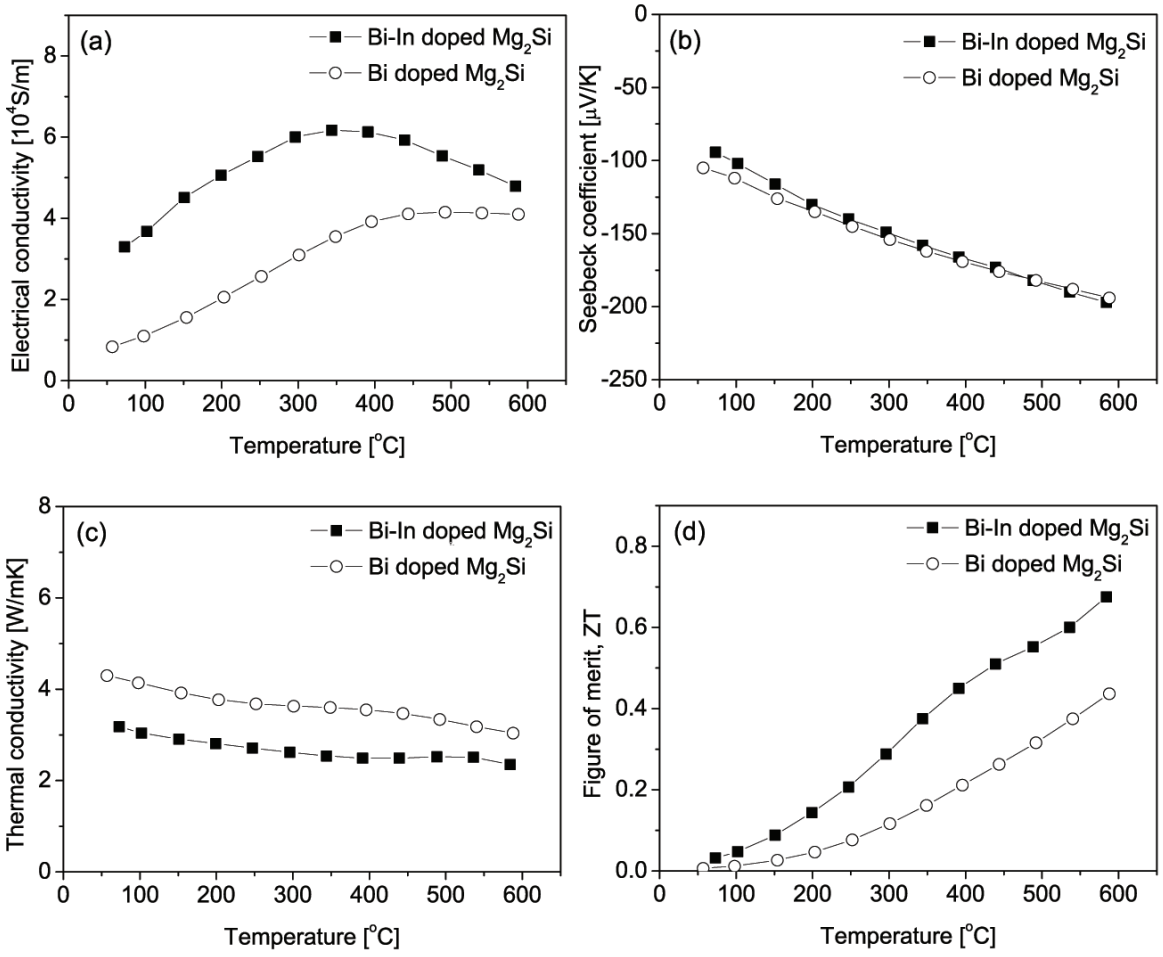

Figure 2.14: TE properties of Bi doped Mg_2Si and Bi-In doped Mg_2Si: (a) electrical conductivity (b) Seebeck coefficient (c) thermal conductivity, and (d) the figure-of-merit

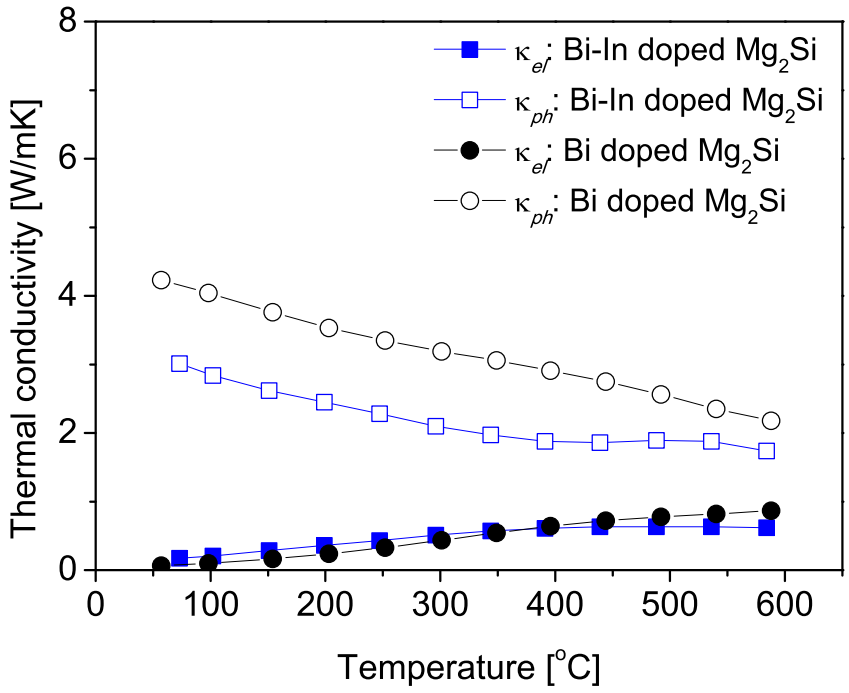

Figure 2.15: Thermal conductivity contribution of lattice and electron components

calculated by subtracting κ_{el} from κ. Fig. 2.15 shows κ_{el} increases with higher temperature at which thermal excitation gives energy for electrons to move from valence band to conduction band, but κ_{ph} has reduction with an increase of temperature due to higher chance of scattering at higher temperature. Fig. 2.15 indicates the thermal conductivity is mainly influenced by lattice component, κ_{ph}, and the total thermal conductivity of Bi-In doped Mg_2Si was reduced compared with Bi doped Mg_2Si due to its finer grains. Therefore, ZT of Bi and In doped Mg_2Si was enhanced from 0.44 to 0.68, which is 1.5 times larger.

2.5 The characterization of nanostructure in bulk TE materials

Nanostructures in bulk alloy were observed using Transmission Electron Microscope (TEM) work. TEM specimens were prepared using two different methods: (a) Twin-jetting

and (b) Focused ion beam (FIB).

2.5.1 Twin-jetting method

Electrolytic thinning is an effective method for conductive materials without any induced artifacts. Commercial twin-jetting equipment (TenuPol-5, Struers) simultaneously polishes both sides of the sample, and creates electron transparent specimens within a few minutes. This equipment controls easily adjustable electrolyte flow, polishing voltage, polishing time, and termination detection sensitivity. The typical procedure of twin-jetting method is,

1. Prepare the solution for electro-polishing

2. Cool down the solution up to $-20\,^{\circ}C$ which is the limit of the equipment and reduce the solution temperature further up to $-30\,^{\circ}C$ by using liquid nitrogen.

3. Set the conditions for the thinning process such as,

    - Flow rate of the electrolyte
    - Light stop value
    - Polishing time

4. Check I-V scanning and determine the voltage on the polishing range (see Fig. 2.16)

5. Find optimum conditions of temperature of electrolyte, flow rate, voltage, and polishing time.

6. Cleaning specimens with ethanol and DI water

Fig 2.16 shows the excursion of voltage condition which should be set within polishing region for thinning and creating electron-transparent area on the specimen. Table 2.5 shows various conditions for twin-jetting process with different electrolytes where solution A and

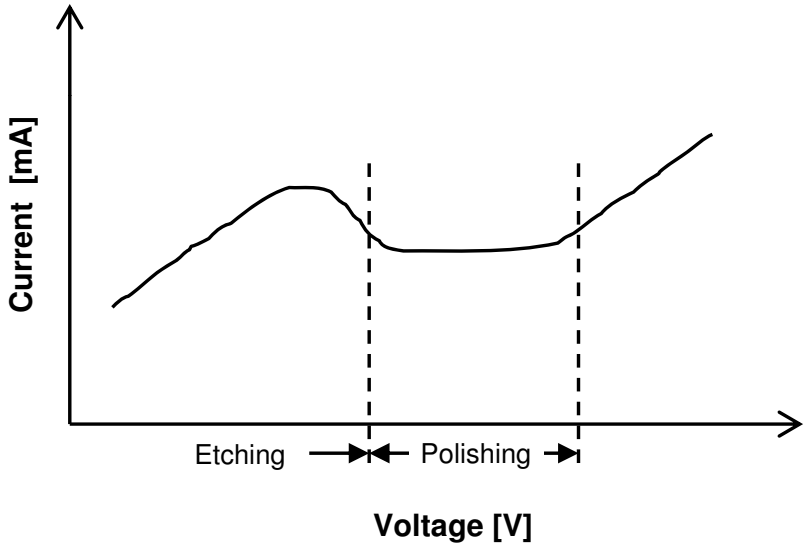

Figure 2.16: I-V scanning curve to determine the optimum voltage for polishing

Specimen $No.$	Temperature $[^{\circ}C]$	Voltage $[V]$	Current $[mA]$	Time [sec]	Flow rate	Electrolyte	Result
1	-37	30	26–64	263	28	A	No etching
2	-37	20	20	180	28	A	No etching
3	-30	20	20–26	143	28	B	Etched out
4	-38.7	18	20	-	28	B	No etching
4-1	-36	32	-	-	28	B	Etched out
5	-35	25	46	-	28	B	No etching

Table 2.5: Experiments for optimizing twin-jetting conditions

B are HNO_3 (20%) + Methanol (80%) and H_2PO_4 + Methanol, respectively. During the processing of sample #1 and #2 which were not etched out, temperature increased by more than $10\,^{\circ}C$ rapidly. This is not normal at twin-jetting process, so electrolyte was changed to type B. In the sample #3, thinning process was performed at $-30\,^{\circ}C$ of electrolyte temperature, 20 [V] applied, and 28 flow units on a full scale of 50. This specimen was etched out in 2 min, so temperature and voltage were reduced up to $-38.7\,^{\circ}C$ and 18 [V], respectively. In this case of sample #4, no etching process occurred. Another polishing was run with the same sample of #4 with increased voltage, but the specimen was etched out completely. Other electrolyte was found such as a solution containing $5g$ lithium chloride, $11g$ magnesium chlorate, 500ml methanol and 100 ml 2-butoxyethanol [66]. However, magnesium chlorate is difficult to be handled in a lab without specific hood and storage. Therefore, other method for the TEM specimen preparation was considered instead of twin-jetting polishing method.

2.5.2 Focused Ion Beam (FIB) method

Most common method for thinning of the disk is twin-jetting process, but this may not be the best method to some alloys. In the case of Mg-Si alloy, it was not successful to produce TEM specimen by using twin-jetting method. The alternative is to make thin area by etching on the edge of half circle by focused ion beam (FIB). The FIB system is similar to a scanning electron microscope (SEM) system, but the FIB uses a gallium (Ga) liquid metal ion source. The Ga ion beam is focused down the probe and scanned across the sample. TEM specimen preparation via FIB process consists of cutting in half-circle disk, polishing up to 100 μm thickness, FIB etching, and ion milling to clean the area damaged by ion beam. The steps for the preparation of TEM specimen are,

1. Cutting : A half-circle disk is required for FIB etching since the flat area of the semicircle is the target region for thinning process by ion beam. A polished rod in 3 mm diameter is sliced into a disk of 1 mm thickness followed by cutting again into

half-disks.

2. Polishing : Finalized thickness of these half disks is 100 ∼120 μm.

3. FIB etching : FIB equipment (FB-2100, Hitachi) was used to create thinned target at the center in the flat area of half-circle processed by several steps of etching since one strong beam for etching at one time can cause damage or break a specimen. In addition, strong ion beam can widen and deepen damaged surface, which is shown as normally amorphous. Fig. 2.17 is schematic figures and explains the thinning process by FIB method. The half disk (2.17 (a)) is placed on the sample holder while the flat surface is face up and is inserted in vacuum chamber. The dimension of target area is 50 μm (height), 2 μm (width) and 10 μm (depth) shown in Fig. 2.17 (c). Fig. 2.17 (d) shows cross section view of the center, at which dimension of the tip of thinned area is 500 nm.

4. Ion milling : In order to remove the contaminated by gun source and damaged area, ion milling process is usually performed after FIB run. This cleaning process of ion milling can remove amorphous layer cause by strong focused ion beam and gallium particles deposited from the target source of FIB gun in the equipment. Milling conditions are,

    a. 1kV - 3mA on both sources (upper and lower)

    b. Chamber pressure : 2.0e-5 Torr

    c. Milling angle : 10 degree

    d. Sample stage motion : continuous rotating (360 degree)

    e. Milling time : 5∼10 min

After the preparation of TEM specimen by cutting, polishing, FIB etching, and ion milling, it is ready to observe the samples. Low magnification and its diffraction pattern

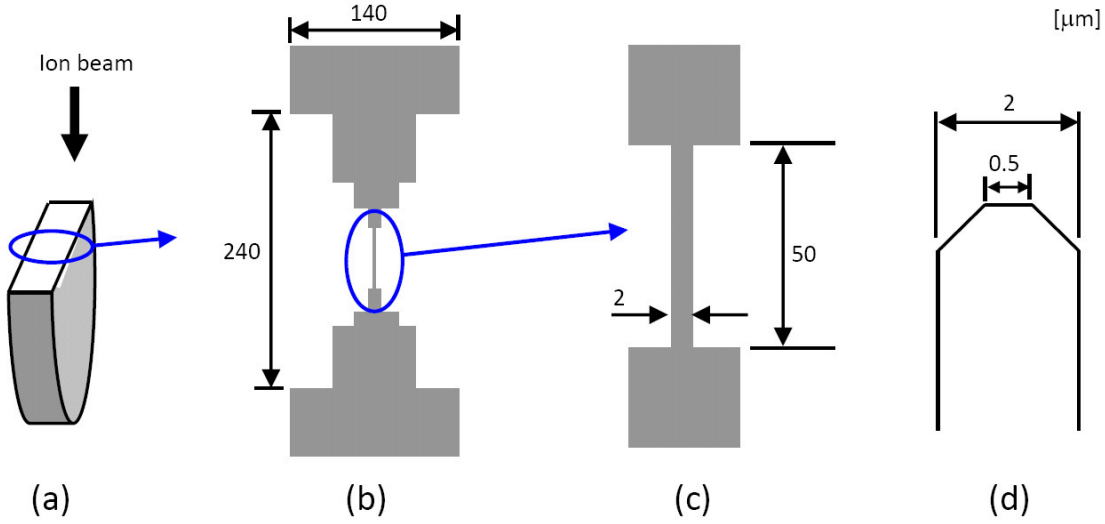

Figure 2.17: Schematic figures of FIB processing: (a) half-circle disk after polishing, (b) top view of the semidisk after FIB processing, (c) top view of the thinnest part at center which is target area of TEM work, and (d) cross section view of target area at center.

were observed by JEM-2011, and JEM-2100F was used for high resolution image, STEM images, and IFFT (Inverse Fast Fourier Transform) analysis.

2.5.3 Nanostructures in bulk Mg_2Si

Two TEM samples shown Table 2.6 were prepared. The sample #2 is bulk Bi-In doped Mg_2Si described in the previous section, and the sample #1 is Mg_2Si alloy doped with Bi, where Mg_2Si powder was offered by Union Material Inc., which was synthesized by direct melting process in an electric furnace followed by crushing the ingot into powders. Then, the powder was consolidated via SPS process.

The microstructures in the sample #1 are shown in Fig. 2.18, where two beam bright field TEM images show grains and their boundaries with grain size of more than 2 μm. This large grain is shown in Fig. 2.18 (a) and its selected area diffraction (SAD) pattern is in the inlet figure, Fig. 2.18 (c). One of the smallest grains is about 1 μm shown in

TEM sample No.	Alloys	Processing route
1	Bi doped Mg_2Si	Direct melting + crushing + SPS
2	Bi-In doped Mg_2Si	MA + SPS

Table 2.6: TEM specimen processed by two different methods

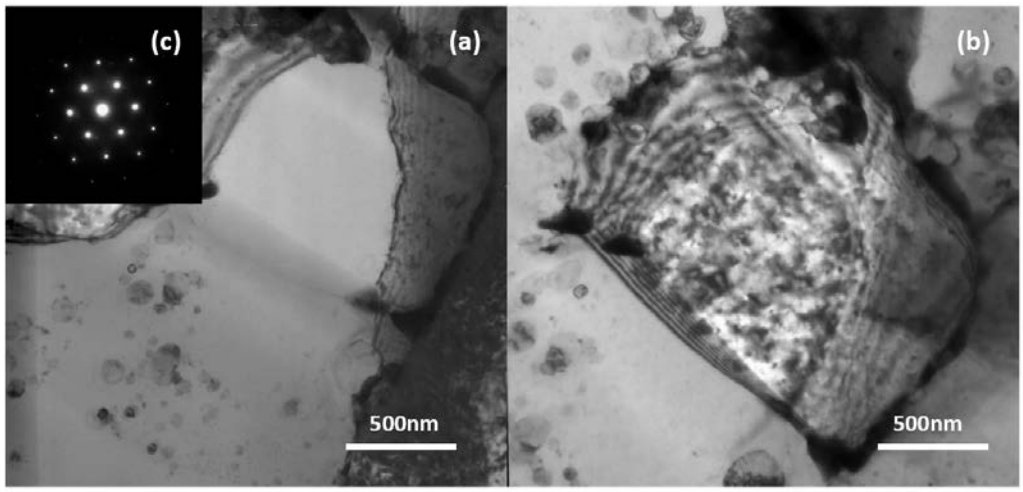

Figure 2.18: TEM images: (a) and (b) are two beam bright field TEM images, and (c) SAD pattern

Fig. 2.18 (b). Along with grain boundaries of both figures (a) and (b), dislocations and spherical precipitates are observed. Energy dispersive x-ray spectroscopy (EDS) analysis was carried out to identify these inclusions. Fig. 2.19 shows STEM image of the interface area of grain boundary, and the spectrum data of EDS analysis, where the size of inclusions is within 200nm. Fig. 2.19 (b) is EDS result of whole area of the image (Fig. 2.19 (a)), and Fig. 2.19 (c) shows EDS result of the inclusion indicated with an arrow, which is identified as magnesium oxide (MgO).

Fig. 2.20 (a) and (c) show TEM and STEM images of the sample #2. The size of most grains is in the range from 100 nm to 500 nm. The ring pattern of SAD in the inlet figure

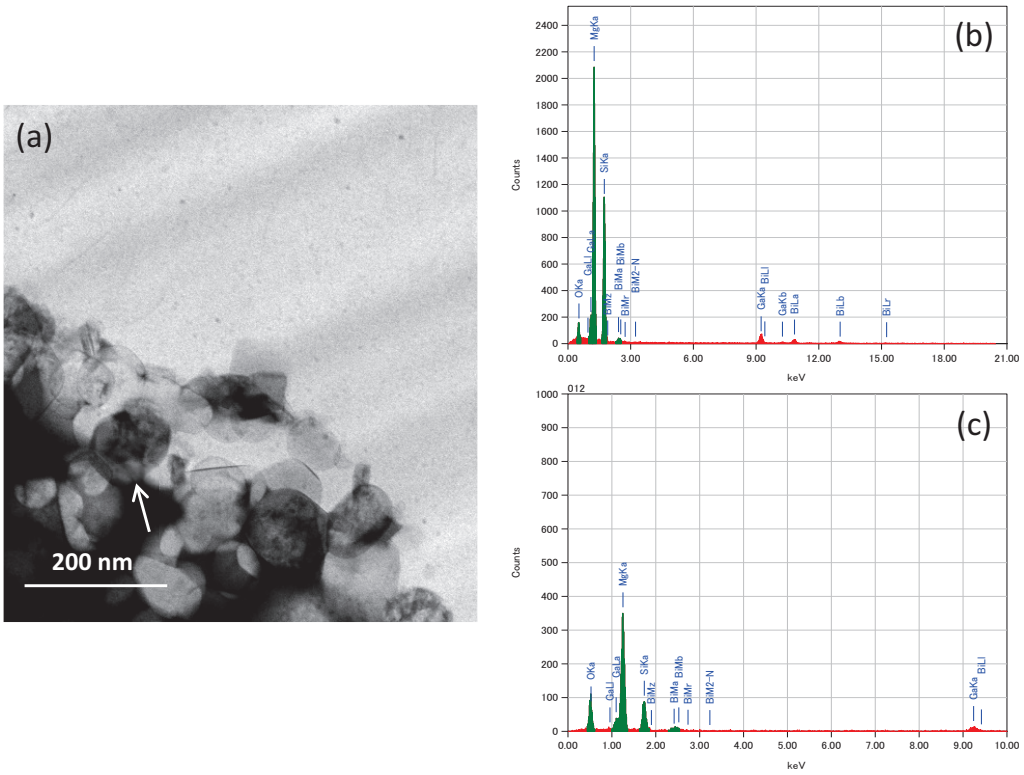

Figure 2.19: EDS analysis near grain boundary: (a) STEM images, (b) EDS analysis of whole area of the image, and (c) EDS data of black inclusions at lower left

(Fig. 2.20 (b)) tells smaller grains in this sample compared with the SAD pattern of single orientation in the sample #1 (Fig. 2.18 (b)). Fig. 2.21 (a) is a high resolution TEM image (HRTEM) near grain boundary and Fig. 2.21 (b) is IFFT (Inverse Fast Fourier Transform) analysis of the image, which shows that some precipitates exists and they form subgrains in a grain. These precipitates produce a large number of grain boundaries which enable more phonon scattering to result in the reduction of thermal conductivity of lattice component. Fig. 2.22 is EDS result of line scanning at the boundary interface including MgO which is shown in black inclusion in the STEM image. Through the scanned line, gallium (Ga) from the beam source of FIB process is detected, which means the cleaning process such as ion milling is further required. Based on TEM observation, it is proved that the combination of MA followed by SPS processing can generate nano size powders.

In summary, high energy MA and SPS for rapid sintering technique were utilized to synthesize Mg_2Si alloy and parametric study for MA and SPS process were carried out. The secondary doping element was investigated and ZT value of Bi-In doped Mg_2Si was improved by 50% compared to Bi doped one. However, it is necessary to optimize the amount of each doping element for the future work. Fig. 2.23 shows κ_{ph} of various bulk Mg_2Si alloys. In this figure, (a) and (b) are the κ_{ph} of nondoped Mg_2Si by MA and SPS route [59], and Bi doped Mg_2Si grown by vertical Bridgman method [54], respectively. Fig. 2.23 (c) and (d) are Bi doped Mg_2Si by SPS after crushing an ingot synthesized by direct melting method (TEM sample #1), and Bi-In doped Mg_2Si via MA followed by SPS (TEM sample #2), respectively. The κ_{ph} of Bi-In doped bulk Mg_2Si was reduced at least by the factor of 2 at $600\,^{\circ}C$ compared with non-doped Mg_2Si (a), and it is also lowered by 60% and 30% compared with (b) and (c), respectively.

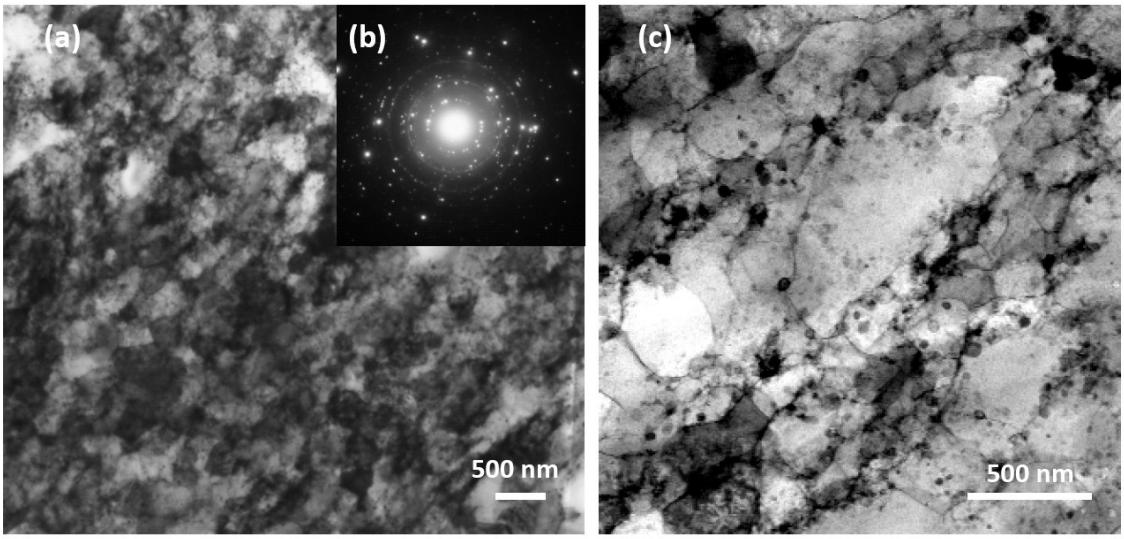

Figure 2.20: TEM images: (a) two beam bright field TEM image, (b) SAD pattern and (c) STEM image

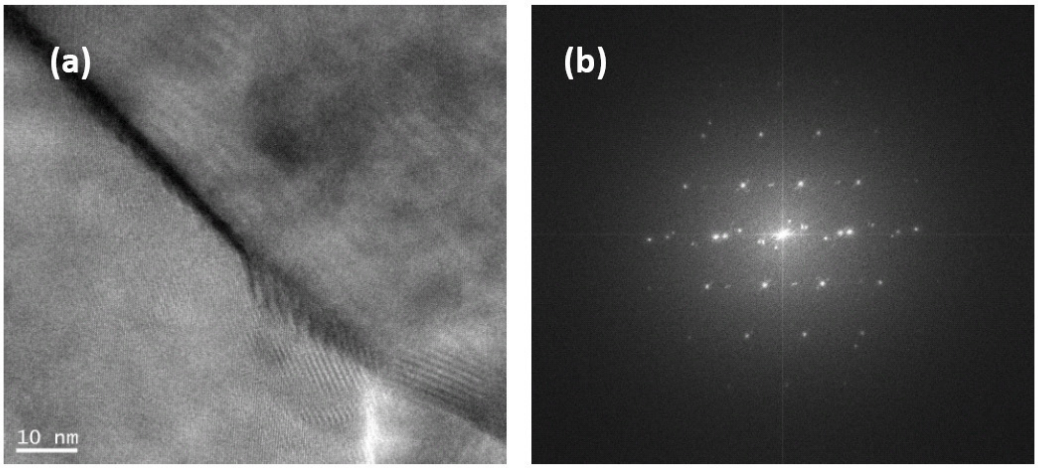

Figure 2.21: HRTEM images: (a) HRTEM image near grain boundary and (b) FFT analysis

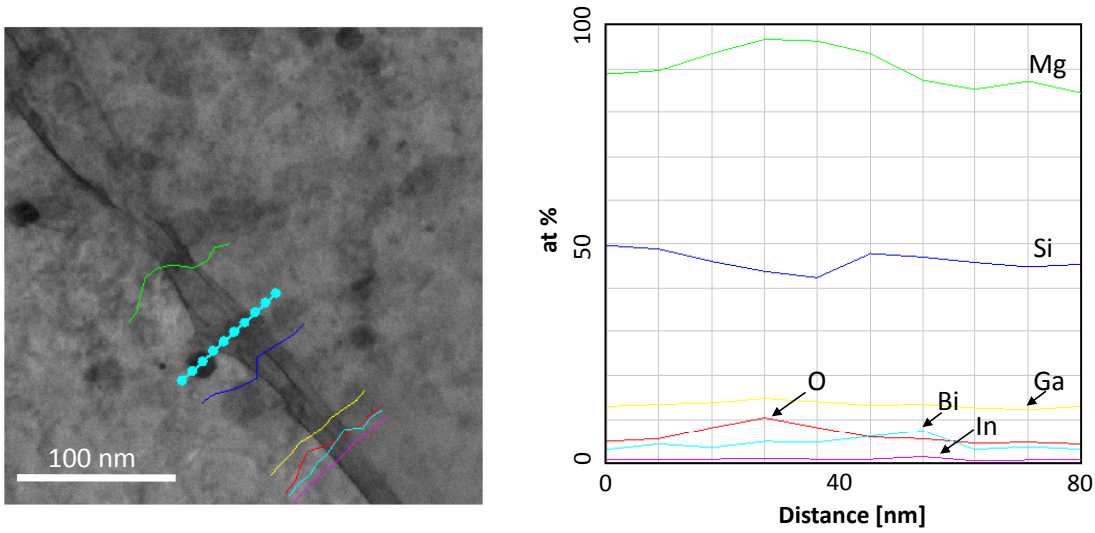

Figure 2.22: The EDS result of line scanning across the grain boundary

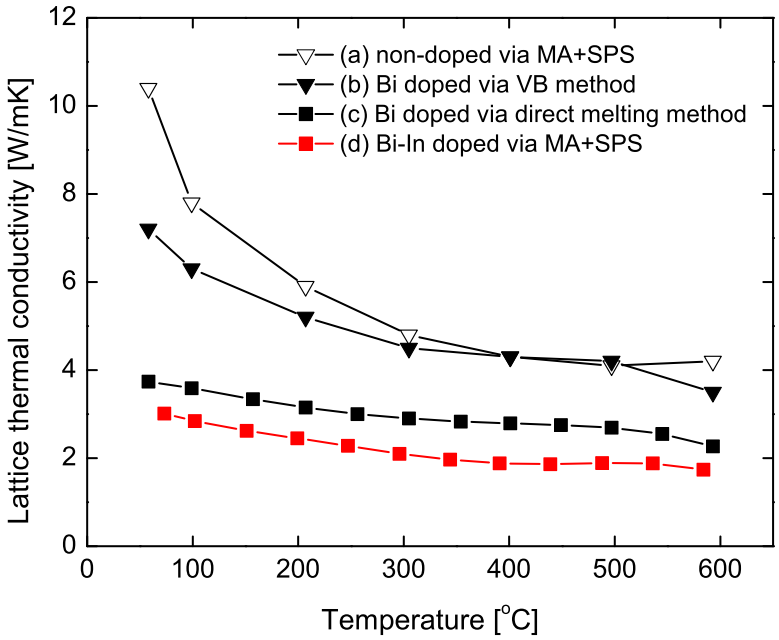

Figure 2.23: The comparison of κ_{ph} with different synthesizing method: (a) non-doped Mg_2Si [59], (b) Bi doped Mg_2Si processed by direct melting and vertical Bridgman [54], (c) Bi doped Mg_2Si by SPS after crushing an ingot synthesized by direct melting method, and (d) Bi-In doped Mg_2Si via MA and SPS

Chapter 3

π DESIGN OF TEG

TE module is effective in the direct conversion from thermal energy to electrical energy. Since TE energy conversion is quiet and non-toxic feedstocks, TE devices have been used in the applications of an electric power generator and a cooling device [67, 68, 69]. Recently, TE modules have been applied to automobiles [70, 71] and unmanned aerial vehicles (UAV) for the purpose of thermal energy harvesting [72, 73]. In automobile applications, the use of TE modules increases fuel efficiency by recapturing wasted exhaust heat and converting it to useable electricity [74].

A segmented design of joined TE materials with different operating temperatures is widely utilized for maximizing output power [46]. Popular segmented TE generators working at a high temperature range use heavy alloys based on Lead Telluride (PbTe) [75], $AgPb_mSbTe_{2+m}$ (LAST) [76], Te/Ag/Ge/Sb (TAGS) [75] and Co_2Sb_3 [77]. Even though these popular TE materials provide higher ZT values, they have large densities of more than 8.0 $[g/cm^3]$. In addition, both Lead (Pb) and Tellurium (Te) are classified as toxic materials [33]. Oxide-based TE alloys, such as Co-O-based p-type and Zn-O-based n-type, are considered but they have low electrical properties resulting in a generator with low output power [78]. Many thermoelectric generators use expensive materials such as the rare element Te, one of the key components in TE system, and Ag in the LAST and Ge in the TAGS systems, resulting in an increased cost of a final device.

This study focuses on bulk Mg_2Si of n-type [54, 79] and HMS of p-type [37] integrated into the high temperature region of a segmented TE generator. Both of these materials have low densities compared with other TE material candidates and have operating temperatures up to $500\,^{\circ}C$. This results in a lighter TEG that has a higher specific output power, which is ideal for airborne engine applications. The synthesis of TE legs and the fabrication of

TE module based on a typical π-shape design will be described. In the following, we will discuss the experimental work on the processing of TE materials, the characterization of TE properties and the measurements of as-assembled TE generator, followed by the comparison of the power output between the experiment and modeling.

3.1 Preparation of TE legs

3.1.1 Synthesis of TE materials

Various processing routes of Mg_2Si have been reported such as direct melting [80], solid state reactions and hot press (HP) [81], the vertical Bridgman method [82, 83], HP after melt-spinning [84], and microwave synthesis [85, 86, 87]. In this chapter, Mg_2Si legs are prepared as follows. Mg (99.95%), Si (99.9999%) and Bi (99.999%) were prepared as starting materials for the Bi doped Mg_2Si high temperature n-type segment. Polycrystalline Mg_2Si with Bi doping was synthesized with Mg:Si ratio of 67:33 (at%) including the Bi dopant (3 at%) by an electric furnace [54]. The obtained polycrystalline compound was crushed into powders via planetary ball milling with a tungsten carbide (WC) jar and balls. The powders were transferred to a glovebox with Ar atmosphere and set up in a graphite die for SPS (Sumitomo Coal Mining Co., Ltd., Dr. Sinter 1020S). The assembled graphite mold of 15 mm in diameter was heated in a two-step procedure for SPS. The first step heats the specimen at 30 MPa from room temperature up to 500 $^\circ C$ with a rate of 100 $^\circ C/min$ and holds the specimen at 500 $^\circ C$ for 3 min. This pre-heating step allows one to maintain low vacuum level at the next sintering step.

As shown in Fig. 3.1, the vacuum level in the SPS chamber starts at 4.4 Pa, increases up to 7 Pa at 500 $^\circ C$, drops to 4.6 Pa after the 3 min holding step at 500 $^\circ C$, and is held at 4.6 Pa for the rest of the process. For the second step, the powder in the graphite mold is pressurized up to 50 MPa while it is heated to 750 $^\circ C$ with a heating rate of 100 $^\circ C$/min. After keeping at 750 $^\circ C$ for 3 min, the specimen is cooled. This optimized two-step SPS process enables one to keep the chamber vacuum level low, which minimizes the chance

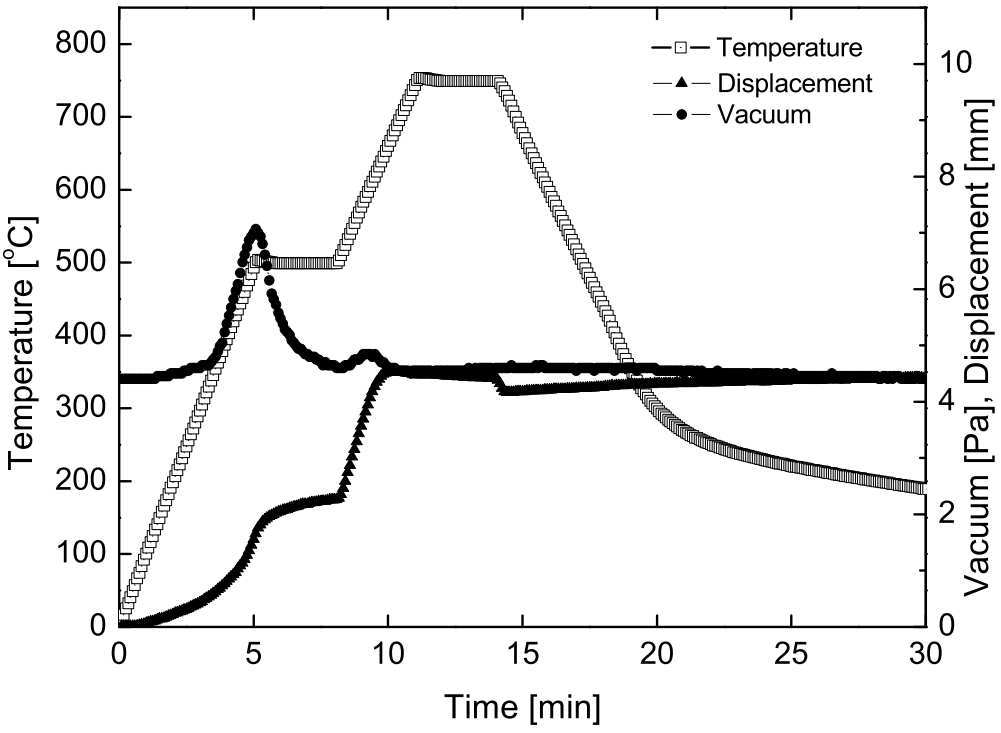

Figure 3.1: Vacuum level and the displacement of the sample during the sintering with the temperature excursion of two-step SPS process

of oxidation and contamination. The sintered Mg_2Si disk is cut into rectangular pillars of $4mm \times 4mm \times 5mm$ by a diamond saw.

To fabricate p-type HMS segment which is for the high temperature leg, Mn (99.9%) and Si (99.9%) were individually put into an alumina jar with alumina balls, and mechanical grinding was carried out in vibration ball milling equipment for 10 hr in Ar atmosphere, where the ball to powder volume ratio was 20:1 The ground powders were blended with a Mn:Si ratio (at%) of 35.5:64.5 in rotary mixer at 100 rpm for 1 hr in Ar atmosphere, then the mixed powders were transferred into the graphite mold of 20 mm diameter. The HMS disk was sintered by SPS process at $900\,^{\circ}C$ and 30 MPa for 15 min in a vacuum. As-sintered HMS was diced into $4mm \times 4mm \times 3.4mm$ by a diamond saw.

As TE segments for low temperature legs, both n-type and p-type Bi-Te based compounds working at low temperature range are purchased from Tellurex Inc. in the shape of $4mm \times 4mm \times 1mm$ and $4mm \times 4mm \times 2.6mm$ respectively.

3.1.2 Characterization

The Seebeck coefficient and electrical conductivity were measured by using a four-point probe measurement system (Ulvac-Rico, ZEM-3). The sample is prepared in the dimension of $2mm \times 2mm \times 10mm$ rectangular bars by dicing the sintered cylinder after SPS process. The five independent measurements were carried out from room temperature up to $300\,^{\circ}C$ for Bi-Te alloys and up to $600\,^{\circ}C$ for high temperature TE legs in vacuum condition. Fig. 3.2 (a) and (b) shows the measured electrical conductivity and Seebeck coefficient of p-type Bi-Te alloys and their average values. In Fig. 3.3, the measured electrical conductivity and Seebeck coefficient of n-type Mg_2Si, (a) and (b), and p-type HMS, (d) and (e), are shown, respectively. The measured TE properties of n-type Bi-Te alloy were offered by the supplier, Tellurex Inc. since it is commercially available while p-type Bi-Te alloy are offered without the measured data due to its custom-made basis.

For thermal conductivity measurements, a sample 10 mm in diameter and 1 mm thick is

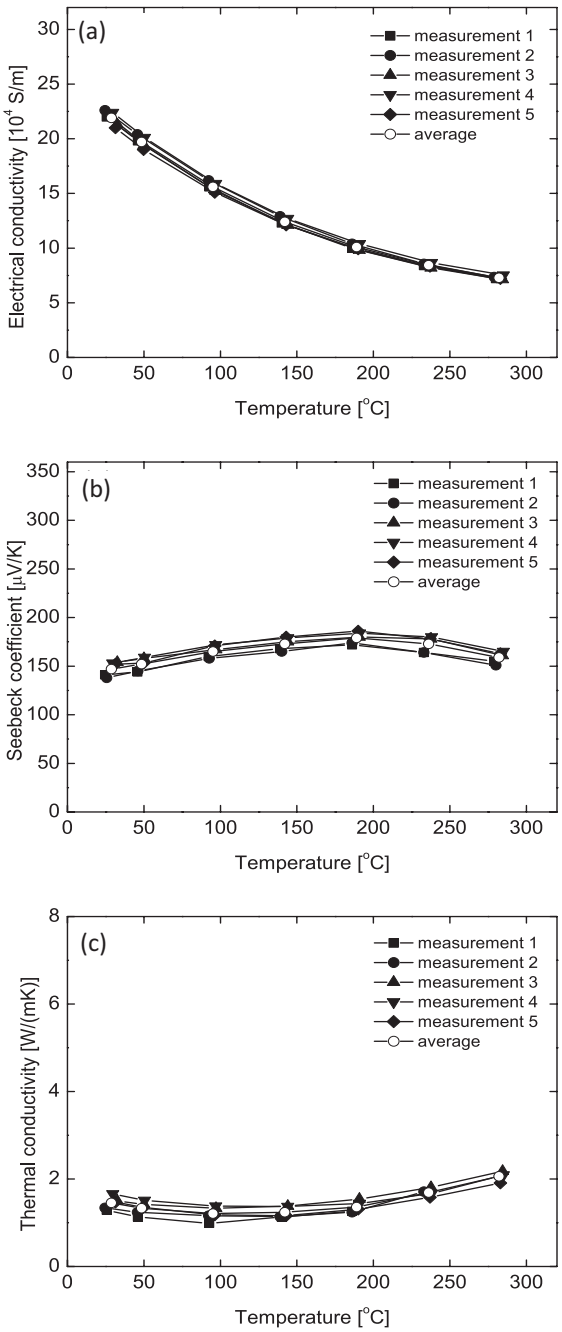

Figure 3.2: Five independent measurements and their average values of TE properties of *p*-type Bi-Te alloy: (a) electrical conductivity, (b) Seebeck coefficient and (c) thermal conductivity

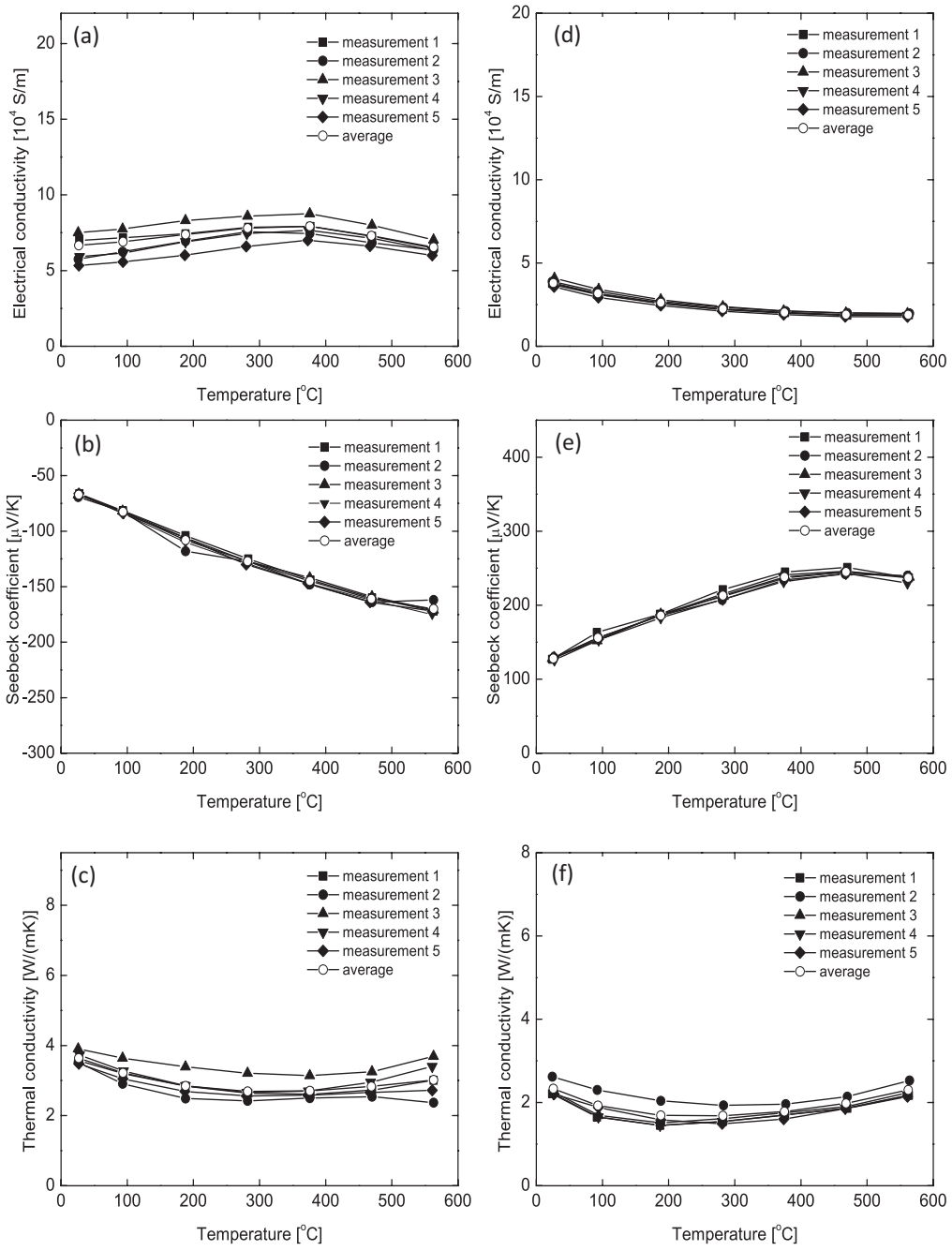

Figure 3.3: Five independent measurements of TE properties of n-type Mg_2Si and p-type HMS: (a) and (d) electrical conductivity, (b) and (e) Seebeck coefficient, and (c) and (f) thermal conductivity, respectively

then prepared for the laser flash measurement system (Ulvac-Rico, TC-9000). This thin disk specimen can be directly obtained by polishing to the target thickness after SPS process. This equipment measures the thermal diffusivity and specific heat capacity of the specimen simultaneously from room temperature to $600\,^{\circ}C$ for the high temperature compounds and from room temperature to $300\,^{\circ}C$ for the Bi-Te based compounds. The thermal conductivity $[W/(mK)]$ can be calculated from the relationship, $\kappa = \alpha \cdot C_p \cdot d$, where α, and C_p are thermal diffusivity $[m^2/s]$ and specific heat capacity $[J/(kgK)]$ respectively, which are measured by TC-9000, and d is mass density $[kg/m^3]$. Fig. 3.2 (c) shows the measured thermal conductivities of p-type Bi-Te alloy, and those of Mg_2Si and HMS are shown in Fig. 3.3 (c) and (f), respectively.

Fig. 3.4 (a)$\sim$(d) show the temperature dependent TE properties, where the TE properties of p-type Bi-Te, n-type Mg-Si and p-type HMS are the average values of five independent characterization measured by the above measurement systems while TE properties of n-type Bi-Te was measured by Tellurex Inc.

3.2 Assembly of π-shaped TE module

Fig. 3.5 (a) illustrates the assembly of the one-pair segmented TE generator in π structure. Let us define the high temperature n-type and p-type legs by n_1 and p_1 and the low temperature n-type and p-type legs by n_2 and p_2. The temperatures of n_1-n_2 interface and the p_1-p_2 interface are determined by intersecting the ZT-Temperature curves of the low temperature TE materials (n_2, p_2) and those of high temperature TE materials (n_1, p_1). The desired interface temperature is $200\,^{\circ}C$ at the n-type junction and $300\,^{\circ}C$ at the p-type junction under the boundary conditions of a hot side at $500\,^{\circ}C$ and a cold side at room temperature. Fig. 3.5 (b) is a thermal resistor network model to predict temperatures at various points through TEG, which will be detailed in the discussion section, later on. Another important design parameter is the length of each segment which has been optimized to achieve the desired temperature gradient across each material. Lengths were calculated

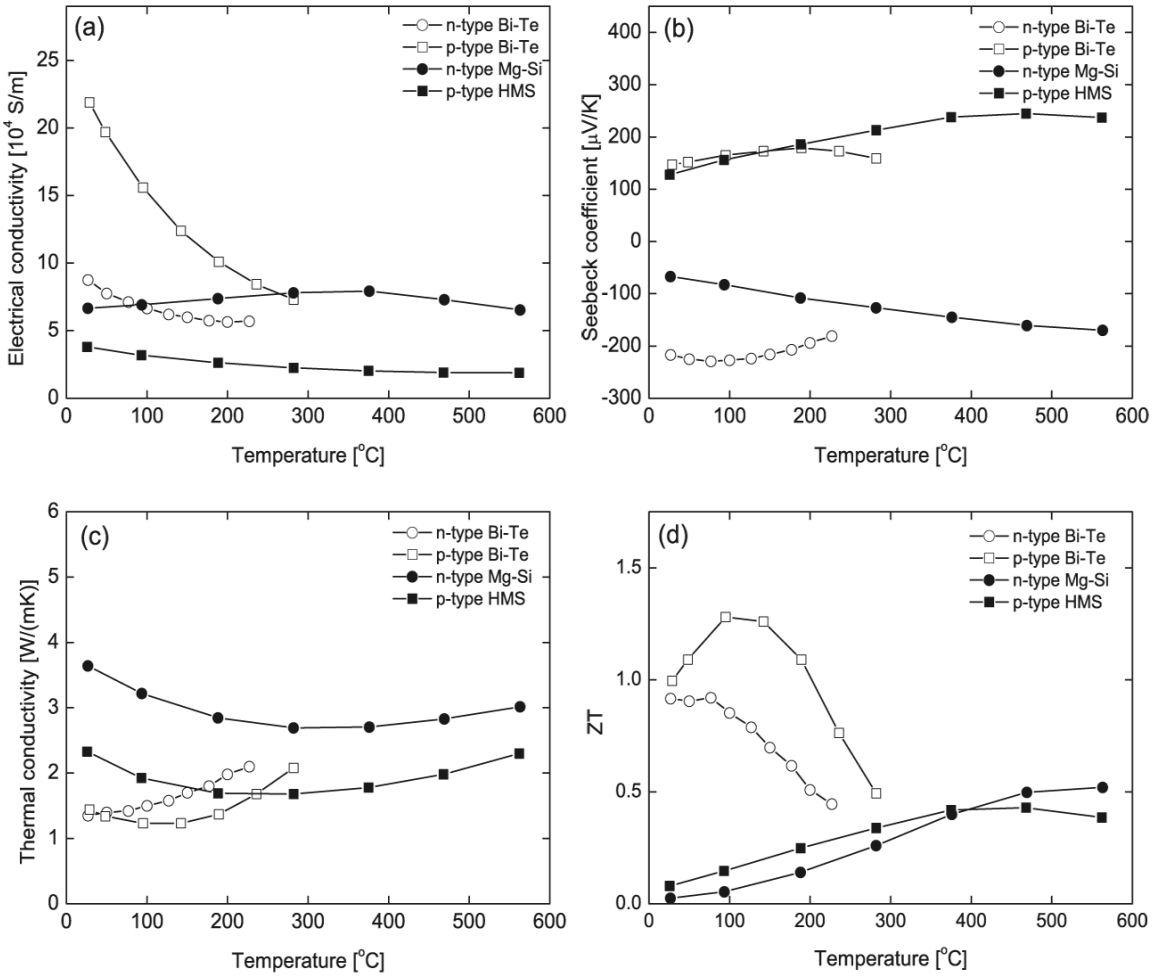

Figure 3.4: Temperature dependent TE properties of n-type Mg_2Si and p-type HMS as high temperature segment, and n-type $Bi_2Te_{3-x}Se_x$ and p-type $Bi_{2-x}Sb_xTe_3$ as low temperature segment: (a) electrical conductivity, (b) Seebeck coefficient, (c) thermal conductivity, and (d) dimensionless the figure of merit, ZT

Alloys	Soldering materials	Bonding layer (A-B)	Processing condition
Alloy 1	Ag-Cu-Sn-Zn	Cu-(n_1, p_1)	680 °C-5min
Alloy 2	Ag-Cd	n_1-n_2, p_1-p_2 and (n_1, p_1)-Cu	425 °C-3min
Alloy 3	Sn-Ag	n_1-n_2, p_1-p_2 and (n_1, p_1)-Cu	250 °C-3min
Alloy 4	Pb-Ag-Sn-In	n_1-n_2, p_1-p_2 and (n_1, p_1)-Cu	350 °C-3min

Table 3.1: The list of all solder materials for bonding interfaces: alloy 4 is the best solder among alloy 2∼4 for low temperature junctions

based on one-dimensional heat conduction law factoring in the difference in thermal conductivity of each segment, which is shown in Appendix A. The combined n-type column is made from 5 mm of Bi doped Mg_2Si and 1 mm of $Bi_2Te_{3-x}Se_x$ while the p-type leg is made from 3.4 mm of HMS and 2.6 mm of $Bi_{2-x}Sb_xTe_3$.

The high temperature TE legs made of Mg_2Si and HMS are brazed to a Cu electrode, and the rest of the segments of TE materials are soldered to each other. Before brazing and soldering processes, it is essential that Ti (50 nm) and Ag (1μm) layers were coated by an E-beam evaporator to increase the interface bonding. Ti is the active element and an ideal adhesion material between the semiconductor blocks and the metal coating layer. Ag has low wetting contact angle which helps the surface stick to the bonding alloys. Table 3.1 shows all solder materials used for bonding these interfaces. All bonding processes were carried out under the gas flowing (2 l/min) environment of 95% Ar and 5% hydrogen to prevent joint interfaces from oxidizing and contaminating during the high temperature process. This design with Ti and Ag adhesive layers ensures lower contact resistance and

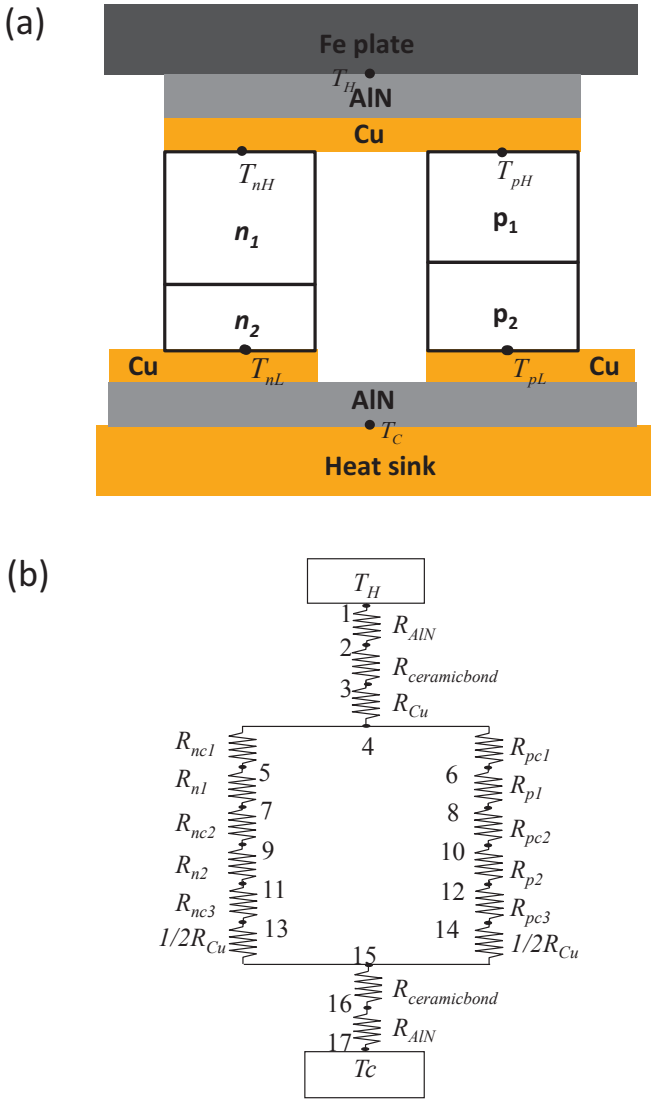

Figure 3.5: The π-shaped TE generator segmented in two TE legs in each column: (a) the illustration of assembled segmented TEG and (b) thermal resistor network model

strong bonding. After assembling the π-shaped TE module, an aluminum nitride (AlN) substrate was attached to the top and bottom sides of the pre-assembled TEG by using a ceramic bond. Since AlN is thermally conductive and electrically insulating material, it transfers heat from the heat source to the TE segments while preventing the system from short circuiting between the adjacent $n-p$ pair.

3.2.1 Contact resistance of bonding interfaces

Electrical contact resistance plays an important role in the segmented TE module generator. High contact resistance between TE segments and at the interface of the metal electrodes would decrease the generator's performance by reducing output power generation. Thus, the minimization of the contact resistances at all interfaces is highly desired. The contact resistance was measured using a four-point probe set up, shown in Fig. 3.6, where two current probes were connected to both ends of a sample to generate current flow through the sample. One voltage probe was located at the end of the Cu electrode while the other voltage probe was scanning along the sample length to detect voltage drop depending on distance between two voltage probes. The electric contact resistance was obtained from Ohm's law based on measured current and detected voltage drops across the bonding interfaces between the fixed and the scanning probe. Fig. 3.7 shows the measured resistance associated with the cross section area of TE segments depending on the distance of two voltage probes. The measured contact resistances at the interface of Cu electrode bonded with n-type and p-type TE segments are 4.8 [$\mu\Omega\ cm^2$] and 3.2 [$\mu\Omega\ cm^2$] at high temperature side, and 43.2 [$\mu\Omega\ cm^2$] and 73.6 [$\mu\Omega\ cm^2$] at low temperature side, respectively. The contact resistance across the interface of high temperature and low temperature TE segments are 75.2 [$\mu\Omega\ cm^2$] for n-type and 94.4 [$\mu\Omega\ cm^2$] for p-type. The measured average value of the electrical contact resistances based on total 6 bonding interfaces in one-pair TE module is 49 [$\mu\Omega\ cm^2$].

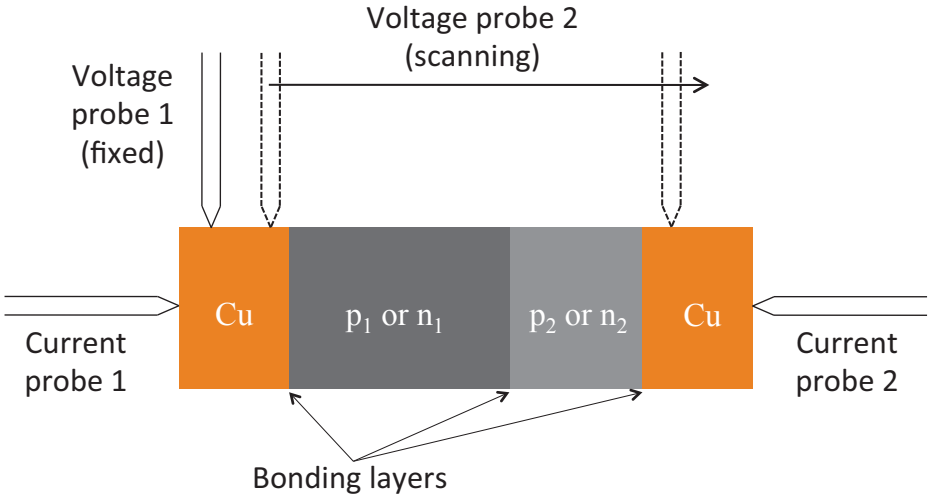

Figure 3.6: The schematic drawing of 4-point-probe method for measuring contact resistance across the junctions

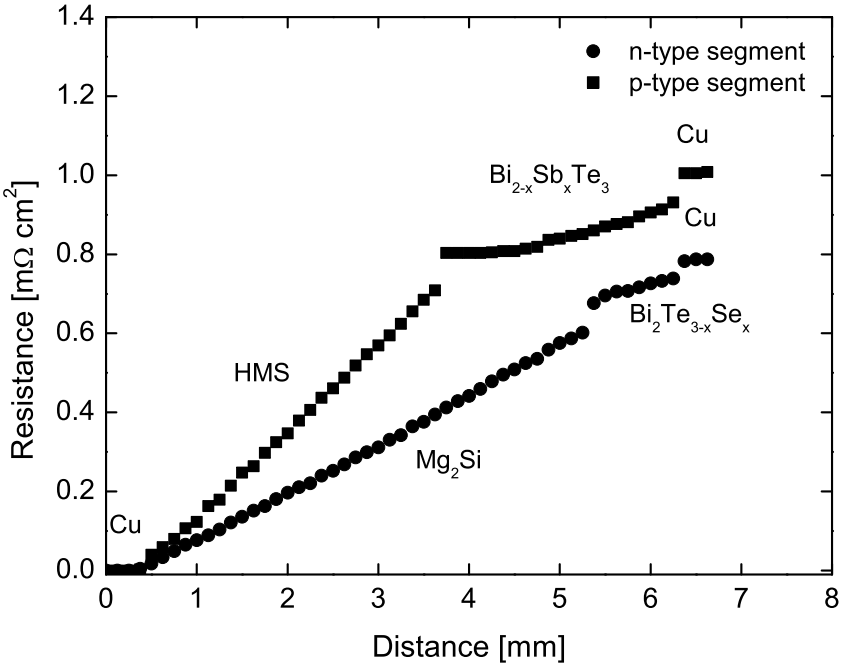

Figure 3.7: Electrical resistance as a function of distance through segmented legs of p-type and n-type columns

3.3 Power measurement test

The assembled TEG was tested for its output power performance under temperature differences (ΔT) of up to 498 $^{\circ}C$. The heat source located at the top of the TE generator is made of two cartridge heaters insulated by magnesium oxide, which are inserted in a metal block. This heat source maintains the hot side temperature (T_H) on top of the TE generator. A heat sink made from a solid block of Cu with a water flow channel inside for tap water circulation maintains the bottom side of the TE device at constant cold temperature (T_C) shown in Fig. 3.5 (a). Under the heater, an Fe plate is inserted to simulate the combustion chamber wall into which the TE generator is integrated to utilize the temperature gap between chamber temperature and outside air. Then the TE module is stacked between the Fe plate and the Cu block on the heat sink. The stacks are surrounded with a 2-inch thick insulation wall made of compressed fiberboard to ensure 1-D vertical heat flow, and thermocouples are inserted at each stacked interface as well as at the Cu electrode to monitor temperatures through heat flow. Fig. 3.8 shows the measurement jig and its set-up.

The measurement tests were carried out under various temperature differences (ΔT) ranging from ΔT= 100 $^{\circ}C$ to 498 $^{\circ}C$. For ΔT=498 $^{\circ}C$, the hot side temperature of the top AlN substrate of the module was set to 521 $^{\circ}C$ while the cold side temperature of bottom AlN substrate was kept below 23 $^{\circ}C$ during the whole measurement process. The measurement at each step of temperature difference was recorded after waiting for steady-state which typically occurred in 10 hr for ΔT=498 $^{\circ}C$. The maximum output power was generated at a half of the open circuit voltage under the matching impedance. Fig. 3.9 shows the output power generation of the module for various ΔT's. At a ΔT of 498 $^{\circ}C$, the maximum output power measured is 0.48 [W] at a load current of 3.4 [A] under a load resistance of 41 [$m\Omega$]. Since the total weight of the two-pair TEG is 11.19 [g], the specific power density, output power per a kilogram, becomes 42.9 [W/kg].

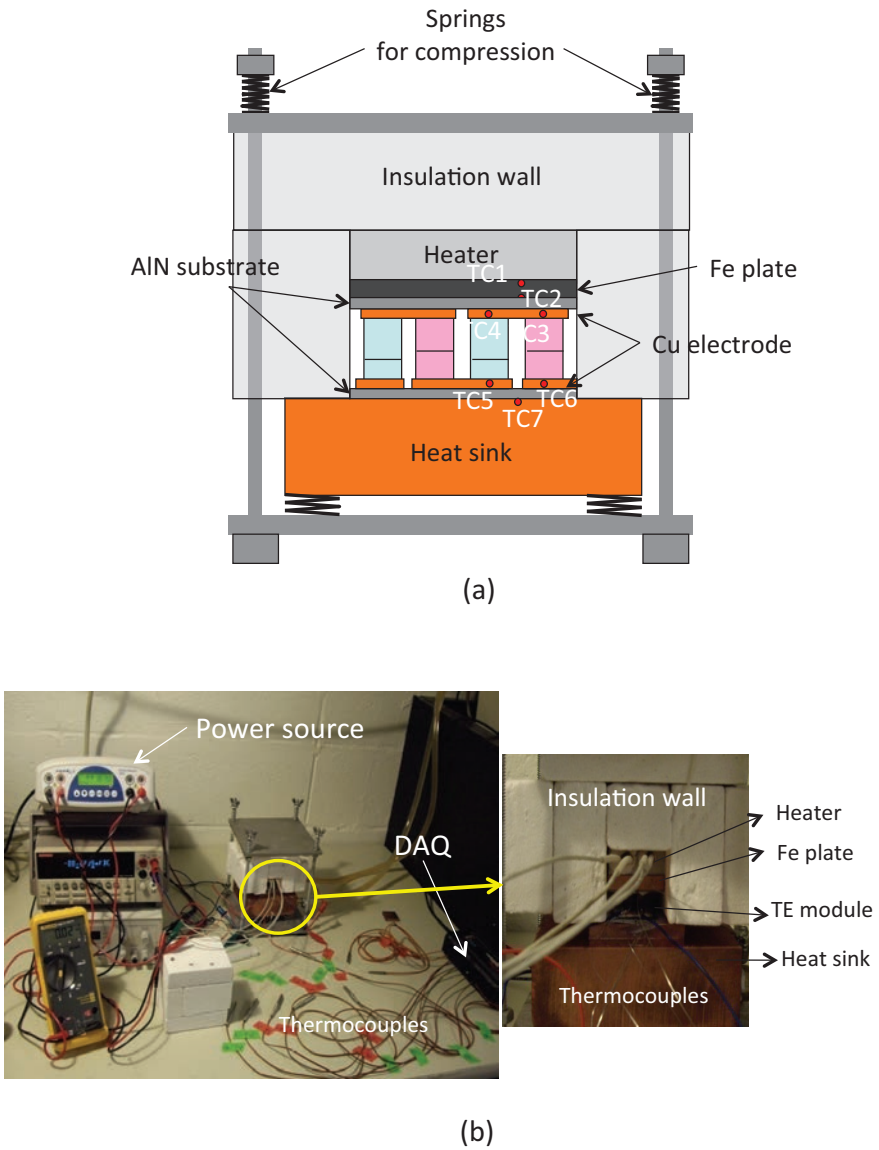

Figure 3.8: The measurement set-up: (a) the illustration of measurement jig where TEG is stacked under compression and (b) photos of measurement setting

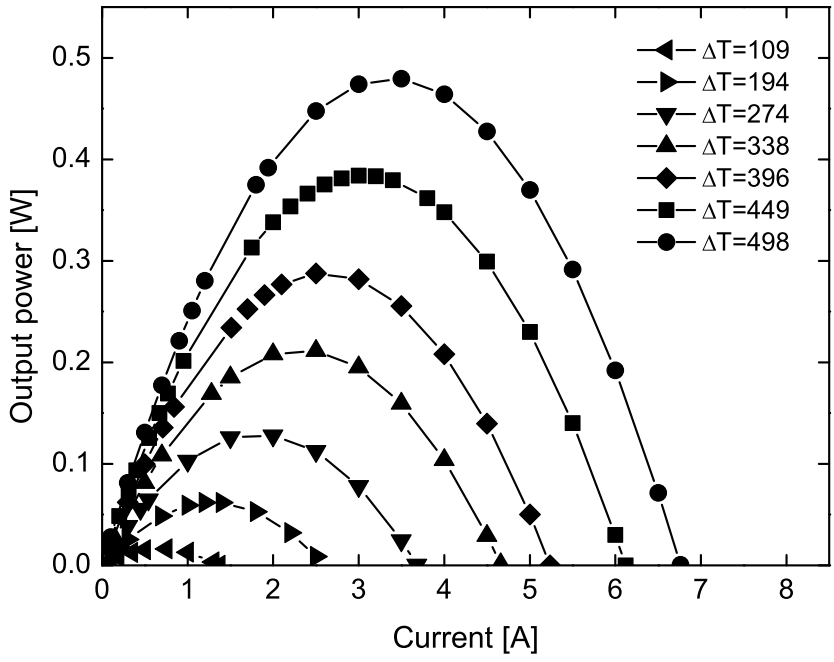

Figure 3.9: The experimental results of two-pair segmented TE module test: Output power generation as a function of load current with various ΔT

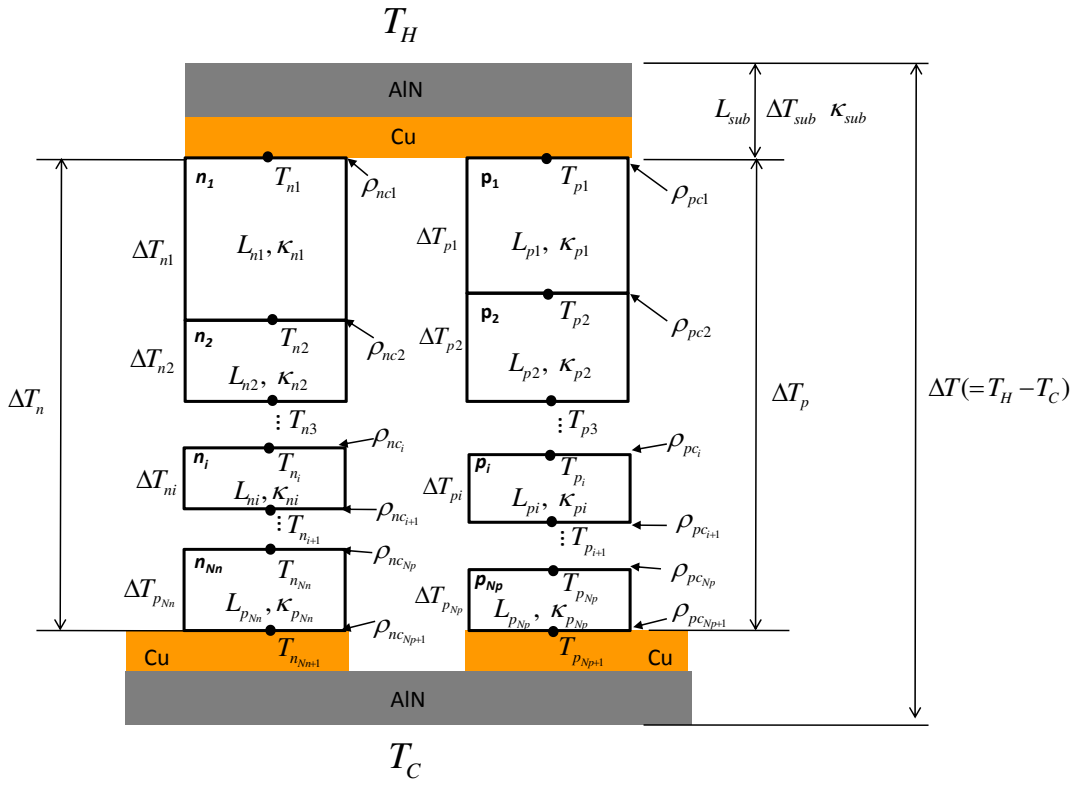

Figure 3.10: The schematic illustration of the general segmented TE module with the number of N_n for n-type leg and N_p for p-type column

3.4 Modeling and verification

3.4.1 Modeling of segmented TEG

The generalized model of segmented TE module is shown in Fig. 3.10, and it is made of combined TE legs consisting of N_n segments of n-type and N_p segments of p-type. The typical TE generator is made by connecting N pairs electrically in series and thermally in parallel. Swanson *et al.* [88] and El-Genk *et al.* [89, 90] have shown a way to estimate the output power generated by segmented TE modules. Min *et al.* [91] considered the effect of electrical contacts on the bonding interface of the metal electrode to TE materials, and also considered temperature drop across ceramic substrate and electrodes in a simple

single leg TEG. By expanding the work of Min *et al.* [91] based on the segmented TEG model [88, 89, 90], this study contributes to construct more reliable model to predict output power generation of the segmented TEG system. The detailed formulation of the model for a segmented TE module with N pairs is given in Appendix B. From Eq. B.8 of Appendix B, open circuit voltage of N pairs is,

$$V_{OC} = N(S_p^M - S_n^M)(T_H - T_C) \tag{3.1}$$

where, S_p^M and S_n^M are the effective Seebeck coefficient of N_p and N_n number of TE elements, respectively, and explicit expressions of and S_p^M and S_n^M are given in Appendix B. From Eq. B.10 in Appendix B, current I obtained by Ohm's law is,

$$I = \frac{N(S_p^M - S_n^M)(T_H - T_C)}{(1+m)\Big[N\Big\{\frac{1}{A_p}\Big(\sum_{i=1}^{N_p}\rho_{p_i}L_{p_i} + \sum_{i=1}^{N_p+1}\rho_{pc_i}\Big) + \frac{1}{A_n}\Big(\sum_{i=1}^{N_n}\rho_{n_i}L_{n_i} + \sum_{i=1}^{N_n+1}\rho_{nc_i}\Big)\Big\} + R_w\Big]} \tag{3.2}$$

where, m is the ratio of load resistance to module resistance, R_L/R. A_p and A_n are the cross sectional areas of the p-type and n-type TE elements respectively. ρ_{p_i}, ρ_{n_i}, ρ_{pc_i} and ρ_{nc_i} are electrical resistivities of the i^{th} p-type and n-type element and contact resistances between the i^{th} and $(i+1)^{th}$ of the p-type and n-type elements respectively. R_w is the electric resistance of lead wires measured experimentally. Generally, the effect of R_w diminishes when N becomes larger, since the internal resistance is relatively much larger than the resistance of the wires, but it cannot be ignored when N is small. The load voltage can be obtained from Eq. 3.1 and 3.2,

$$V = -\left[N\Big(\frac{1}{A_p}\Big(\sum_{i=1}^{N_p}\rho_{p_i}L_{p_i} + \sum_{i=1}^{N_p+1}\rho_{pc_i}\Big) + \frac{1}{A_n}\Big(\sum_{i=1}^{N_n}\rho_{n_i}L_{n_i} + \sum_{i=1}^{N_n+1}\rho_{nc_i}\Big)\Big) + R_w\right]I + V_{OC} \tag{3.3}$$

Thus, output power is obtained as,

$$\begin{aligned} P &= I^2 R_L \\ &= \frac{N(S_p^M - S_n^M)^2 (T_H - T_C)^2 \cdot \dfrac{m}{(1+m)^2}}{\left[\dfrac{1}{A_p}\Big(\sum_{i=1}^{N_p} \rho_{p_i} L_{p_i} + \sum_{i=1}^{N_p+1} \rho_{pc_i}\Big) + \dfrac{1}{A_n}\Big(\sum_{i=1}^{N_n} \rho_{n_i} L_{n_i} + \sum_{i=1}^{N_n+1} \rho_{nc_i}\Big) + \dfrac{R_w}{N}\right]} \end{aligned} \tag{3.4}$$

In this study, it is noted that 2 pairs of TE modules are assembled, i.e., $N = 2$ and two segments are used at each type, i.e., N_p=N_n=2, and $A_p = A_n = A$. The maximum output power can be obtained under $R_L = R$, i.e., $m = 1$. Therefore, output power generation is expressed as,

$$P = \frac{(S_p^M - S_n^M)^2 (T_H - T_C)^2}{\dfrac{2}{A}\left(\sum_{i=1}^{2} \rho_{p_i} L_{p_i} + \sum_{i=1}^{3} \rho_{pc_i} + \sum_{i=1}^{2} \rho_{n_i} L_{n_i} + \sum_{i=1}^{3} \rho_{nc_i}\right) + R_w} \tag{3.5}$$

The efficiency of the module is estimated as,

$$\eta = \frac{T_H - T_C}{T_H}\left[\frac{4}{Z^M T_H} + \frac{2(S_{p_1} T_{p_1} - S_{n_1} T_{n_1})}{(S_p^M - S_n^M) T_H} - \frac{(R_{p_1} + R_{n_1})(T_H - T_C)}{2 R_{tot}^M T_H}\right]^{-1} \tag{3.6}$$

3.4.2 Comparison of experimental data with predictions by the model

The measurement results of two-pair module are compared to the predicted results for validation. Fig. 3.11 shows the measured and predicted $I - V$ curves under ΔT=498 $^\circ C$,

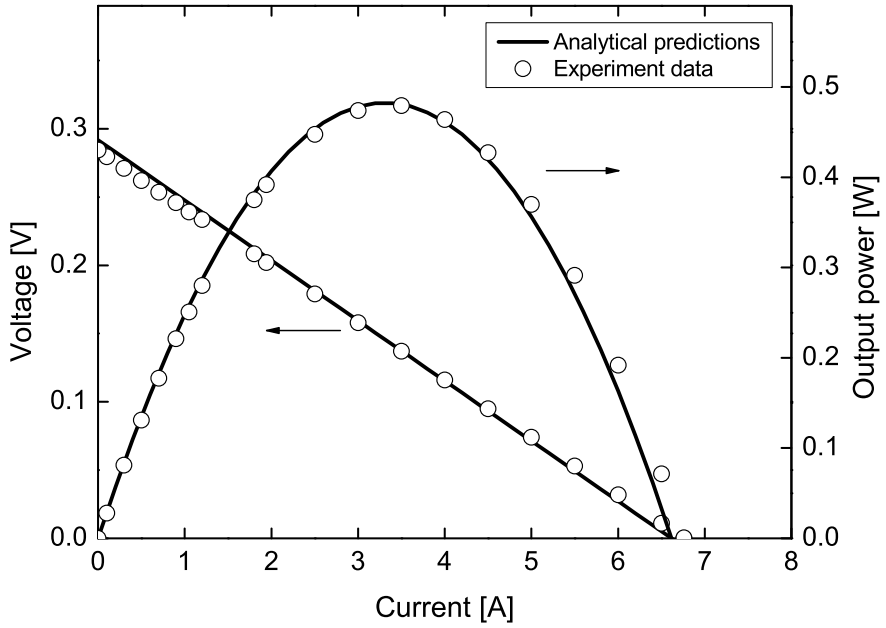

Figure 3.11: Comparison of experimental data with prediction by the model: I-V curve and output power as a function of load current

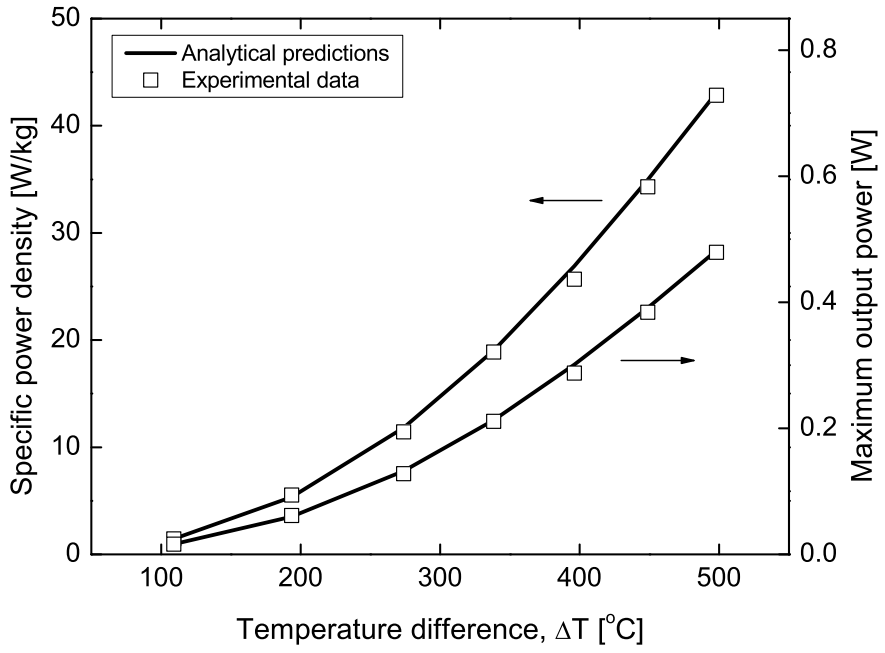

Figure 3.12: Comparison of experimental data with prediction by the model: The maximum output power and the specific power density as a function of ΔT

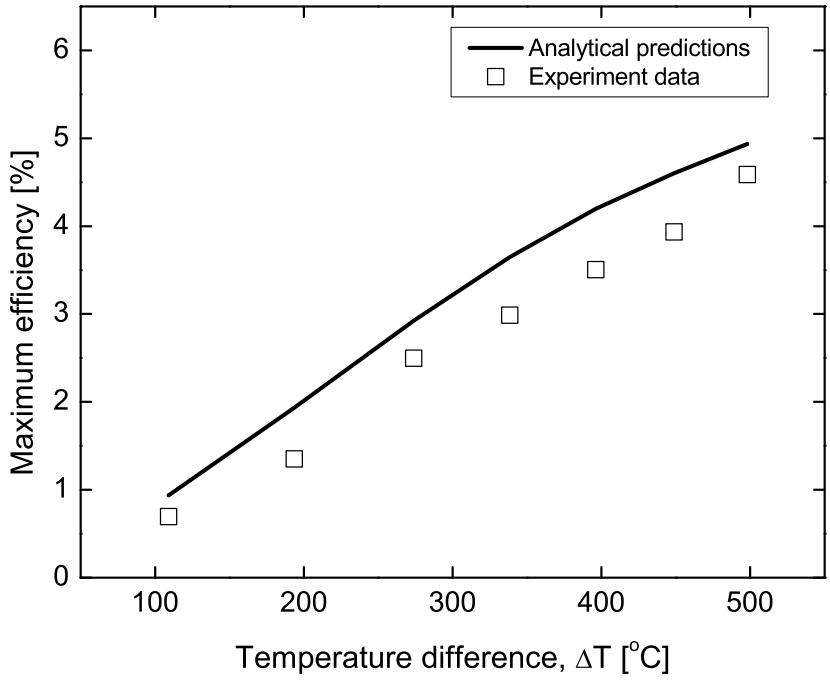

Figure 3.13: Comparison of experimental data with prediction by the model: The maximum efficiency of the module as a function of ΔT. Solid lines are analytical modeling and marks are experimentally measured data

in which the solid line is the predicted results by Eq. 3.3 while the plotted markers are the measured data points. The measured V_{OC} is 285 $[mV]$ and the predicted value is 292 $[mV]$, which is in a good agreement with about 3% difference. The measured I_{SC} of about 6.7 [A] is close to the predicted value of 6.6 [A] within 1% difference. This good agreement is mainly due to low contact resistance at bonding interfaces. The measured internal resistance of two-pair module at room temperature is 23.1 $[m\Omega]$ and the calculated value based on Fig. 3.4 (a) is 22.3 $[m\Omega]$. The maximum power output in Fig. 3.11 is 0.48 $[W]$ and is measured at the load current of 3.4 [A] while the predicted maximum output power is 0.482 $[W]$. This measured value and the theoretical calculation for output power generation are in a good agreement within 1%. As indicated in Fig. 3.12, the generated power and the specific power density are parabolic functions of ΔT $(= T_H - T_C)$ and are in agreement with the predicted power equation, Eq. 3.4. The maximum efficiency of the module as a function of ΔT is illustrated in Fig. 3.13 where the solid line is the prediction by the theoretical model and the square markers are the measured points. The maximum module efficiency is 4.6% measured at ΔT=498 $^\circ C$ and the predicted efficiency by Eq. 3.6 is 4.8%. A comparison between the measured data and predictions by the model demonstrates that the segmented TE module fabrication and its measurement processes were carried out correctly.

3.5 Discussion

Contact resistance is a key factor in determining the output power of TE module design since the electrical contact barriers at the intermediate bonding interfaces of TE segments are larger than that at the junction of TE elements bonded with metal electrodes of hot and cold sides. It is hard to bond directly between semiconductor materials (TE legs) by brazing or soldering, so a thin metal coating is placed on the surfaces before soldering. Fig. 3.14 show the temperature dependent electrical resistivity and Seebeck coefficient measured by four-point probe equipment (Ulvac-Rico, ZEM-3). Two Mg_2Si samples are bonded by using Ag solder with and without thin Ti-Ag coating. The measurement results in Fig. 3.14 (a)

show that the bonding layer with Ti-Ag coating reduces the electrical contact resistance compared with bonding without using a Ti-Ag metal coating while the Seebeck coefficient is not affected by the addition of the thin Ti-Ag metal coating at bonding layer as shown in Fig. 3.14 (b).

Regarding the bonding process for jointing with Cu electrodes, the contact resistance at the hot side and cold side metal junctions are less than 1 [$\mu\Omega\ cm^2$] and 70 [$\mu\Omega\ cm^2$], which are reasonably low compared to the internal resistance of TE materials. Thus, it is important to select the correct brazing or soldering materials working at intermediate temperatures at the junction of Mg_2Si - Bi-Te and HMS - Bi-Te bonding up to $300\,^{\circ}C$. The processing temperature should be quite below $500\,^{\circ}C$ because the melting point of Bi-Te based compound is about $590\,^{\circ}C$. Fig. 3.15 compares the electrical contact resistance across the junction of intermediate bonding layers of n-type and p-type columns along with soldering alloy 2 to 4, see Table 3.1. The horizontal and vertical axes of Fig. 3.15 show the distance and electrical resistance between two voltage probes, respectively. Alloy 2 gives rise to the largest contact resistance, 14.07 [$m\Omega\ cm^2$], due to its high processing temperature which may create micro cracks near the junction area since Bi-Te based compound is very brittle caused by weak van der Waals bonding along the c-direction. Alloy 3 reduces the electrical contact resistance of HMS - Bi-Te interface up to 1.32 [$m\Omega\ cm^2$] by using a low temperature soldering material. However, it is not suitable due to its low melting point, $225\,^{\circ}C$, which is quite lower than the target temperature of $300\,^{\circ}C$ at the intermediate junction. Alloy 4 has a melting temperature of $350\,^{\circ}C$ and gives much lower contact resistance, below 0.1 [$m\Omega\ cm^2$], which is reasonably low compared with the internal resistance of the one-pair module assembly, 11.2 [$m\Omega\ cm^2$]. Therefore, alloy 4 is selected to minimize electrical contact barriers across the intermediate junctions, which enables the smooth resistance over the TE legs as shown in Fig. 3.15. However, the electrical contact resistance across different TE segments is relatively larger than that at the other interfaces of Cu and TE legs at high and low temperature sides. One possible reason is that the metal coating by electron-beam evaporation and TE materials are physically bonded rather than chemical

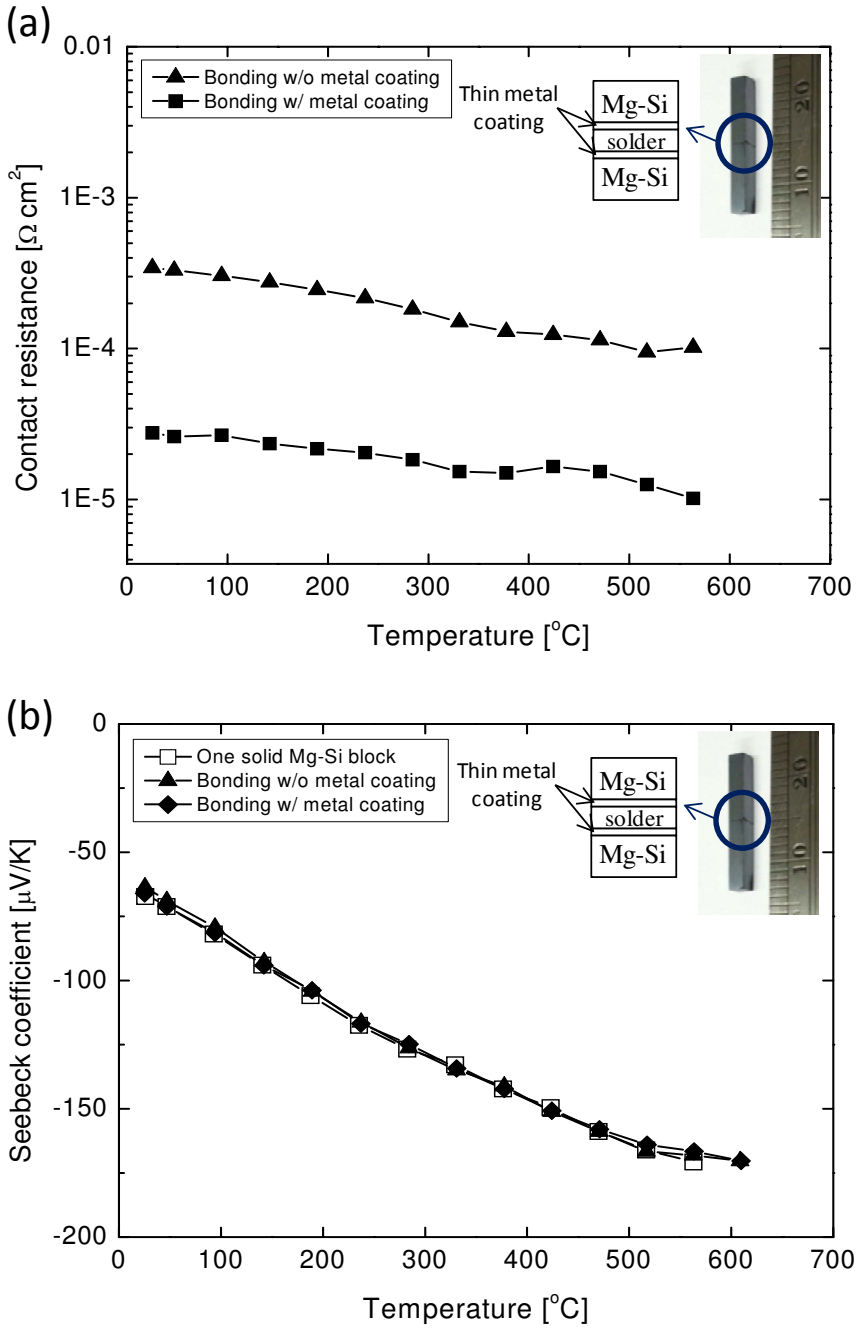

Figure 3.14: The effect of metal coating layer at bonding interfaces: (a) temperature dependent contact resistance and (b) Seebeck coefficient: one solid block, bonding with and without Ti-Ni coating

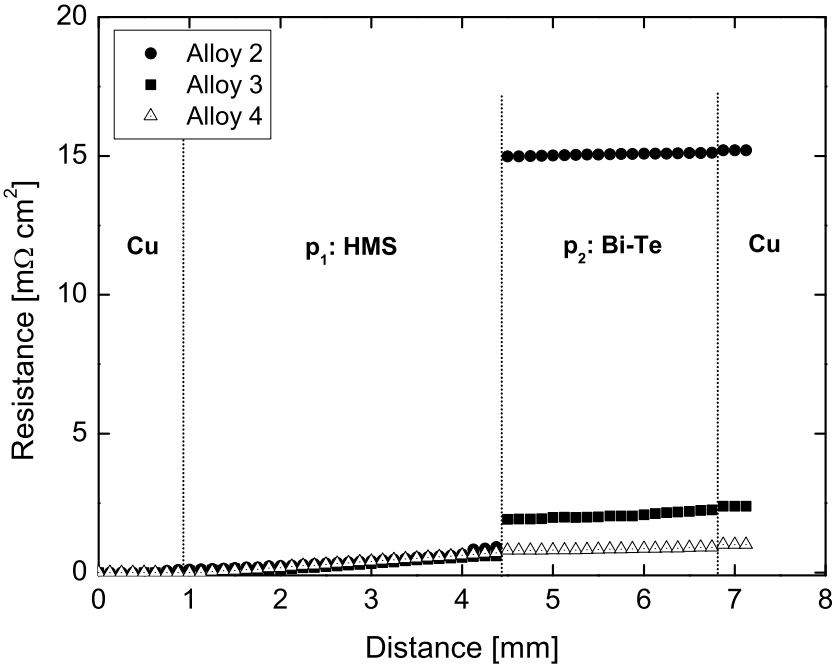

Figure 3.15: The comparison of measured electrical contact resistance of p-type segment with various bonding materials as a function of the distance of two voltage probes

reaction. To reduce the electrical contact resistance between different TE materials, chemical bonding is desired by optimizing to sinter different TE materials at the same time using SPS method. A diffusion barrier is required to prevent unwanted reaction which decreases TE performance. In this study, the limited alloys for brazing and soldering were studied. To minimize the contact resistance at an interface, various alloys need to be examined for optimizing, which will differ in working temperature and types of TE segments.

To verify an agreement of temperature gradient through the TEG, thermal resistor network model [92] of the one-pair π-shaped TEG was built shown in Fig. 3.5 (b) assuming 1-D heat flow, where all contact thermal resistance of bonding interfaces as well as ceramic bonding layers were considered. Thermal resistance R $[W/K]$ is defined by $R = \Delta x/(\kappa A)$, where κ, Δx, and A are thermal conductivity, thickness and cross-section area through which heat is being conducted, respectively [92]. The thermal resistances calculated by the equation above are listed in Table 3.2. The largest thermal resistances of TE legs means the largest temperature drop occurred when heat passed through the TE leg materials. The ceramic bond layer generated the second largest temperature drop in this π TEG. The R_{TEp} is larger than R_{TEn} since the thermal conductivities of the n-type TE legs are larger than those of the p-type legs (see, Fig. 3.4 (c)). The node temperatures at junctions were obtained based on Kirchhoff's junction rule, *i.e.*, $\Sigma Q_i = 0$ at each node i, where the heat flow Q $[W]$ is expressed by $Q = \Delta T/R_{th}$ [92]. From the iteration of this method at 17 nodes, the form of $[Q] = [1/R_{th}][T]$ is calculated where $[1/R_{th}]$ is 17×17 symmetric matrix. The temperatures at the top (T_H) and the bottom (T_C) are known as boundary conditions, so $[1/R_{th}]$ is reduced to 15×15 matrix. By taking the inverse of $[1/R_{th}]$ matrix, the predicted temperatures by thermal resistor network model are obtained, which is plotted in Fig. 3.16.

In addition, 2-D FEM analysis using ANSYS was carried out, in which element type and mesh size were plane55 and 0.25 mm^2, respectively, under $\Delta T = 498\,^{\circ}C$. For more accurate results, the thick insulation wall covering the outside of the assembled TE generator and air gap between n-type and p-type TE legs were taken into account for the FEM analysis. The element type and mesh size of the insulation and air gap were the same as the above.

	ΣR_{AlN}	$\Sigma R_{ceramicbond}$	ΣR_{Cu}	R_{TEp}	R_{TEn}	$\Sigma R_{\rho c}$
Thermal resistance $[K/W]$	0.23	9.4	0.23	231.3	131.5	1.14

Table 3.2: The sub-total thermal resistances of each material, where R_{TEp} and R_{TEn} are the sum of thermal resistance of each p-type and n-type segments, respectively. $\Sigma R_{\rho c}$ is the sum of six solder layers

Fig. 3.16 shows the result of temperatures at various points where T_H, T_{nH}, T_{pH}, T_{nL}, T_{pL} and T_C are defined in Fig. 3.5 (a). The measured net $\Delta T_p (= T_{pH} - T_{pL})$ across p-type column is $435\,^{\circ}C$, and ΔT_p by the thermal resistor network model and ANSYS are $437\,^{\circ}C$ and $428\,^{\circ}C$, respectively. The net ΔT_n in n-type leg by experiment is $412\,^{\circ}C$ and those of thermal resistor network model and ANSYS are $437\,^{\circ}C$ and $413\,^{\circ}C$, respectively. ΔT_p by the experiment is in a good agreement with the results of thermal resistor network modeling and ANSYS analysis within 2%, and regarding ΔT_n 6% difference is shown between the measured temperature gap and the result predicted by the resistor network model. The largest value of temperature gap is obtained by thermal resistor network model due to the assumption of an ideal 1-D heat flow while heat dissipation presumably occurred along the horizontal direction in the experiment and ANSYS analysis is based on 2-D geometry.

The p-type Bi-Te alloy (Tellurex Inc.) shown in Fig. 3.4 has higher electrical conductivity, which gives rise to lower Seebeck coefficient compared with other reported works [29, 93]. The electronic thermal conductivity (κ_{el}) can be obtained by using Wiedemann-Franz law, $\kappa_{el} = L\sigma T$, where L is Lorenz number. The Lorenz number to estimate carrier contribution to the thermal conductivity in p-type Bi-Te alloy is determined based on its electrical conductivity (σ) according to the experimental curve reported by Goldsmid [6], which is 1.5×10^{-8} $[V^2K^{-2}]$ at room temperature. The calculated lattice thermal conductivity (κ_{ph}) by subtracting the electronic contribution from total thermal conductivity is 0.52 [W/mK] at room temperature. In order to explain this low value of κ_{ph} of p-type Bi-Te, we studied its nanostructure by transmission electron microscope (TEM) using FEI Tecnai G2 F20.

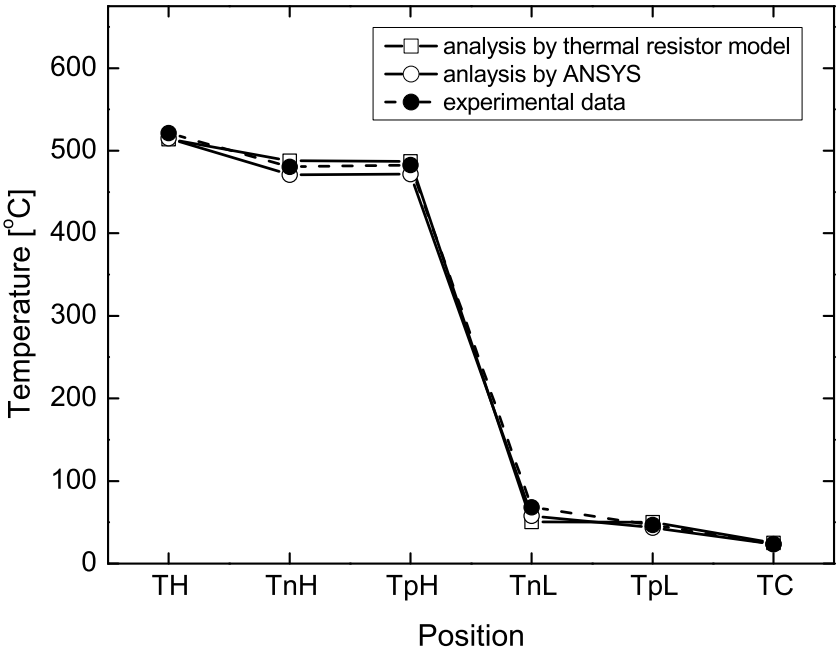

Figure 3.16: The temperature gradient of experimental result and prediction by thermal resistor network model and ANSYS analysis

Fig. 3.17 (a) shows the embedded nanocrystals with the size of 2 to 10 nm. The SAD pattern in the inset confirms randomly oriented nanograins, which is evidenced as ring patterns. The HRTEM image in Fig. 3.17 (b) shows that the nanograins form with different crystalline orientations, each of which shows the periodic lattice structure. Some amorphous precipitates shown in the upper middle of Fig. 3.17 (b) are observed, which is presumably caused by the ion-milling process of sample preparation. The observed nanocrystals are identified as Sb rich phase by energy dispersive spectroscopy (EDS) analysis with the composition of Sb:Te=49:51 in atomic percent, where Bi peak intensity was too low to analyze it while the EDS performed on the entire area of Fig. 3.17 (a) provides us with Bi:Sb:Te=4:30:66. These observations are similar to those of Bi_2Te_3/Sb_2Te_3 nanocomposite processed by Cao *et al.* [94] who mixed two nanocrystalline powders of Bi_2Te_3 and Sb_2Te_3 where they used three different mixing ratios of the former to the latter, 1:2, 1:3 and 1:7. Our data of Bi:Sb:Te=4:30:66 is close to the case of the third mixing case of 1:7, but not exactly matching. The thermal conductivity of Bi_2Te_3/Sb_2Te_3 nanocomposite processed by Cao *et al.* is slightly lower than our data, Fig. 3.4 (a). The electrical conductivity of our p-type Bi-Sb-Te, Fig. 3.4 (b) is higher than that of the Bi_2Te_3/Sb_2Te_3 nanocomposite processed by Cao et al., resulting in the higher ZT ($1.0 \sim 1.3$) over the temperature range of $25 \sim 120\,^{\circ}C$, see Fig. 3.4 (d) than that of the Bi_2Te_3/Sb_2Te_3 nanocomposite processed by Cao *et al.*. The benefit of the nanostructures enables intensive phonon scattering to reduce κ_{ph} without reducing the electrical conductivity, which gives rise to higher ZT value.

In summary, a two-pair segmented TEG was fabricated using Si based, light weight, cost-effective, and non-toxic TE alloys; Mg_2Si for n-type and HMS for p-type. The two-pair segmented TEG can be used as a new propulsion system for a MAV or a waste heat recovery system for a UAV where the proposed π TEG is attached to the surface of a combustion chamber of a MAV or UAV. Bi-Te based compounds are utilized on n-type and p-type segments for low temperature side. A reasonably low average electrical contact resistance of below 50 [$\mu\Omega\ cm^2$] is achieved and the total contact resistance through the module is less than 2% of the internal resistance of the TE materials. The low electrical barriers enable

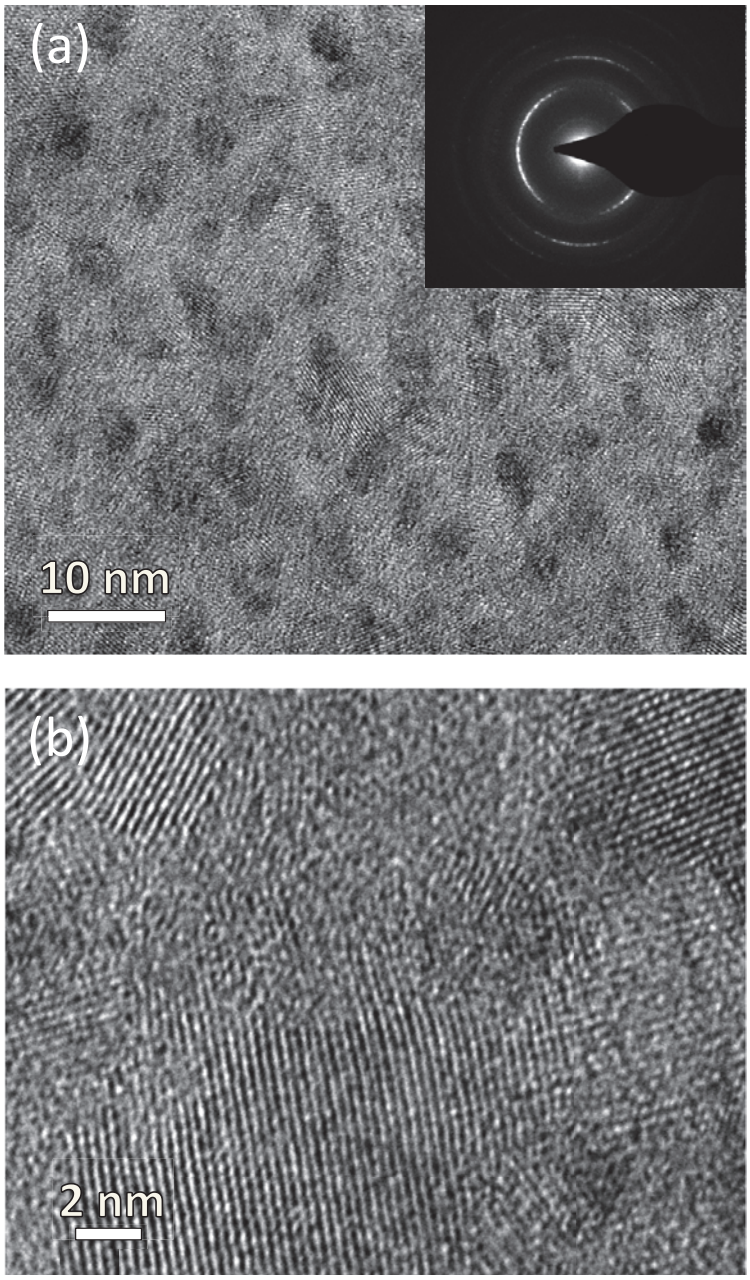

Figure 3.17: TEM/HRTEM images of nanostructures of p-type $Bi_{2-x}Sb_xTe_3$: (a) TEM image showing embedded nanocrystals in a matrix in size of $\sim$10 nm, where EDS for area analysis was carried out covering the area and its SAD pattern in the inset, and (b) HRTEM of a single nanograin which was identified as Sb-rich phase by EDS

the segmented TEG to reach the maximum specific power density of 42.9 $[W/kg]$ under a $498\,^{\circ}C$ temperature difference, which has a good agreement with analytical predictions.

Chapter 4

LINEAR DESIGN OF TEG

As mentioned in Chapter. 1, the conventional TEG is single-stage couples connecting electrically in series and thermally in parallel with π-shape design. To design higher power output, Harman [43] suggested the cascaded design of stacking two or more π-shaped TEGs. TE module at lower legs consisting of TE materials working best for low temperature range generates power from the heat rejected by the upper module based on TE legs operating at high temperature. This design has a disadvantage for weight sensitive applications because extra ceramic substrates and metal electrodes increase the total weight of the device. One way to improve the TE performance as well as to minimize the total weight of the device is the segmented design by dividing the n-type and p-type legs into several segments using different TE materials [44, 45]. However, the π-shaped planar structure becomes unstable if the length of n-type and p-type TE column is not identical, which makes the TEG module weak at high temperature environment. Stockholm [47] introduced a linear design concept of TE module where an electric current flows in a straight line through the TE legs while the electric current in the π-shaped TEG design flows alternatively up and down. Fig. 4.1 compares the linear design with π design. Crane *et al.* [95] showed the aspect ratio of n-type in the linear TEG design can be controlled with that of p-type independently. Sakamoto *et al.* [96] designed a linear-shaped TEG for high temperature range by using only n-type TE element, which has a limit of scaling up by connecting a number of n-type uni-legs electrically in series and thermally in parallel. However, the reported TEGs used bulk Cu or stainless steel as electrodes, which are the main source of increasing the total device's weight. In addition, ceramic substrates on top and bottom sides of the module are still required to avoid short-circuiting.

In this chapter, an advanced design of the segmented linear TEG is proposed for its

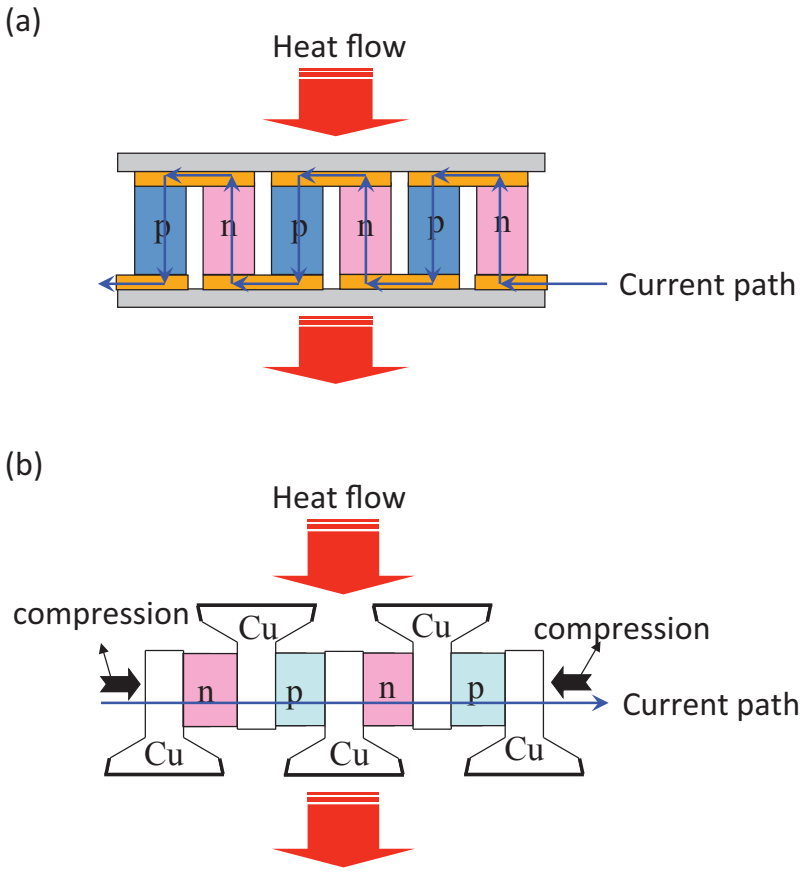

Figure 4.1: π TEG vs. linear TEG design: Electric current flows (a) alternatively up and down along with TE legs in π-shaped TEG, and (b) in straight path in perpendicular to heat flow in linear-shaped TEG

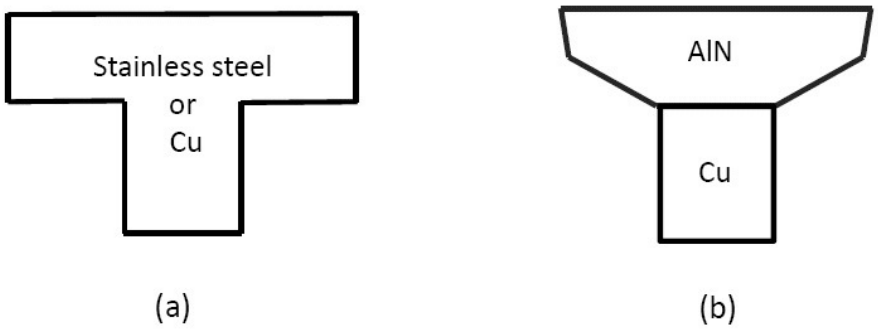

Figure 4.2: Electrodes in linear TE design: (a) conventional T-shaped electrode made of bulk metal, and (b) dovetail-shaped AlN-Cu composite electrode

integration into the walls of a combustion engine system in UAV or automotive engine with two innovative designs: (a) dovetail-shaped electrode based on a composite of Copper (Cu) and Aluminum nitride (AlN), and (b) self-jointing by shrink-fit behavior of Fe-based shape memory alloy (Fe-SMA). As the high temperature TE segments, bulk Mg_2Si of n-type and HMS of p-type are used since they are light-weight, non-toxic and low-cost TE compounds working for high temperature range. In the following, we will discuss linear-shaped TEG design and also its performance as compared with π-shaped TE module.

For accurate comparison with the π-shaped segmented TEG, the same set of TE segments are used to assemble linear-shaped TEG in this chapter. All TE legs in linear-shaped TEG were synthesized and prepared from the same TE materials used in the π-shaped TEG so that the measured TE properties of each segment in Chapter 3 can be utilized to predict the performance of π-shaped and linear-shaped TEGs.

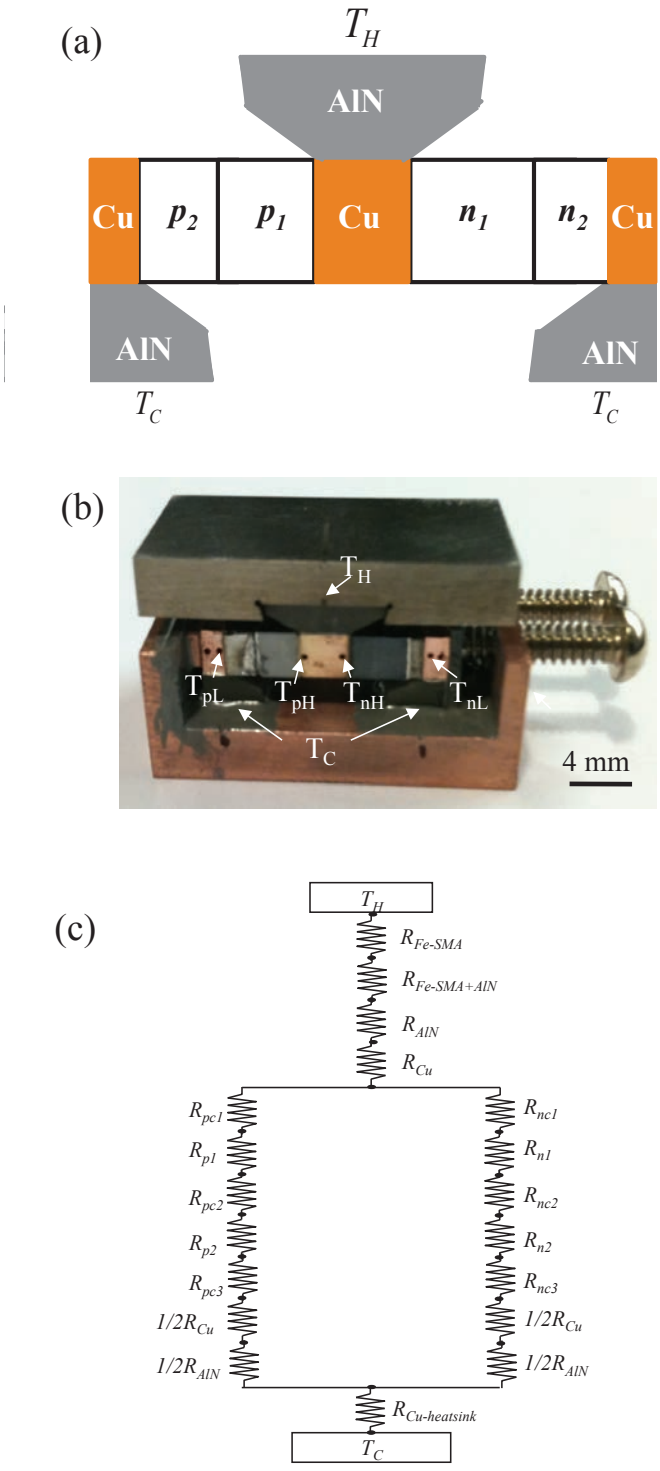

Figure 4.3: The assembly of linear TEG: (a) Schematic figure of the assembled linear-shaped TE module showing full and half shape of AlN-Cu electrodes, (b) assembled linear TEG stacked with Fe-SMA plate and Cu cooling fin, and (c) thermal resistor network model corresponding to (b)

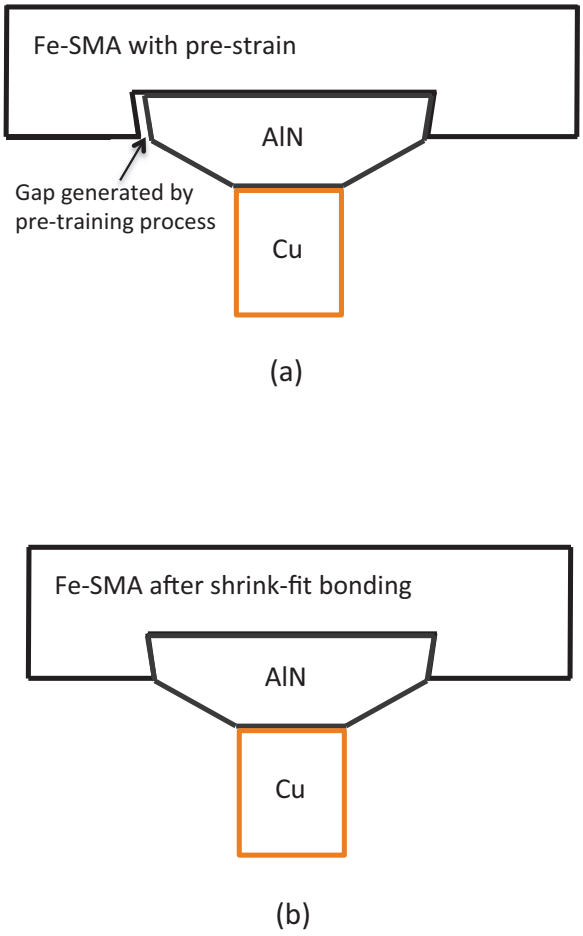

Figure 4.4: Shrink-fit procedure: (a) insertion of dovetail-shaped electrodes into the grooves of pre-trained Fe-SMA, and (b) the completion of shrink-fit by increasing temperature above T_{A_f} of Fe-SMA

4.1 Dovetail-shaped electrode

Conventional electrodes in the linear TE design [96, 97, 98] were made by bulky T-shaped metals of Cu or stainless steel shown in Fig. 4.2 (a), where lower vertical block was only incorporated to pass electric current in a horizontal direction while the top horizontal portion of the T-shaped electrode played a role of absorbing heat energy from a heat source. The new concept of a dovetail-shaped composite electrode proposed in this chapter is to replace the top part of the metal block with AlN ceramic material, see Fig. 4.2 (b), which transfers heat from a heat source effectively to lower Cu part of the T-shape electrode while preventing a short circuit between adjacent $n-p$ pairs, see Fig. 4.3 (a), for AlN is thermally conductor, but insulator electrically. AlN and Cu were brazed by using Ag based brazing filler (Ag-Cu-Ti) at $800\,^{\circ}C$. AlN has much lower mass density (3.26 g/cm^3) than copper (8.94 g/cm^3) and stainless steel (8.03 g/cm^3) so that the total weight of fully assembled linear TEG using the composite electrodes becomes lighter than that of conventional linear TEGs.

Another feature of the proposed AlN-Cu electrode has an angle in upper AlN part. In Fig. 4.3 (a), the upper angled edge of AlN cooperates in a shrink-fitting assembly to be integrated into a combustion chamber's wall made of Fe based SMA (Fe-SMA), see Fig. 4.4 (a) and (b). As shown in Fig. 4.3 (b), a half shape of AlN-Cu electrodes are required for the complete TE module assembly, which are placed at the far ends of right and left sides. A compressive force is applied horizontally on the flat end of the half shape electrodes is important for the compressive force to be applied horizontally so that both thermal and electrical resistances at the interfaces can be minimized and heat flows to the cold side of the TEG, the bottom Cu block shown in Fig. 4.3 (b). The thermal resistor network model of the linear TEG was constructed as shown in Fig. 4.3 (c), which will be discussed in the Discussion section.

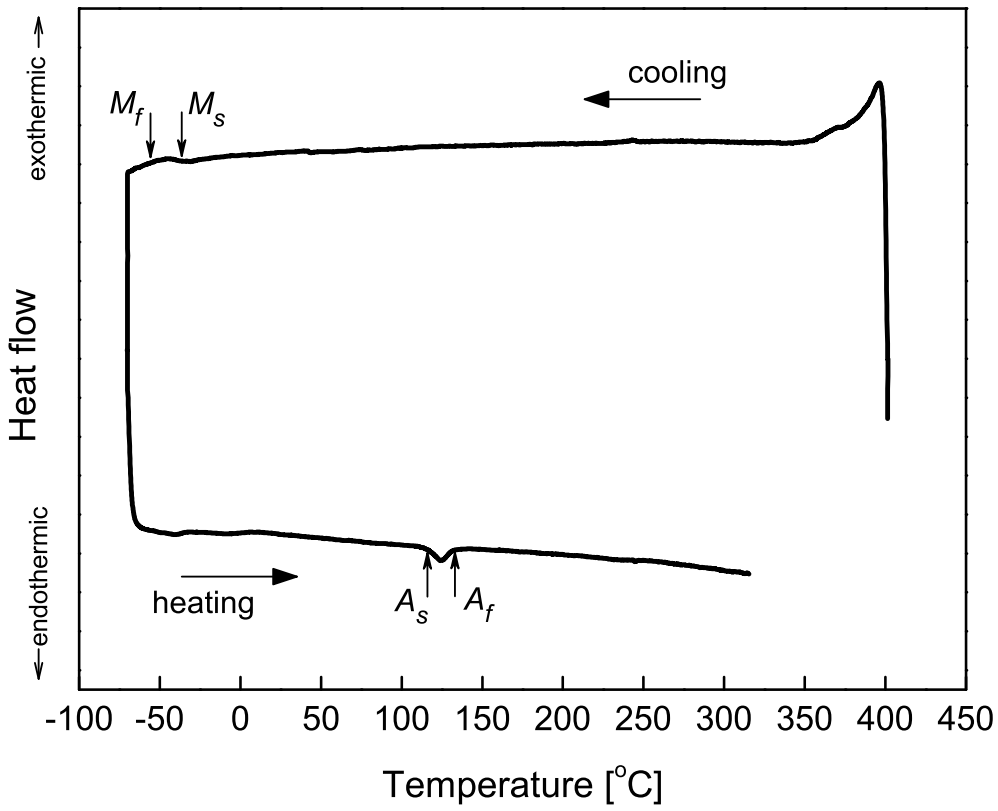

Figure 4.5: DSC chart showing T_{Ms}, T_{Mf}, T_{As}, and T_{Af}

4.2 Fe-SMA for the shrink-fit integration

The concept of new integration method is that the AlN part of the dovetail-shaped electrode is inserted into the groove of the combustion chamber's wall which is made of low-cost Fe-Si-Mn-Cr SMA (Fe-SMA) [99]. As-received Fe-SMA plate from the supplier (Awaji Materia Co., LTD, Japan) was characterized to examine the transformation temperatures; martensite start temperature (T_{Ms}), martensite finish temperature (T_{Mf}), austenite start temperature (T_{As}), and austenite finish temperature (T_{Af}) by differential scanning

calorimeter (DSC) from $-70\,^{\circ}C$ to $400\,^{\circ}C$, which was measured under no applied stress, so the transformation was not stress induced. Fig. 4.5 is the DSC results of this Fe-SMA showing the weak peaks as compared with TiNi-SMA. From the DSC results the endothermic peak was observed around $125\,^{\circ}C$ on the heating curve, where T_{As} and T_{Af} were found as $115\,^{\circ}C$ and $135\,^{\circ}C$, respectively. The exothermic peak on the cooling path was detected around at $-50\,^{\circ}C$ but T_{Ms} and T_{Mf} were not clearly shown. Since the transformation to the martensite phase occurs much below room temperature, Fe-SMA after the shrink-fit assembly by heating above T_{Af} and cooling down to room temperature is still the austenite phase, which means no phase transition occurs at the operation temperature range of TEG, room temperature to $500\,^{\circ}C$.

In order to obtain the correct shape memory strain during the shrink-fit joining of the dovetail-shaped electrode and Fe-SMA plate, 6% tensile strain was applied to as-received Fe-SMA plate. This prestraining was repeated again to secure larger recovery strain of up to 3.5%. Then, the prestrained Fe-SMA plate is subjected to shape memorization process, *i.e.*, annealing at $600\,^{\circ}C$ for 2 hr with the heating rate of $10\,^{\circ}C/min$ under the gas flowing ($1\ l/min$) environment of 95% Ar and 5% hydrogen, then it was cooled down to room temperature. Then, the Fe-SMA was machined with groove, see Fig. 4.4 (a), followed by insertion of the top AlN part of the dovetail-shaped electrodes into the grooves of the Fe-SMA plate, see Fig. 4.4 (a). Heating up to temperature above T_{Af} led to a shrink-fit assembly of the dovetail-shaped AlN-Cu electrodes with Fe-SMA plate, Fig. 4.4 (b). The compressive strain of Fe-SMA plate for the shrink-fit joining can be optimized by joining the length of the groove. To this end, various shrink-fit strains were applied. If the shrink-fit strain is not optimized, cracks could occur at the end of shrink-fit assembly, for example, the use of larger than 0.3% compression led to such cracking emanating from the sharp corners of the grooves. It was found that 0.1% of the fitting strain enables the assembly to be crack free, see Fig. 4.6 where the corner ends of the machined groove were rounded to avoid the stress concentration due to the sharp corner of AlN parts. This shrink-fit bonding is expected to be much more durable compared to solder based bonding which is prone to failure due to

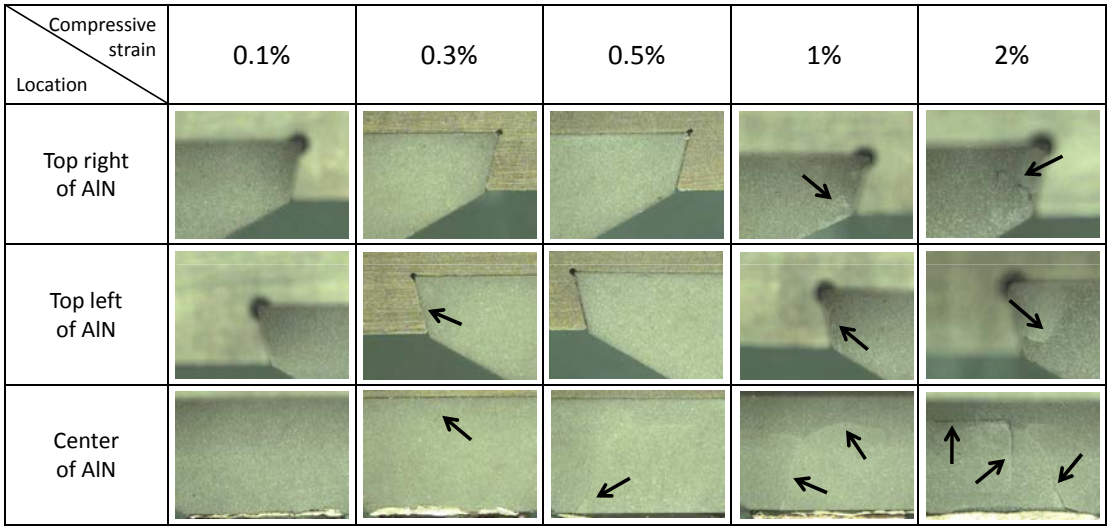

Figure 4.6: The optimization of assembling strain at the shrink-fitting process, where use of various strains from 0.1% to 2% are used

the vibration-induced cracking soldered region.

4.3 Two-pair TEG fabrication and the output power measurement

The high temperature TE legs made of Mg_2Si and HMS were brazed to a Cu block of the dovetail-shaped at $680\,^{\circ}C$ for 5 min using Ag-Cu-Sn-Zn soldering materials. The pre-assembled parts were inserted into the grooves of Fe-SMA plate, and then the shrink-fitting was carried out at $350\,^{\circ}C$ for 30 min with the heating rate of $10\,^{\circ}C/min$. After cooling down to room temperature naturally, soldering was achieved between the low temperature TE legs (n_2, p_2) and the high temperature TE legs (n_1, p_1) under applied compression, and the half shape of Cu-AlN electrodes were also soldered to n_2 and p_2 legs using Pb-Ag-Sn-In soldering materials at $350\,^{\circ}C$ for 5 min. It is essential that Ti (50 nm) and Ag (1 μm) layers were thinly pre-coated on the bonding surfaces of each TE segment prior to the soldering since Ti is an ideal adhesion material, and Ag has low wetting contact angle, which ensures lower

contact resistance and strong bonding. All brazing and soldering processes were carried out under the gas flowing (2 l/min) environment of 95% Ar and 5% hydrogen to prevent joint interfaces from being oxidized and contaminated during the high temperature bonding process. It is highly desired to minimize the electrical contact resistances of linear TE legs since the larger contact resistance degrades TEGs performance by reducing its output power generation [100]. The voltage drops across the bonding interfaces were measured using a four-point probe method, and the electric contact resistance is obtained from Ohm's law. The measured contact resistances at the interface of Cu electrode bonded with n-type and p-type TE segments are 3.2 [$\mu\Omega\ cm^2$] and 52.8 [$\mu\Omega\ cm^2$] at high temperature side, and 28.8 [$\mu\Omega\ cm^2$] and 59.2 [$\mu\Omega\ cm^2$] at low temperature side, respectively.

The heat source made of two cartridge heaters was inserted into Al block, and a solid Cu block with a water flow channel inside for water circulation was inserted to the bottom Cu block, see Fig. 4.3 (b). A compression loading jig of bolts (shown in Fig. 4.3 (b)) was applied horizontally the linear TEG where thin AlN plates were inserted between the half shape electrodes and side supports of the bottom Cu block to avoid a short circuit. Fig. 4.3 (b) shows the developed linear-shaped TEG combined with the cooling fin under the compression in horizontal direction. This assembly was insulated by 2-inch thick fiberboard to ensure 1-D heat flow vertically while the electric current flowed horizontally, and thermocouples were installed at each bonding interface to monitor temperatures. The output power was measured under the temperature difference ($\Delta T = T_H - T_C$) varied as high as $\Delta T = 497\,^{\circ}C$, where the hot side temperature (T_H) at the AlN part of dovetail-shaped electrode was set to $523\,^{\circ}C$ while the cold side temperature (T_C) of the bottom AlN at the half shape of Cu-AlN electrode was maintained as low as $26\,^{\circ}C$. Fig. 4.7 shows the results of the output power generated by the linear TEG at various ΔTs. The maximum output power measured at $\Delta T = 497\,^{\circ}C$ is 0.513 [W] at a load current of 3.38 [A] under a load resistance of 45 [$m\Omega$]. The specific power density was calculated to be 89.2 [W/kg] by dividing the power out by the total weight of the two-pair linear-shaped TEG excluding Fe-SMA plate, which is 5.75 [g].

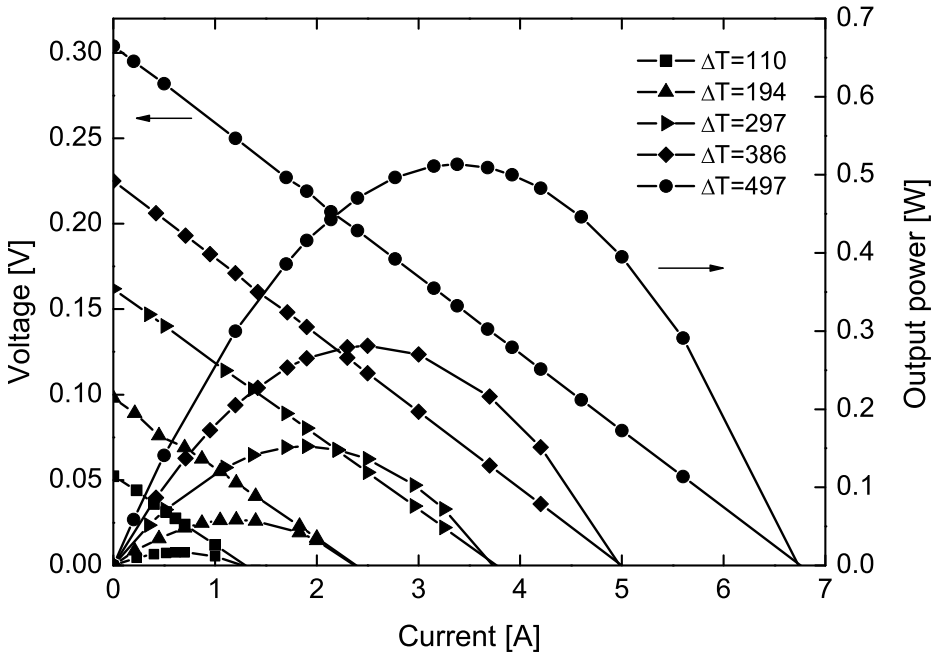

Figure 4.7: The experimental results of two-pair linear TEG test: I-V curve and output power generation as a function of load current with various ΔT.

4.4 Comparison of experimental data with predictions by the model

In Chapter 3, the generalized analytical model was constructed to estimate output power generated by the segmented TEG incorporating the effect of the ceramic substrate and electrical contacts at the interface of TE segments and metal electrodes. From this model, the load voltage is,

$$V = -\left[\frac{2}{A}\left(\sum_{i=1}^{2}\rho_{p_i}L_{p_i} + \sum_{i=1}^{3}\rho_{pc_i} + \sum_{i=1}^{2}\rho_{n_i}L_{n_i} + \sum_{i=1}^{3}\rho_{nc_i}\right) + R_w\right]I + V_{OC} \tag{4.1}$$

ρ_{p_i}, ρ_{n_i}, ρ_{pc_i} and ρ_{nc_i} are electrical resistivities of p-type and n-type element and contact resistances between the i^{th} and $(i+1)^{th}$ of the p-type and n-type elements respectively. L_{p_i} and L_{n_i} are the length of each i^{th} segment, and V_{OC} is open circuit voltage. R_w is the electric resistance of lead wires measured experimentally.

The output power of two pairs in the linear-shaped TEG is,

$$P = \frac{2(S_p^M - S_n^M)^2(T_H - T_C)^2 \cdot \dfrac{m}{(1+m)^2}}{\left[\dfrac{1}{A}\left(\displaystyle\sum_{i=1}^{2}\rho_{p_i}L_{p_i} + \sum_{i=1}^{3}\rho_{pc_i} + \sum_{i=1}^{2}\rho_{n_i}L_{n_i} + \sum_{i=1}^{3}\rho_{nc_i}\right) + \dfrac{R_w}{2}\right]} \tag{4.2}$$

where, m is defined as R_L/R. S_p^M and S_n^M are the effective Seebeck coefficient. The explicit expressions of S_p^M and S_n^M are,

$$S_p^M = \frac{\displaystyle\sum_{i=1}^{2} S_{p_i}\frac{\kappa_p^E L_{p_i}}{\kappa_{p_i}L_p}}{\displaystyle\sum_{i=1}^{2}\frac{\kappa_p^E L_{p_i}}{\kappa_{p_i}L_p} + \frac{\kappa_p^E L_{sub_C}}{\kappa_{sub_C}L_p} + \frac{\kappa_p^E L_{sub_H}}{\kappa_{sub_H}L_p}}, S_n^M = \frac{\displaystyle\sum_{i=1}^{2} S_{n_i}\frac{\kappa_n^E L_{n_i}}{\kappa_{n_i}L_n}}{\displaystyle\sum_{i=1}^{2}\frac{\kappa_n^E L_{n_i}}{\kappa_{n_i}L_n} + \frac{\kappa_n^E L_{sub_C}}{\kappa_{sub_C}L_n} + \frac{\kappa_n^E L_{sub_H}}{\kappa_{sub_H}L_n}} \tag{4.3}$$

κ_p^E and κ_{p_i} are effective thermal conductivity of all combined p-type leg and thermal conductivity of i^{th} segment, respectively. L_p and L_n are total length of each combined leg. κ_{sub_H}, L_{sub_H} and ΔT_{sub_H} are the effective thermal conductivity, length, and temperature drop of the combined layer consisting of Fe-SMA plate, shrink-fit joint layer, and dovetail-shaped electrode at high temperature, respectively. κ_{sub_C}, L_{sub_C} and ΔT_{sub_C} are the same as the above at low temperature. ΔT_p and ΔT_{p_i} are the temperature difference through the combined p-type column and the temperature difference across i^{th} segment of p-type, respectively.

The efficiency of the linear-shaped TEG is,

$$\eta = \frac{T_H - T_C}{T_H}\left[\frac{4}{Z^M T_H} + \frac{2(S_{p_1}T_{p_1} - S_{n_1}T_{n_1})}{(S_p^M - S_n^M)T_H} - \frac{(R_{p_1} + R_{n_1})(T_H - T_C)}{2R_{tot}^M T_H}\right]^{-1} \tag{4.4}$$

where R_{tot}^M is effective electrical resistance of 1-pair,

$$R_{tot}^M = \frac{1}{A_p}\left(\sum_{i=1}^{2}\rho_{p_i}L_{p_i} + \sum_{i=1}^{3}\rho_{pc_i}\right) + \frac{1}{A_n}\left(\sum_{i=1}^{2}\rho_{n_i}L_{n_i} + \sum_{i=1}^{3}\rho_{nc_i}\right) + \frac{R_w}{N} \tag{4.5}$$

K_p^M and K_n^M are effective thermal conductance of p-type and n-type legs respectively.

$$K_p^M = \frac{K_p^E}{\sum_{i=1}^{2}\frac{\kappa_p^E L_{p_i}}{\kappa_{p_i}L_p} + \frac{\kappa_p^E L_{sub_C}}{\kappa_{sub_C}L_p} + \frac{\kappa_p^E L_{sub_H}}{\kappa_{sub_H}L_p}},\ K_n^M = \frac{K_n^E}{\sum_{i=1}^{2}\frac{\kappa_n^E L_{n_i}}{\kappa_{n_i}L_n} + \frac{\kappa_n^E L_{sub_C}}{\kappa_{sub_C}L_n} + \frac{\kappa_n^E L_{sub_H}}{\kappa_{sub_H}L_n}} \tag{4.6}$$

and, Z^M is module figure of merit which is defined as,

$$Z^M = \frac{(S_p^M - S_n^M)^2}{R_{tot}^M(K_p^M + K_n^M)} \tag{4.7}$$

Fig. 4.8 and Fig. 4.9 show the measured and predicted curves under $\Delta T = 497\,^\circ C$. The solid lines are the calculated predictions based on Eq. 4.1 and Eq. 4.2, and the plotted markers are the measured data by experiment. In Fig. 4.8, the measured V_{OC} is 304 $[mV]$ and the predicted value is 314 $[mV]$, which is in a good agreement within 3%. The maximum power output, 0.513 $[W]$ is measured at the load resistance of 44.9 $[m\Omega]$ while the maximum output power by the analytical model is 0.517 $[W]$. This measured value and

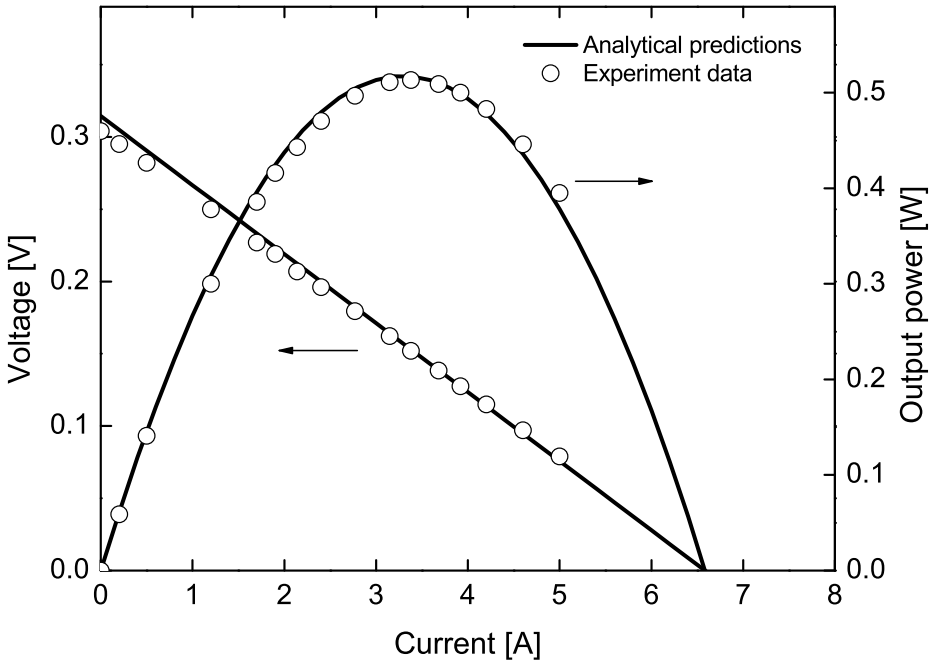

Figure 4.8: Comparison of experimental data with prediction by the model: I-V curve and output power as a function of load current

the theoretical calculation for output power generation are in a good agreement within 1%. Fig. 4.9 shows the maximum output power and efficiency as a function of $\Delta T(= T_H - T_C)$. The generated power is parabolic functions of ΔT and the measured value is in an agreement with the predicted power equation, Eq. 4.2 when m=1 for the impedance matching. The maximum module efficiency is 3.6% measured at $\Delta T = 497\,^{\circ}C$ and the predicted value by Eq. 4.4 is 4.3%. A good agreement between the measured data and predictions by the model indicates that the segmented linear-shaped TEG fabrication and its measurement processes were carried out correctly.

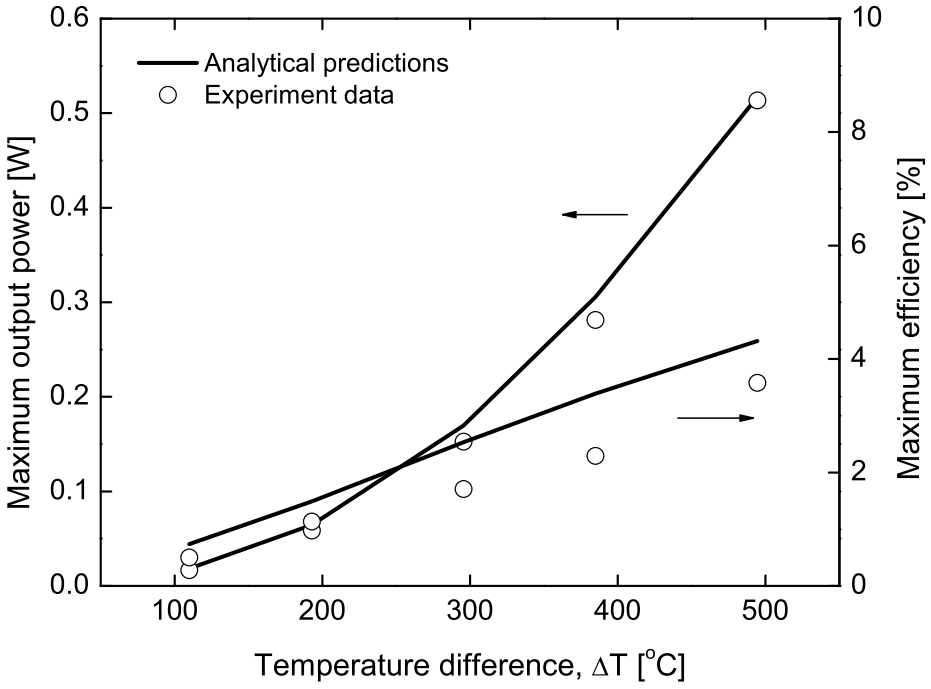

Figure 4.9: Comparison of experimental data with prediction by the model: The maximum output power and module efficiency as a function of ΔT

4.5 Discussion

Fig. 4.10 through Fig. 4.15 show the comparison between measured data of the typical π-shaped TEG in Chapter 3 and the linear-shaped TEG proposed in this Chapter, where the same TE materials are used. The solid lines in Fig. 4.10 show the temperature difference only through TE segments as a function ΔT, where ΔT_n and ΔT_p are the measured temperature gap across the combined n-type and p-type column, respectively. The marker in square indicates n-type and that in circle is p-type, and the solid and hollow markers mean the linear TEG and π-shaped TEG data, respectively. The dotted line is the measured V_{OC}, where the solid and hollow triangles indicate the linear TEG and the π-shaped TEG. It is noted in Fig. 4.11 that the larger temperature gradient through TE legs in the linear design was induced than that in the π-shaped TEG. This is mainly because of the reduced thermal resistance thank to the use of AlN-Cu composite electrode and shrink-fit integration method in the linear TEG design. Fig. 4.11 shows the measured temperature values (solid markers) when $\Delta T = 500\,^{\circ}C$, and the numerical results by ANSYS (hollow markers). The conditions used for the FEM thermal analysis based on ANSYS are as follows: (1) element type: plane55, (2) mesh size: 0.25 mm square, and (3) temperature boundary conditions: $T_H = 525\,^{\circ}C$ and $T_C = 25\,^{\circ}C$ for $\Delta T = 500\,^{\circ}C$. The temperature gradient results of π-shaped and linear TEG are shown in Fig. 4.12 and Fig. 4.13, respectively. The ceramic materials covering TEG set for insulation and the space filled with air between the top Fe-SMA plate and the bottom Cu block were taken into account for the accurate thermal analysis. The solid and dashed lines denoting the temperatures of given positions (in horizontal axis) in Fig. 4.11 are for the linear TEG and π-shaped TEG, respectively. The horizontal axis indicates the locations of recording temperature, defined in Fig. 4.3 (b). In addition, the thermal resistor network model of 1-D heat flow was built as shown in Fig. 4.3 (c) which is corresponding to Fig. 4.3 (b). The details of how to calculate the temperatures at nodes defined in Fig. 4.3 (b) are described in Chapter 3. ΔT_n by experiment, the thermal resistor model and ANSYS are $455\,^{\circ}C$, $475\,^{\circ}C$ and $478\,^{\circ}C$, and ΔT_p are $465\,^{\circ}C$, $479\,^{\circ}C$ and $483\,^{\circ}C$,

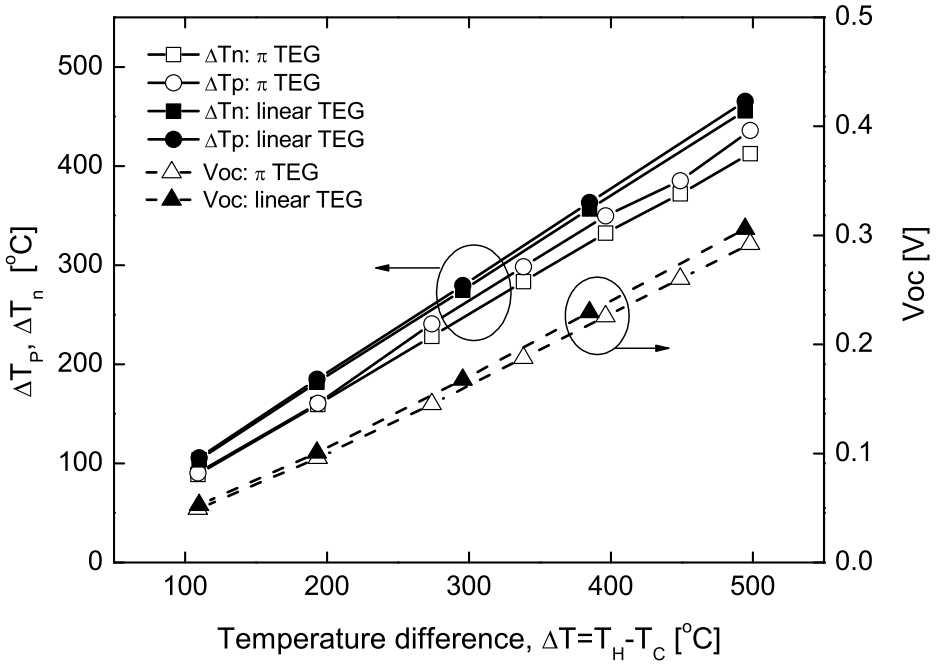

Figure 4.10: Comparison of the linear TEG with π-shaped TEG: Temperature difference generated through only TE legs and V_{oc} as a function of ΔTs

respectively. These measured values and the predictions by FEM and the thermal resistor network model are in good agreement within 5% in ΔT_n and within 4% in ΔT_p.

The temperature drops of the linear TE module from the dovetailed AlN to TE legs on both high and low temperature ends are smaller than those of the π TEG, which verifies that the thermal resistance through substrate layers in the linear TE design is smaller than that of the π TEG, resulting in the larger temperature gradient in the linear TEG. This larger temperature gradient in the linear TEG generates larger electric potential, as shown by the dotted line in Fig. 4.10, which produces more output power generation, as shown in Fig. 4.14, where the $I-V$ and $I-P$ curves of the two different TEG designs under $\Delta T = 500\,^{\circ}C$ are given.

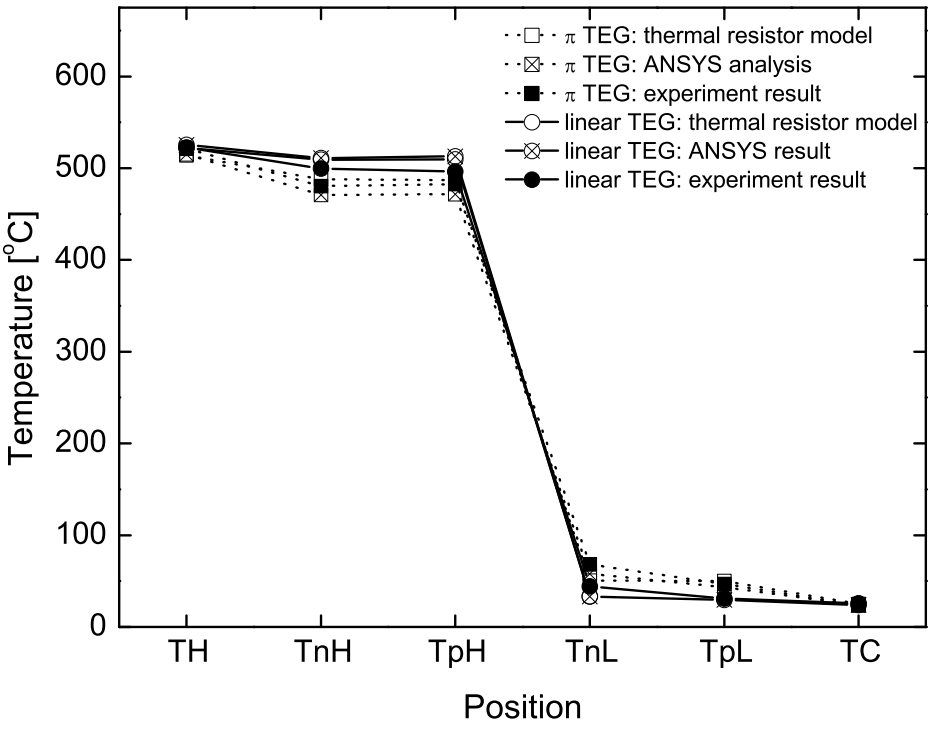

Figure 4.11: Comparison of the linear TEG with π-shaped TEG: Temperature profile of experiment data, predictions by ANSYS analysis and the thermal resistor network model

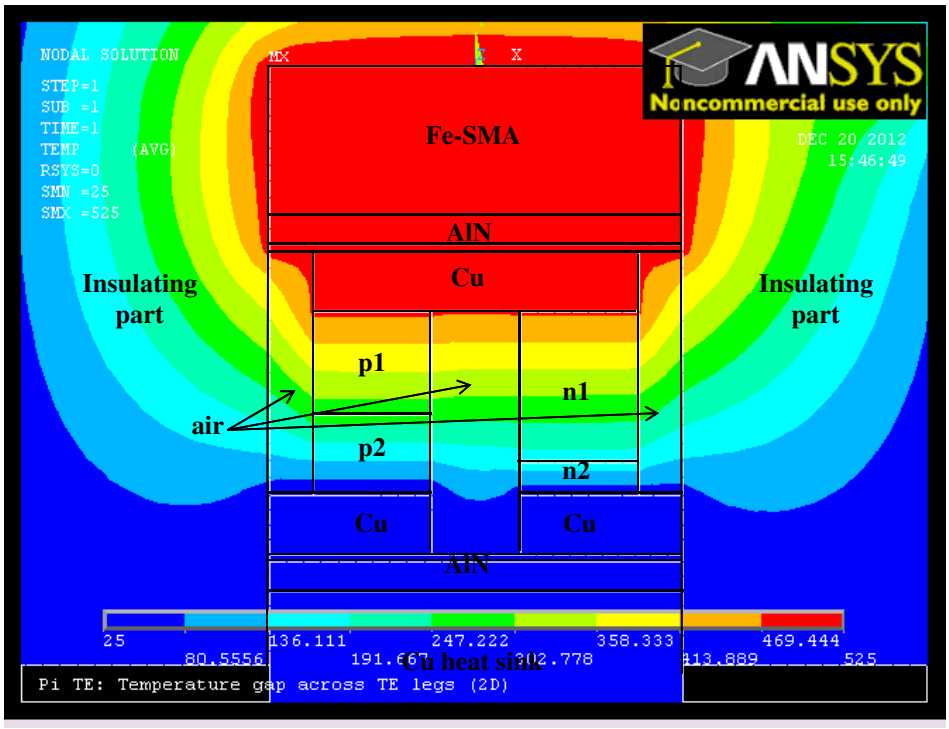

Figure 4.12: The FEA results of temperature distributions for π-shaped TEG design

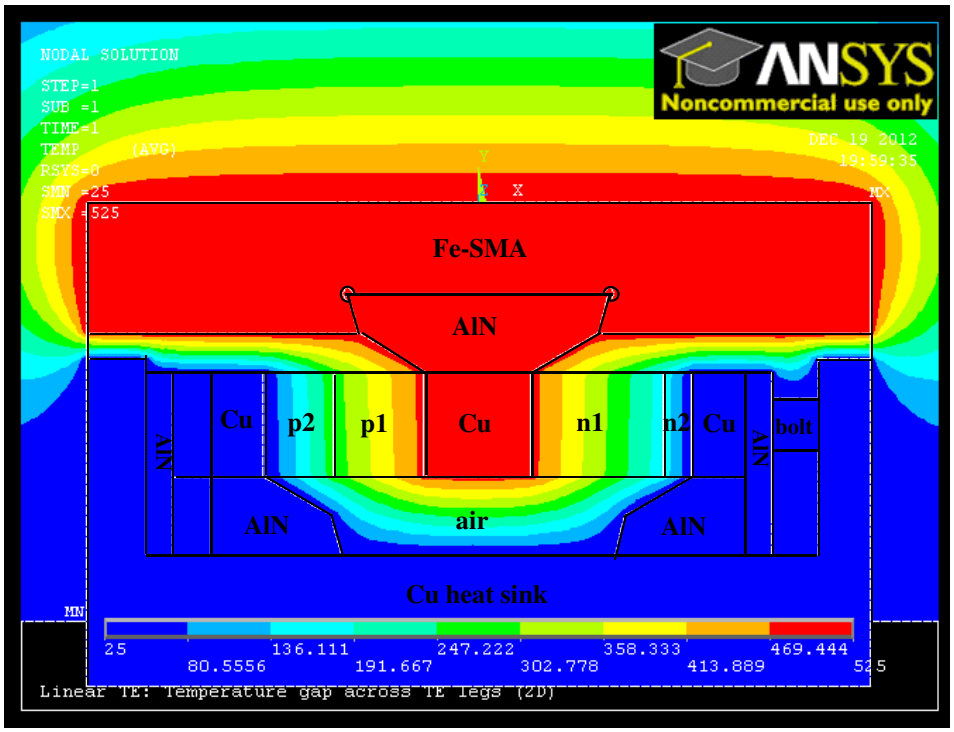

Figure 4.13: The FEA results of temperature distributions for the linear TEG with integration using shrink-fit method

The maximum output power of the linear TEG design is higher by 7% more than that of the π TEG since the larger electric potential is generated in the former. Fig. 4.15 shows the generated output power and the specific power density as a function of ΔT, where the specific power density is defined as a power generation per a unit weight, *i.e.*, in unit of $[W/kg]$. The dotted and solid lines show the calculated maximum out power and specific power density, respectively, and the solid and hollow markers are the experimental data of linear and π-shaped TEG, respectively. The advantage of the linear design in this study is to reduce the total weight of the TEG since the use of AlN plates and metal electrodes in the π-shaped TEG design is replaced by Cu-AlN T-shaped electrode. The specific power density of the linear TEG design is improved by 108% as compared with that of the π TEG as the weight of the linear TEG is 5.75 $[g]$ while that of π-shaped TEG is 11.19 $[g]$ where the both designs exclude the weight of the combustion chamber wall (Fe-SMA plate). The lighter weight is a critical issue in weight-sensitive applications such as UAV, so the linear TE structure is a promising design improving of power generation while ensuring stronger bonding between the linear TEG and the walls of a combustion chamber of an engine.

Let us now turn to the thermomechanical stress issue associated with the integrated linear TEG into the walls of combustion chamber made of Fe-SMA. To this end, we made FEM analysis by using four different 2D geometries of TEG, (a) π TEG interfaced with planar AlN and Fe-SMA plates, (b) linear TEG with AlN and T-shaped Cu electrode interfaced with planar Fe-SMA plate, (c) linear TEG with dovetail-shaped AlN-Cu composite electrode, interfaced with planar Fe-SMA plate and (d) the present linear TEG with dovetailed-shaped AlN-Cu composite electrode interfaced with grooved Fe-SMA shrink-fit bonding. The FEM results of these are shown in Fig. 4.16, 4.17, 4.18 and 4.19, respectively. The common conditions used for the FEM analysis were as follows: (1) element type: plane223, (2) mesh size: 0.25 mm square, (3) temperature boundary conditions: $T_H = 525\,^{\circ}C$ and $T_C = 25\,^{\circ}C$ for $\Delta T = 500\,^{\circ}C$, and (4) adiabatic environment to ensure complete 1-D heat flow. The compression of 0.7 MPa in horizontal direction was applied to linear TEG to minimize contact resistances thermally and electrically, which is generated by bolt-jointing, see Fig. 4.3 (b).

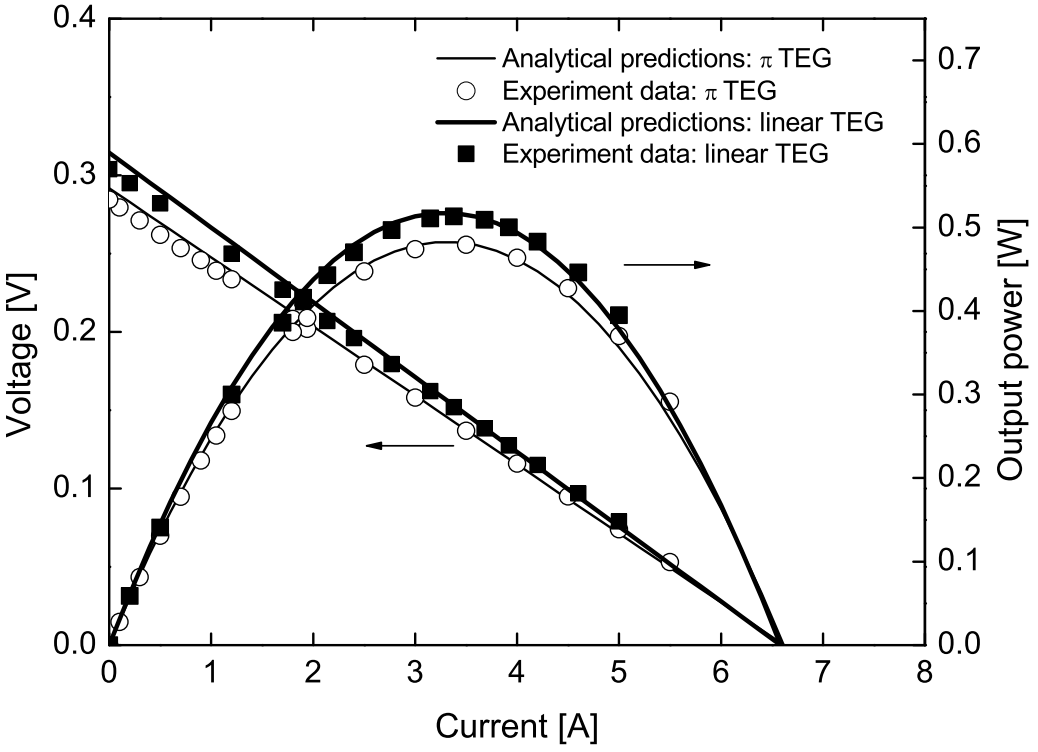

Figure 4.14: Comparison of the linear TEG with π-shaped TEG: $I - V$ curve and output power

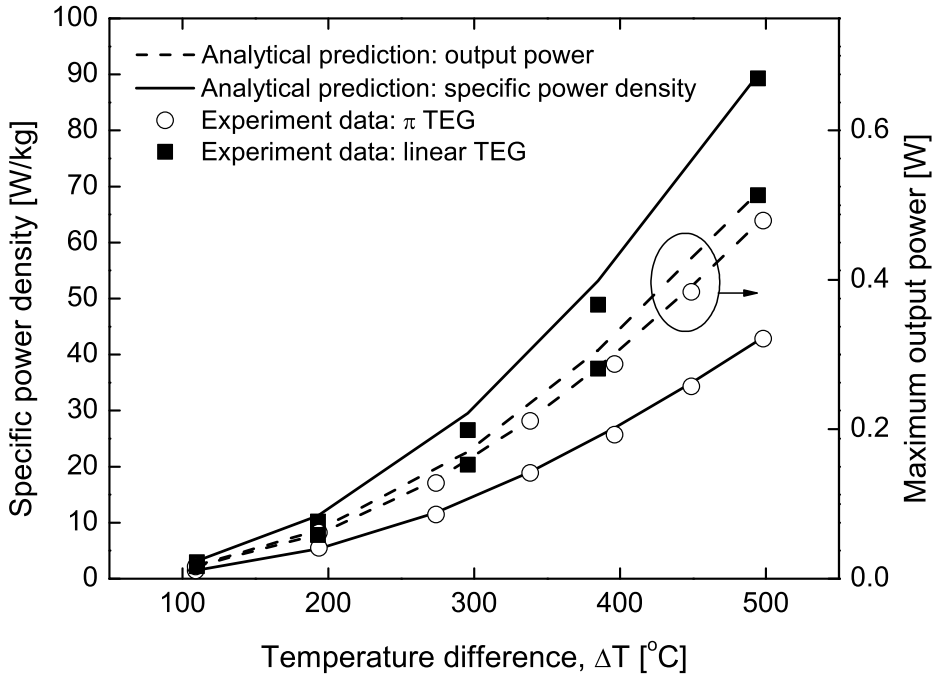

Figure 4.15: Comparison of the linear TEG with π-shaped TEG: The maximum output power and the specific power density as a function of ΔTs

In Fig. 4.16, the maximum shear stress of the segmented π-shaped TEG is 759 MPa at the interface between AlN plate and Cu electrodes mainly due to a mismatch of coefficient of thermal expansion (CTE). Fig. 4.17 shows shear stress distribution in linear TEG design using bulk T-shape Cu electrode, where the maximum shear stress occurred at AlN-Cu interface, which is 1.35 GPa. This indicates the linear TEG structure using solid T-shape electrode reported by Crane *et al.* [97] and Sakamoto *et al.* [96] is weaker design than the above π-shaped TEG design. Fig. 4.18 and 4.19 shows shear stresses of linear TEG using dovetailed AlN-Cu composite electrode without and with shrink-fitting integration method, respectively. The maximum shear stress of 439 MPa occurred at the interface of Fe-SMA and AlN part in the assembly without shrink-fitting shown in Fig. 4.18, which is much lower than that of the linear TEG using bulk Cu electrode in Fig. 4.17, and reduced by 42% compared with π-shaped TEG. The linear TEG by using shrink-fit method shown in Fig. 4.19 gives rise to the maximum shear stress of 402 MPa, which is reduced by 47% and 9% compared with the π-shaped TEG and the linear TEG without shrink-fitting, respectively. As the top corners of the groove in Fe-SMA plate is modified to be rounded to eliminate stress concentration on the sharp part of assembled AlN, the maximum shear stress in the linear TEG design with shrink-fit design is reduced to the smallest. On the other hand, the conventional linear structure using a solid T-shape electrode, Fig. 4.17 was weak under high temperature environment due to larger thermal stress induced. Therefore, the FEA results of Fig. 4.16 through 4.19, we can conclude that the linear TEG with dovetailed AN-Cu composite electrode built in the Fe-SMA based on shrink-fit bonding, is the best design among others.

In summary, new TEG design is proposed, which is based on dovetail shaped AIN-Cu electrode built in the Fe-SMA plate by using shrink-fit bonding. This design gives rise to the best performance in terms of highest specific power density, while it is more robust and durable. The power output of the this linear TEG is 7% higher than that of the π-shaped TEG. The specific power density of the linear TEG is dramatically increased from that of the π TEG, *i.e.*, from 42.9 $[W/kg]$ to 89.3 $[W/kg]$ thank to lighter weight of the

TEG design	Max. shear stress	Total weight	Max. temperature difference
(a)	759 [MPa]	5.6 $[g]$	446.9 $[^{\circ}C]$
(b)	1.3 [GPa]	4.7 $[g]$	439.3 $[^{\circ}C]$
(c)	439 [MPa]	2.9 $[g]$	423.3 $[^{\circ}C]$
(d)	402 [MPa]	2.9 $[g]$	458.9 $[^{\circ}C]$

Table 4.1: Comparison of various TEG designs: maximum shear stress, total weight of 1-pair assembly, and maximum temperature difference across TE materials

linear TEG, and the maximum shear stress of the linear TEG is reduced by 47% compared with the conventional π-shaped TEG. Table 4.1 summarizes each TEG design, (a) $\sim$ (d) as shown in Fig. 4.16 $\sim$ Fig. 4.19. The total weight of the design (b) is estimated based on the measured value of design (c) and (d) by replacing top AlN part with Cu block, where the weight of Fe-SMA is excluded. The design (a) generates the second largest temperature difference which is larger than that of the design (b) due to the thermal resistance of bulk T-shaped Cu electrode is higher than that of Cu planar electrode in the design (a). The design (c) has the lowest temperature gap because the thermal conductivity of the top AlN part is lower than that of Cu in the design (b). The design (d) of the lightest weight has the minimum shear stress and the largest temperature gap among others due to the shrink-fit joining method.

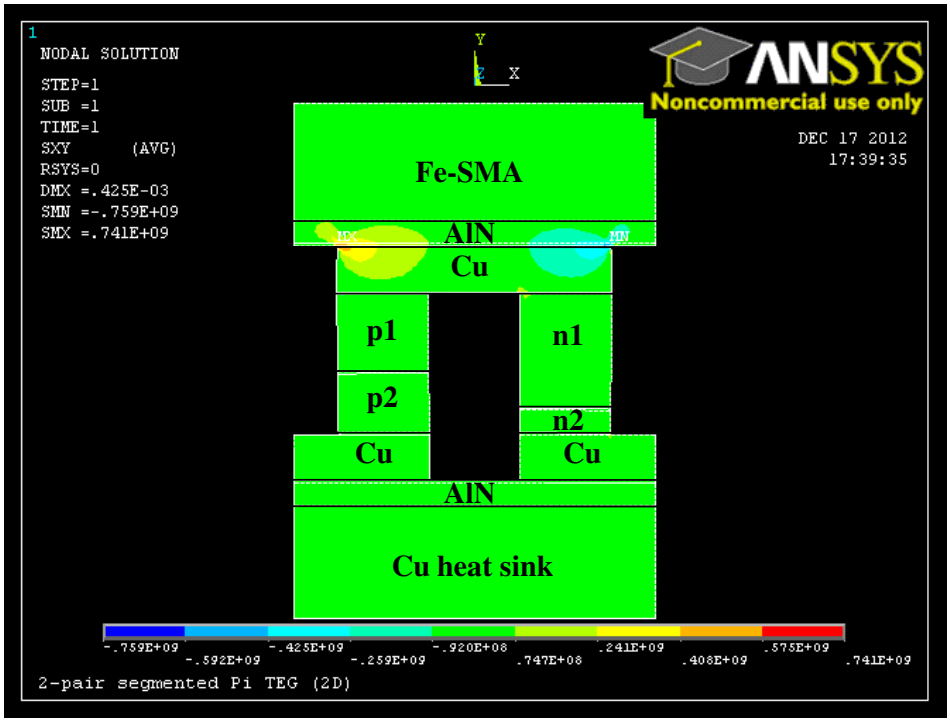

Figure 4.16: The results of finite element analysis by ANSYS: segmented π-shape TEG, design (a)

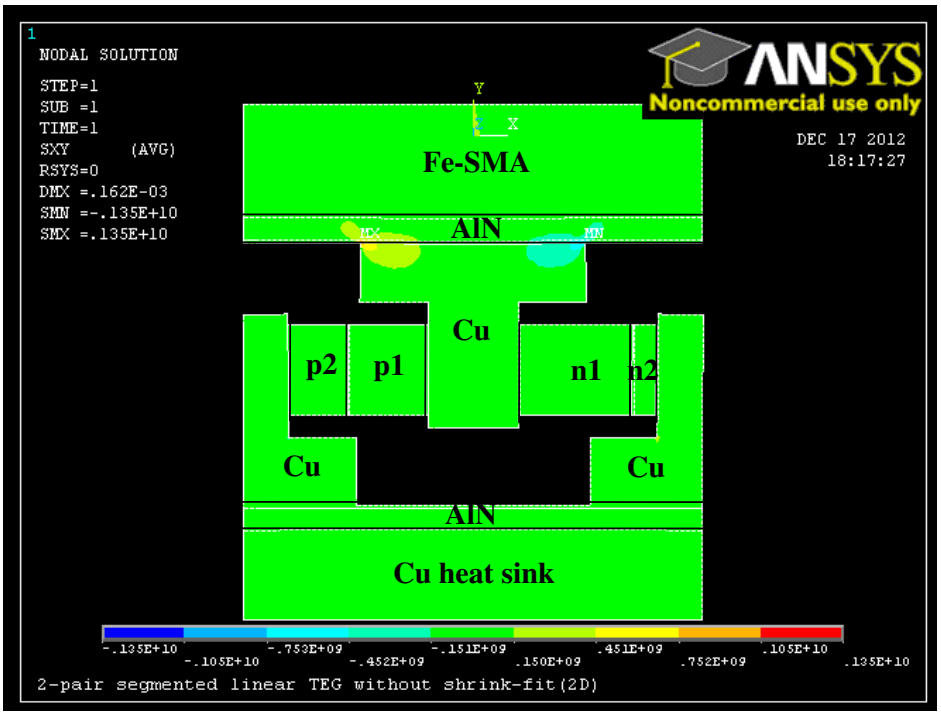

Figure 4.17: The results of finite element analysis by ANSYS: segmented linear TEG using T-shaped Cu electrodes, design (b)

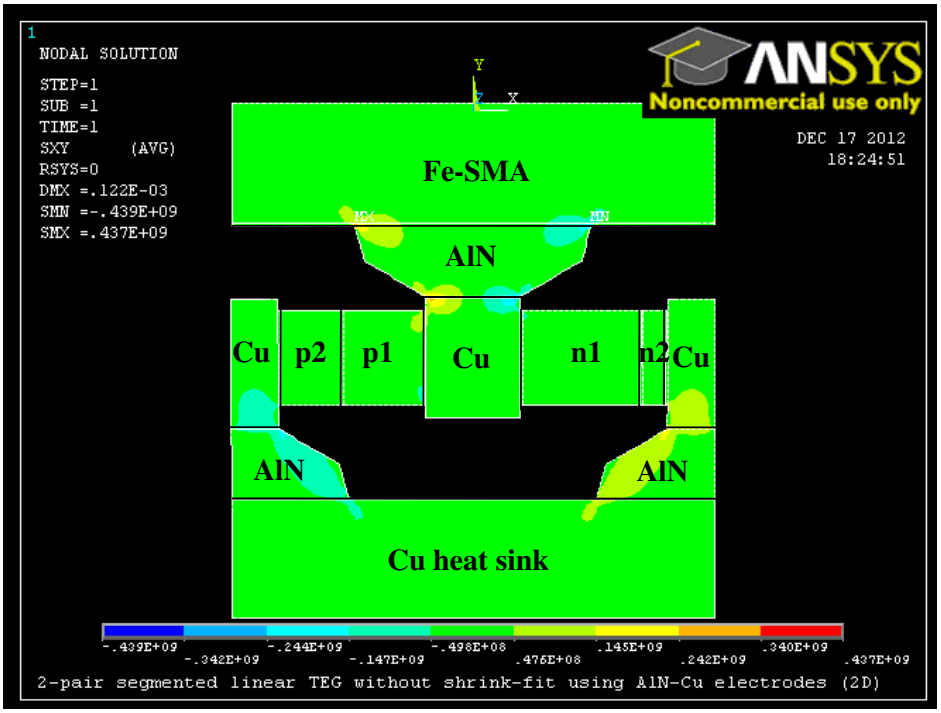

Figure 4.18: The results of finite element analysis by ANSYS: segmented linear TEG with dovetail-shaped electrodes using AlN-Cu composite interfaced with planar Fe-SMA plate, design (c)

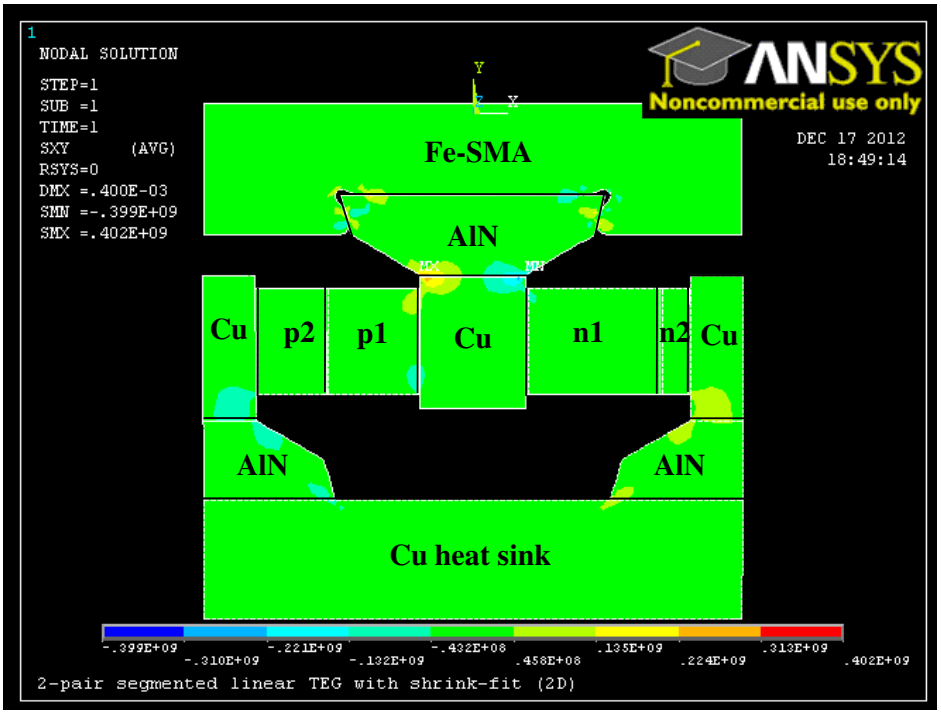

Figure 4.19: The results of finite element analysis by ANSYS: segmented linear TEG with dovetail-shaped AlN-Cu composite electrode using shrink-fitting integration to the grooved Fe-SMA plate, design (d)

Chapter 5

CONCLUSION

The goal of this research is to design a segmented TEG generating higher specific output power, and develop self-integration method into a combustion system in weight-sensitive applications such as aero and ground vehicles. To this end, light-weight TE materials and new design of electrodes are essential. Mg_2Si for n-type and HMS for p-type are the most promising TE compounds for this purpose since both alloys are low mass density compared with other candidates working at intermediate temperature around $500\,^{\circ}C$. The forming of nanostructures is a key issue to improve ZT value by reducing thermal conductivity of lattice component since other properties are not easy to control independently due to their interrelationship each other. Nano-sized grain structures enables κ_{ph} to be decreased independently resulting from intensive phonon scattering, and it was constructed via high energy MA for alloyed nano particles and SPS for rapid sintering processing to minimize grain growth during solidification. This combination of MA and SPS technique is simple and effective method to synthesize bulk TE materials with nanostructues. Based on this advanced metallurgical process, this study investigated a new secondary doping element, Indium on Bi doped Mg_2Si alloy, and the ZT value of Bi-In doped n-type Mg_2Si was improved by more than 50% as compared with Bi doped Mg_2Si alloy.

The two-pair π shaped TEG was fabricated based on two segments in each n-type and p-type column, where n-type Mg_2Si and p-type HMS were utilized as TE segments for high temperature side, and Bi-Te alloys were served as low temperature parts. It is important to examine electrical contact resistance at all bonding interfaces in TEG assembly because those interfaces of two dissimilar materials influence the electrical resistance of TEG module and output power generation becomes poor with higher contact resistances. The output power generation was measured under $\Delta T = 500\,^{\circ}C$ and experimental results were

compared with analytical predictions, which have a good agreement within 2% difference.

The advanced linear-shaped TEG design is proposed for self-integration process into combustion chamber's wall using the shape memorizing of Fe-SMA. To this end, the composite electrode consisting of tapered AlN part and Cu block was processed, which enables AlN to fit into Fe-SMA for shrink-fit joining. In the proposed TEG of linear structure in this study, each metal electrode and ceramic substrate of conventional π shaped TEG were combined to one T-shape electrode composed of AlN and Cu, which conducts heat effectively. Thus, larger temperature gaps across TE segments were generated and output power was increased by 7% compared to π shaped TEG. It also lightens the total weight of the device dramatically, so the specific power density, $[W/kg]$, was increased by a factor of more than two. The thermal resistor network model and ANSYS analysis were demonstrated for the verification between measured temperature values and predictions. The net temperature gap (ΔT_n and ΔT_p) are in a good agreement each other within 5% difference. The AlN-Cu electrode and shrink-fitting scheme enabled the proposed TEG design to overcome the structural weakness. The structural stability at high temperature environment was investigated via FEM analysis using ANSYS. Thus, the TEG design in this study reduced the maximum thermal shear stress by 46% compared to π-shaped TEG and by 70% of conventional linear-shaped TEG.

REFERENCES

[1] T. J. Seebeck. Ueber die magnetische polarisation der metalle und erze durch temperatur-differenz. *Annalen der Physik*, 82(2):133–160, 1826.

[2] M Peltier. Investigation of the heat developed by electric currents in homogeneous materials and at the junction of two different conductors. *Ann. Chim. Phys*, 56:371, 1834.

[3] S. W. Angrist. *Direct Energy Conversion*. Allyn and Bacon, Boston, 1965.

[4] M. V. Vedernikov, E. K. Iordanishvili, and A. F. Ioffe. Origin of modern semiconductor thermoelectric energy conversion. *17th Int. Conf. on Thermoelectrics*, 1:37–42, 1998.

[5] H. J. Goldsmid and R. W. Douglas. The use of semiconductors in thermoelectric refrigeration. *British J. Appl. Phys*, 5:386–390, 1954.

[6] H. J. Goldsmid. Heat conduction in bismuth telluride. *Proc. Phys. Soc.*, 72:17–26, 1958.

[7] G. A. Slack. *CRC Handbook of Thermoelectrics*. CRC Press, Boca Raton, 1995.

[8] G. L. Bennett. *CRC Handbook of Thermoelectrics: Space application*. CRC Press, Boca Raton, 1995.

[9] D.M. Rowe, editor. *Thermoelectrics Handbook: Macro to Nano*. CRC Taylor & Francis, 2006.

[10] H. J. Goldsmid. *Thermoelectric Refrigeration*. Plenum Press, New York, 1964.

[11] D. D. Pollock. *Thermocouples: Theory and Properties*. CRC Press, Boca Raton, FL, 1991.

[12] B. Wolfing, C. Kloc, J. Teubner, and E. Bucher. High performance thermoelectric Tl_9BiTe_6 with an extremely low thermal conductivity. *Phys. Rev. Lett.*, 86:4350, 2001.

[13] V. L. Kuznetsov, L. A. Kuznestsova, A. E. Kaliazin, and D. M. Rowe. Preparation and thermoelectric properties of $A_8^{II}B_{16}^{III}B_{30}^{IV}$ clathrate compounds. *J. Appl. Phys.*, 87:7871, 2000.

[14] J. Androulaskis, C. H. Lin, H. J. Kong, C. Uher, C. Wu, T. Hogan, B. A. Cook, T. Caillat, K. M. Paraskevopoulos, and M. Kanatzidis. Spinodal decomposition and nucleation and growth as a means to bulk nanostructured thermoelectrics: Enhanced performance in $Pb_{1-x}Sn_xTe$-PbS. *J. Am. Chen. Soc.*, 129:9780, 2007.

[15] D. Y. Chung, T. Hogan, P. Brazis, M. Rocci-Lane, C. Kannewurf, M. Bastea, C. Uher, and M. G. Kanatzidis. $CsBi_4Te_6$: A high-performance thermoelectric material for low-temperature applications. *Science*, 287:1024, 2000.

[16] K. F. Hsu, S. Loo, F. Guo, W. Chen, J. S. Dyck, C. Uher, T. Hogan, E. K. Polychroniadis, and M.G.Kanatzidis. Cubic $AgPb_mSbTe_{2+m}$: Bulk thermoelectric materials with high figure of merit. *Science*, 303:818, 2004.

[17] J. S. Rhyee, K. H. Lee, S. M. Lee, E. Cho, S. I. Kim, E. Lee, Y. S. Kwon, J. H. Shim, and G. Kotliar. Peierls distortion as a route to high thermoelectric performance in $In_4Se_{3-\delta}$ crystals. *Nature*, 459:965, 2009.

[18] B. Yu, Q. Zhang, H. Wang, X. Wang, H. Wang, D. Wang, H. Wang, G. J. Snyder, G. Chen, and Z. F. Ren. Thermoelectric property studies on thallium-doped lead telluride prepared by ball milling and hot pressing. *J. Appl. Phys.*, 108:016104, 2010.

[19] J. S. Rhyee, K. Ahn, K. H. Lee, H. S. Ji, and J. Shim. Enhancement of the thermoelectric figure-of-merit in a wide temperature range in $In_4Se_{3-x}Cl_{0.03}$ bulk crystals. *Adv. Mater.*, 23:2191, 2011.

[20] W. S. Liu, Q. Zhang, Y. C. Lan, S. Chen, X. Yan, Q. Zhang, H. Wang, D. Z. Wang, G. Chen, and Z. F. Ren. Thermoelectric property studies on Cu-doped n-type $Cu_xBi_2Te_{2.7}Se_{0.3}$ nanocomposites. *Adv. Energy Mater.*, 1:577, 2011.

[21] K. Biswas, J. He, Q. Zhang, G. Wang, C. Uher, V. P. Dravid, and M. G. Kanatzidis. Strained endotaxial nanostructures with high thermoelectic figure-of-merit. *Nat. Chem.*, 3:160, 2011.

[22] X. Shi, J. Yang, J. R. Salvador, M. Chi, J. Y. Cho, H. Wang, S. Bai, J. Yang, W. Zhang, and L. Chen. Multiple-filled skutterudites: High themoelectric figure-of-merit through separately optimizing electrical and thermal transports. *J. Am. Chen. Soc.*, 133:7837, 2011.

[23] H. Liu, X. Shi, F. Xu, L. Zhang, W. Zhang, L. Chen, Q. Li, C. Uher, T. Day, and G. J. Snyder. Copper ion liquid-like thermoelectrics. *Nat. Mater.*, 11:422, 2012.

[24] J. Fan, H. Liu, X. Shi, S. Bai, X. Shi, and L. Chen. Investigation of thermoelectric properties of $Cu_2Ga_xSn_{1-x}Se_3$ diamond-like compounds by hot pressing and spark plasma sintering. *Acta Mater.*, 61:4297, 2013.

[25] R. Rogl, A. Grytsiv, E. Royanian, P. Heinrich, E. Bauer, P. Rogl, M. Zehetbauer, S. Puchegger, M. Reinecker, and W. Schranz. New p- and n-type skutterudites with ZT>1 and nearly identical thermal expansion and mechanical properties. *Acta Mater.*, 61:4066, 2013.

[26] L. D. Hicks and M. S. Dresselhaus. Effect of quantum-well structure on the thermoelectric figure of merit. *Phys. Rev. B*, 47:12727, 1993.

[27] L. D. Hicks and M. S. Dresselhaus. Thermoelectric figure of merit of a one-dimensional conductor. *Phys. Rev. B*, 47:16631, 1993.

[28] M. S. Dresselhaus, G. Chen, M. Y. Yang, R. G. Yang, H. Lee, D. Z. Wang, Z. F. Ren, J. P. Fleurial, and P. Gogna. New direction for low dimensional thermoelectric material. *Adv. Mater.*, 19:1043, 2007.

[29] B. Poudel, Q. Hao, Y. Hao, Y. Ma, Y.C. Lan, A. Minnich, B. Yu, X. Yan, D.Z. Wang, A. Muto, D. Vashaee, X.Y. Chen, J.M. Liu, M.S. Dresselhaus, G. Chen, and Z.F. Ren. High-thermoelectric performance of nanostructured bismuth antimony telluride bulk alloys. *Science*, 320:634, 2008.

[30] X. W. Wang, H. Lee, Y.C. Lan, G. H. Zhu, G. Joshi, D. Z. Wang, J. Yang, A. J. Muto, M. Y. Tang, J. Klastdky, S. Song, M. S. Dresselhaus, G. Chen, and Z. F. Ren. Enhanced thermoelectric figure of merit in a nanostructured n-type silicon germanium bulk alloy. *Appl. Phys. Lett.*, 93:193121, 2008.

[31] G. Joshi, H. Lee, Y. C. Lan, X. W. Wang, G. H. Zhu, D. Z. Wang, R. W. Gould, D. C. Cuff, M. Y. Tang, M. S. Dresselhaus, G. Chen, and Z. F. Ren. Enhanced thermoelectric figure-of-merit in nanostructured p-type silicon germanium bulk alloys. *Nano Lett.*, 8:4670, 2008.

[32] R. Venkatasubramanian, E. Siivola, T. Colpitts, and B. OQuinn. Thin-film thermoelectric devices with high room-temperature figures of merit. *Nature*, 413:597, 2001.

[33] P. Vij and D. Hardej. Evaluation of tellurium toxicity in transformed and non-transformed human colon cells. *Environ. Toxicol. Phar.*, 34:768, 2012.

[34] G. J. Snyder and E. S. Toberer. Complex thermoelectric materials. *Nature*, 7(105), 2008.

[35] L. D. Zhao, B. P. Zhang, J.F. Li, H.L. Zhang, and W.S. Liu. Enhaced thermoelectric and mechanical properties in textured n-type Bi_2Te_3 prepared by spark plasma sintering. *Solid State Science*, 10:651, 2008.

[36] T. Caillat, J. P. Fleurial, and A. Borshchevsky. Preparation and thermoelectric properties of semiconducting Zn_4Sb_3. *J. Phys. Chem Solids*, 58:1119, 1997.

[37] T. Itoh and M. Yamada. Synthesis of thermoelectric manganese silicide by mechanical alloying and pulse discharge sintering. *J. Electron. Mater.*, 38:925, 2009.

[38] W. S. Liu, B. P. Zhang, J. F. Li, H. L. Zhang, and L. D. Zhang. Enhaced thermoelectric properties in $CoSb_{3-x}Te_x$ alloys prepared by mechanical alloying and spark plasma sintering. *J. Appl. Phys.*, 102:103717, 2007.

[39] M Fukano, T. Iida, K. Makino, M. Akasaka, Y. Oguni, and Y. Takanashi. Crystal growth of Mg_2Si by the Vertical Bridgman method and the doping effect of Bi and Al on thermoelectric characteristics. *Mater. Res. Soc. Symp. Proc.*, 1044:1044–U06–13, 2008.

[40] A. A. Yaroshevsky. Abundances of chemical elements in the earth's crust. *Geochemistry International*, 44:48, 2006.

[41] K. W. Mlynarski. *Survey methods for nonfuel minerals: U.S. Geological Survey Minerals Yearbook*, volume 1:1.4. 1998.

[42] M.S. El-Genk, H. H. Saber, J. Sakamoto, and T. Caillat. Life tests of a skutterudites thermoelectric unicouple (MAR-03). 21 Aug. 2003.

[43] T. Harman. Multiple stage thermoelectric generator of power. *J. Appl. Phys.*, 29:1471, 1958.

[44] J. Schilz, L. Helmers, Y. S. Yang, Y. Noda, and M. Niino. Bismuth Telluride/Iron Disilicide segmented thermoelectric elements: Patterning, preparation and properties. In *Proceedings of ICT97*, number 97TH8291, page 375, Dresden, Germany, August 26-29 1997.

[45] Y. S. Yang, M. Niino, A. Nishsida, and J. Yoshino. Development and evaluation of 3-Stage segmented thermoelectric elements. In *Proceedings of ICT98*, number 98TH8365, page 429, Nagoya, Japan, May 24-28 1998.

[46] R.R. Heikes and R. W. Ure. *Thermoelectricity: Scinece and Engineering*, chapter 17. Interscience Publishers,. Inc., New York, 1961.

[47] J. G. Stockholm. *CRC Handbook of Thermoelectric*, chapter 53. CRC Press, Boca Raton, 1995.

[48] J. Schilz, M. Riffel, K. Pixius, and H. J. Meyer. Synthesis of thermoelectric materials by mechnical alloying in planetary ball mills. *Powder Technology*, 105:149, 1999.

[49] J.Yang, X. Fan, R. Chen, W. Zhu, S. Bao, and X. Duan. Consolidation and thermoelectric properties of n-type bismuth telluride based materials by mechanical alloying and hot pressing. *J. Alloy. Compd.*, 416:270, 2006.

[50] J. Yang, Q. Hao, H. Wang, Y. C. Lan, Q. Y. He, D. Z. Wang, J. A. Harriman, V. M. Varki, M. S. Dresselhaus, G. Chen, and Z. F. Ren. Solubility study of Yb in n-type skutterudites $Yb_xCo_4Sb_{12}$ and their enhanced thermoelectric properties. *Phys. Rev. B*, 80:115329, 2009.

[51] S. C. Ur, J. C. Kwon, and I. H. Kim. Thermoelectric properties of Fe-doped $CoSb_3$ prepared by mechanical alloying and vacuum hot pressing. *J. Alloy. Compd.*, 442:358, 2007.

[52] J.Cui, X. Liu, W. Yang, D. Chen, H. Fu, and P. Ying. Thermoelectric properties in nanostructured homologous series alloys $Ga_mSb_nTe_{1.5}$. *J. Appl. Phys.*, 105:063703, 2009.

[53] H. Wang, J. F. Li, C. W. Nan, M. Zhou, W. S. Liu, and B. P. Zhang. High-performance $Ag_{0.8}Pb_{18+x}SbTe_{20}$ thermoelectric bulk materials fabricated by mechanical alloying and spark plasma sintering. *Appl. Phys. Lett.*, 88:092104, 2006.

[54] M. Akasaka, T. Iida, A. Matsumoto, K. Yamanaka, Y. Takanashi, T. Imai, and N. Hamada. The thermoelectric properties of bulk crystalline n- and p-type Mg_2Si prepared by the vertical Bridgman method. *J. Appl. Phys.*, 104:013703, 2008.

[55] M. Yoshinaga, T. Iida, M. Noda, T. Endo, and Y. Takanashi. Bulk crystal growth of Mg_2Si by the vertical bridgman method. *Thin Solid Film*, 461:86, 2004.

[56] Y. Isoda, T. Nagai, H. Fujiu, Y. Imai, and Y. Shinohara. The effect of Bi doping thermoelectric properties of $Mg_2Si_{0.5}Sn_{0.5}$. In *26^{th} International Conference on Thermoelectrics*, page 251, 2007.

[57] Q. Zhang, J. He, J. Zhu, S. N. Zhang, X. B. Zhao, and T. M. Tritt. High figures of merit and natural nanostructures in $Mg_2Si_{0.4}Sn_{0.6}$ based thermoelectric materials. *Appl. Phys. Lett.*, 93:102109, 2008.

[58] Q. Zhang, J. He, X. B. Zhao, S. N. Zhang, T. J. Zhu, H. Yin, and T. M. Tritt. In situ synthesis and thermoelectric properties of La-doped Mg_2(Si,Sn) composites. *J. Phys. D: Appl. Phys.*, 41:185103, 2008.

[59] J. Tani and H. Kido. Thermoelectric properties of Bi-doped Mg_2Si semiconductors. *Phys. B.*, 364:218, 2005.

[60] J. Tani and H. Kido. Thermoelectric properties of Al-doped $Mg_2Si_{1-x}Sn_x$. *J. Alloy. Comp.*, 464:335, 2008.

[61] Y. Chen, C. P. Li, H. Chen, and Y. Chen. One-dimensional nanomaterials synthesized using high-energy ball milling and annealing process. *Sci. Tech. Adv. Mater.*, 7:839, 2006.

[62] C. Suryanarayana. Mechanical alloying and milling. *Prog. Mater. Sci.*, 46:1, 2001.

[63] M. Tokita. Mechanism of spark plasma sintering. Brochure of Sumitomo Coal Mine Co. Ltd.

[64] J. Tani and H. Kido. Thermoelectric properties of Sb-doped Mg_2Si semiconductors. *Intermetallics*, 15:1202, 2007.

[65] C. Kittel. *Introducton to Solid State Physics*. Number ch. 6:p150. Wiley, 8th edition, 2005.

[66] M. Zhang, W. Z. Zhang, and G. Z. Zhu. The morphology and crystallography of polygonal Mg_2Sn precipitates in a Mg-Sn-Mn-Si alloy. *Scripta Materialia*, 59:866, 2008.

[67] D. M. Rowe. Thermoelectric power generation. *Proc. Inst. Electr. Eng.*, 125:1113, 1978.

[68] L. E. Bell. Cooling, heating, generating power, and recovering waste heat with thermoelectric systems. *Science*, 321:1457, 2008.

[69] W. C. Hall. *CRC Handbook of Thermoelectrics*, chapter 40. CRC Press, Boca Raton, FL, 1995.

[70] M.A. Karri, E.F. Thacher, and B.T. Helenbrook. Exhaust energy conversion by thermoelectric generator: Two case studies. *Energy Convers. Manage.*, 52:1596, 2011.

[71] K. Saqr, M. Mansour, and M. Musa. Thermal design of automobile exhaust based thermoelectric generators: Objectives and challenges. *Int J Automot Technol*, 92:155, 2008.

[72] J. Fleming, W. Ng, and S. Ghamaty. Thermoelectric-based power system for UAV/MAV applications. pages AIAA2002–3412, Portsmouth, VA, 2002. Unmanned Aerospace Vehicles, Systems, Technologies, and Operations Conference and Workshop.

[73] W. R. Pogue, N. J. Baucom, J. P. Thomas, and M. A. Qidwai. Structure-power system for unmanned air vehicles. Baltimore, MD, 2005.

[74] C. Yu and K.T. Chau. Thermoelectric automotive waste heat energy recovery using maximum power point tracking. *Energy Convers Manage.*, 50:1506, 2009.

[75] D. Crane, D. Kossakovski, and L. Bell. Modeling the building blocks of a 10% efficient segmented thermoelectric power generator. *J. Electron. Mater.*, 38:1382, 2009.

[76] J. D'Angelo, E. Case, N. Matchanov, C. I. Wu, T. Hogan, J. Barnard, C. Cauchy, T. Hendricks, and M. Kanatzidis. Electrical, thermal, and mechanical characterization of novel segmented-leg thermoelectric modules. *J. Electron. Mater.*, 40:2051, 2011.

[77] M. S. El-Genk, H. H. Saber, T. Caillat, and J. Sakamoto. Tests results and performance comparisons of coated and un-coated skutterudite based segmented unicouples. *Energy Convers. Manage.*, 47:174, 2006.

[78] S. M. Choi, K. H. Lee, C. H. Lim, and W. S. Seo. Oxide-based thermoelectric power generation module using p-type $Ca_3Co_4O_9$ and n-type $(ZnO)_7In_2O_3$ legs. *Energy. Convers. Manage.*, 52:335, 2011.

[79] H. S. Kim, M. S. Choi, K. Kikuchi, and M. Taya. Optimization of thermoelectric modules based on mg-si system. *Proc. of SPIE*, 7288:72881W2, 2009.

[80] V. K. Zaitsev, M. I. Fedorov, E. A. Gurieva, I. S. Eremin, P. P. Konstantinov, A. Yu. Samunin, and M. V. Vedernikov. Highly effective $Mg_2Si_{1-x}Sn_x$ thermoelectrics. *Phys. Rev. B*, 74:045207, 2006.

[81] J. Y. Jung and I. H. Kim. Synthesis and thermoelectric properties of n-type Mg_2Si. *Elec. Mat. Lett.*, 6:187, 2010.

[82] M. Akasaka, T. Iida, K. Nemoto, J. Soga, J. Sato, K. Makino, M. Fukano, and Y. Takanashi. Non-wetting crystal growth of Mg_2Si by vertical Bridgman method and thermoelectric characterisitics. *J. Crystal Growth*, 304:196, 2007.

[83] D. Tamura, R. Nagai, K. Sugimoto, H. Udono, I. Kikuma, H. Tajima, and I. Ohsugi. Melt growth and characterization of Mg_2Si bulk crystals. *Thin Solid Film*, 515:8272, 2007.

[84] Q. Li, Z. Lin, and J. Zhou. Thermoelectric materials with potential high power factors for electricity generation. *J. Electron. Mater.*, 38:1268, 2009.

[85] E. Savary, F. Gascoin, and S. Marinel. Fast synthesis of nanocrystalline Mg_2Si by microwave heating: a new route to nano-structured thermoelectric materials. *Dalton Trans.*, 39:11074, 2010.

[86] E. Savary, F. Gascoin, S. Marinel, and R. Heuguet. Spark plasma sintering of fine Mg_2Si particles. *Powder Tech.*, 228:295, 2012.

[87] D. Berthebaud and F. Gascoin. Microwaved assisted fast synthesis of n and p-doped Mg_2Si. *J. Solid State Chem.*, 202:61, 2013.

[88] B. W. Swanson, E. V. Somers, and R. R. Heikes. Optimization of a sandwitched thermoelectric device. *Journal of Heat Transfer*, 83:77, 1961.

[89] M. S. El-Genk and H. H. Saber. High efficiency segmented thermoelectric unicouple for operation between 973 and 300 K. *Energy Convers Manage*, 44:1069, 2003.

[90] M. S. El-Genk and H. H. Saber. *Thermoelectrics Handbook: Macro to Nano*, chapter Modeling and optimization of Segmented Thermoelectric Generators for Terrestrial and Space Applications. CRC Taylor & Francis, 2006.

[91] G. Min and D. M. Rowe. *CRC Handbook of thermoelectric*, chapter 38. CRC Press, Boca Raton, 1995.

[92] M. Taya. *Electronic composites*. Cambridge University Press, 2005.

[93] X. Tang, W. Xie, H. Li, W. Zhao, Q. Zhang, and M. Niino. Preparation and thermoelectric transport properties of high-performance p-type BiTe with layered nanostructure. *Appl. Phys. Lett.*, 90(012102), 2007.

[94] Y. Q. Cao, X. B. Zhao, T. J. Zhu, X. B. Zhang, and J. P. Tu. Syntheses and thermoelectric properties of BiTe/SbTe bulk nanocomposites with laminated nanostructure. *Appl. Phys. Lett.*, 92:143106, 2008.

[95] D. T. Crane, J. W. LaGrandeur, F. Harris, and L. E. Bell. Performance results of a high power density thermoelectric generator: Beyond the couple. In *Proceedings of the 27th International Conference on Thermoelectrics*, Corvallis, OR, August 2008.

[96] T. Sakamoto, T. Iida, Y. Taguchi, S. Kurosaki, Y. Hayatsu, K. Nishio, Y. Kogo, and Y. Takanashi. Examination of a thermally viable structure for an unconventional uni-leg Mg_2Si thermoelectric power generator. *J. Electron. Mater.*, 41:1429, 2012.

[97] D. T. Crane and L. E. Bell. Progress towards maximizing the performance of a thermoelectric power generator. In *Proceedings of the 25th International Conference on Thermoelectrics*, Vienna, Austria, August 2006.

[98] H. S. Kim, W. S. Liu, K. Kikuchi, and M. Taya. Thermoelectric properties of n-type magnesium silicide and numerical analysis of module device. In *Proc. of the 18th International Conference on Composite Materials*, Jeju Island, South Korea, August 2011.

[99] A. Sato, H. Kubo, and T. Maruyama. Mechanical properties of Fe-Mn-Si based SMA and the application. *Materials transactions*, 47(3):571, 2006.

[100] T. Nemoto, T. Iida, J. Sato, T. Sakamoto, T. Nakajima, and Y. Takanashi. Power generation characteristics of Mg_2Si uni-leg thermoelectric generator. *J. Electron. Mater.*, 41:1312, 2012.

Appendix A

LENGTH OF EACH TE SEGMENT

Fig. A.1 is a schematic drawing of p-type segmented element with given thermal conductivity properties of each segment to find the length of each TE block. Based on Fourier's law of 1-D heat conduction, input heat flux Q is,

$$Q = \kappa_{p_1} \frac{T_H - T_C}{L_{p_1}} = \kappa_{p_2} \frac{T_H - T_C}{L_{p_2}} \tag{A.1}$$

where T_{in_p} is the interface temperature of p_1 and p_2 TE materials, and κ_{p_1} and κ_{p_2} are thermal conductivity of HMS and Bi-Sb-Te, which are measured at the average temperature of T_H and T_{in_p}, and T_{in_p} and T_C, respectively. Total length (L) of combined leg is usually known initially,

$$L = L_{p_1} + L_{p_2} \tag{A.2}$$

From Eq. A.1, L_{p_2} can be expressed as:

$$L_{p_2} = \frac{\kappa_{p_2}(T_{in_p} - T_C)}{\kappa_{p_1}(T_H - T_{in_p})} L_{p_1} \tag{A.3}$$

By combining Eq. A.2 and A.3,

$$L_{p_1} = L - L_{p_2} = L - \frac{\kappa_{p_2}(T_{in_p} - T_C)}{\kappa_{p_1}(T_H - T_{in_p})} L_{p_1} \tag{A.4}$$

So, one may obtain the optimized length of each thermoelectric block shown below,

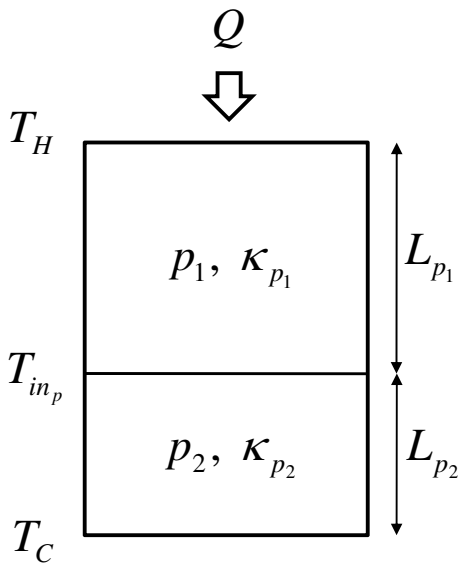

Figure A.1: Heat flow of p-type segmented leg combined with p_1 and p_2 TE materials

$$L_{p_1} = \frac{L}{1 + \dfrac{\kappa_{p_2}(T_{in_p} - T_C)}{\kappa_{p_1}(T_H - T_{in_p})}} \tag{A.5}$$

Then, from Eq. A.2, L_{p_2} can be found,

$$L_{p_2} = L - L_{p_1} = \frac{L}{1 + \dfrac{\kappa_{p_1}(T_H - T_{in_p})}{\kappa_{p_2}(T_{in_p} - T_C)}} \tag{A.6}$$

Similarly, the lengths of n-type column, the lengths can be calculated.

Appendix B

π-SHAPED TEG MODEL

As shown in Fig 3.10, the general segmented TEG model is described by expanding the work of Min *et al.* [91]. The numbers of n-type and p-type segments are N_n and N_p, respectively. It is also assembled by connecting N pairs electrically in series and thermally in parallel. The temperature difference ΔT , induced by the boundary temperature of hot side T_H, and cold side T_C, is given for the p-type leg,

$$\begin{aligned}
\Delta T &= T_H - T_C \\
&= \sum_{i=1}^{N_p} \Delta T_{p_i} + 2\Delta T_{sub} \\
&= \Delta T_p \left(\sum_{i=1}^{N_p} \frac{\Delta T_{p_i}}{\Delta T_p} + \frac{2\Delta T_{sub}}{\Delta T_p} \right) \\
&= \Delta T_p \left(\sum_{i=1}^{N_p} \frac{\kappa_p^E L_{p_i}}{\kappa_{p_i} L_p} + \frac{2\kappa_p^E L_{sub}}{\kappa_{sub} L_p} \right)
\end{aligned} \tag{B.1}$$

where we used continuity of heat flow,

$$\begin{aligned}
\kappa_{p_i} \frac{\Delta T_{p_i}}{L_{p_i}} &= \kappa_{p_i}^E \frac{\Delta T_p}{L_p} \\
L_p = \sum_{i=1}^{N_p} L_{p_i} &and\ \Delta T_p = \sum_{i=1}^{N_p} \Delta T_{p_i}
\end{aligned} \tag{B.2}$$

κ_p^E and κ_{p_i} are effective thermal conductivity of all combined p-type leg and thermal con-

ductivity of i^{th} segment respectively. L_p and L_n are total length of each combined leg and L_{p_i} and L_{n_i} are the length of each i^{th} segment. κ_{sub}, L_{sub} and ΔT_{sub} are the effective thermal conductivity, length, and temperature drop of the combined layer of ceramic substrate and metal electrode, respectively. ΔT_p and ΔT_{p_i} are the temperature difference through the combined p-type column and the temperature difference across i^{th} segment of p-type respectively. Therefore, the net temperature difference through the TE materials of p-type is obtained as,

$$\Delta T_p = \frac{T_H - T_C}{\sum_{i=1}^{N_p} \frac{\kappa_p^E L_{p_i}}{\kappa_{p_i} L_p} + \frac{2\kappa_p^E L_{sub}}{\kappa_{sub} L_p}} \tag{B.3}$$

Similarly for n-type,

$$\Delta T_n = \frac{T_H - T_C}{\sum_{i=1}^{N_n} \frac{\kappa_n^E L_{n_i}}{\kappa_{n_i} L_n} + \frac{2\kappa_n^E L_{sub}}{\kappa_{sub} L_n}} \tag{B.4}$$

where the subscript of p and n denotes p-type and n-type element. Open circuit voltage can be estimated by adding the voltage generated by p-type and n-type,

$$\begin{aligned} V_{OC} &= N(V_p + V_n) \\ &= N\left(\sum_{i=1}^{N_p} S_{p_i}(T_{p_i} - T_{p_{i+1}}) - \sum_{i=1}^{N_n} S_{n_i}(T_{n_i} - T_{n_{i+1}})\right) \\ &= N\left(\sum_{i=1}^{N_p} S_{p_i}\Delta T_{p_i} - \sum_{i=1}^{N_n} S_{n_i}\Delta T_{n_i}\right) \end{aligned}$$

where, S_{p_i} and S_{n_i} are the Seebeck coefficient of i^{th} segment of p-type and n-type, respectively. By defining and $\Delta T_{p_i} = T_{p_i} - T_{p_{i+1}}$, and $\Delta T_{n_i} = T_{n_i} - T_{n_{i+1}}$ using Eq. B.2,

$$V_{OC} = N\left(\sum_{i=1}^{N_p} S_{p_i}\frac{\kappa_p^E L_{p_i}}{\kappa_{p_i} L_p}\Delta T_p - \sum_{i=1}^{N_n} S_{n_i}\frac{\kappa_n^E L_{n_i}}{\kappa_{n_i} L_n}\Delta T_n\right) \tag{B.5}$$

By substituting Eq. B.3 and Eq. B.4 into Eq. B.5,

$$V_{OC} = N\left(\frac{\sum_{i=1}^{N_p} S_{p_i}\frac{\kappa_p^E L_{p_i}}{\kappa_{p_i} L_p}}{\sum_{i=1}^{N_p}\frac{\kappa_p^E L_{p_i}}{\kappa_{p_i} L_p} + \frac{2\kappa_p^E L_{sub}}{\kappa_{sub} L_p}} - \frac{\sum_{i=1}^{N_n} S_{n_i}\frac{\kappa_n^E L_{n_i}}{\kappa_{n_i} L_n}}{\sum_{i=1}^{N_n}\frac{\kappa_n^E L_{n_i}}{\kappa_{n_i} L_n} + \frac{2\kappa_n^E L_{sub}}{\kappa_{sub} L_n}}\right)(T_H - T_C) \tag{B.6}$$

To simplify Eq. B.6, the effective Seebeck coefficient is defined as:

$$S_p^M = \frac{\sum_{i=1}^{N_p} S_{p_i}\frac{\kappa_p^E L_{p_i}}{\kappa_{p_i} L_p}}{\sum_{i=1}^{N_p}\frac{\kappa_p^E L_{p_i}}{\kappa_{p_i} L_p} + \frac{2\kappa_p^E L_{sub}}{\kappa_{sub} L_p}}, S_n^M = \frac{\sum_{i=1}^{N_n} S_{n_i}\frac{\kappa_n^E L_{n_i}}{\kappa_{n_i} L_n}}{\sum_{i=1}^{N_n}\frac{\kappa_n^E L_{n_i}}{\kappa_{n_i} L_n} + \frac{2\kappa_n^E L_{sub}}{\kappa_{sub} L_n}} \tag{B.7}$$

Therefore, the open circuit voltage is finally reduced to:

$$V_{OC} = N(S_p^M - S_n^M)(T_H - T_C) \tag{B.8}$$

The total electrical resistance is calculated by summing the TE material's resistance, contact resistance, and lead wire's resistance.

$$
\begin{aligned}
R_{tot} &= R_{TE} + R_c + R_w \\
&= N\left[\frac{1}{A_p}\sum_{i=1}^{N_p}\rho_{p_i}L_{p_i} + \frac{1}{A_n}\sum_{i=1}^{N_n}\rho_{n_i}L_{n_i} + \frac{1}{A_p}\sum_{i=1}^{N_p+1}\rho_{pc_i} + \frac{1}{A_n}\sum_{i=1}^{N_n+1}\rho_{nc_i}\right] + R_w \\
&= N\left[\frac{1}{A_p}\left(\sum_{i=1}^{N_p}\rho_{p_i}L_{p_i} + \sum_{i=1}^{N_p+1}\rho_{pc_i}\right)\right. \\
&\qquad \left. + \frac{1}{A_n}\left(\sum_{i=1}^{N_n}\rho_{n_i}L_{n_i} + \sum_{i=1}^{N_n+1}\rho_{nc_i}\right)\right] + R_w
\end{aligned} \tag{B.9}
$$

ρ_{p_i}, ρ_{n_i}, ρ_{pc_i} and ρ_{nc_i} are electrical resistivity of p-type and n-type element and contact resistance between the i^{th} and $(i+1)^{th}$ of p-type and n-type elements, respectively. A_p and A_n are the cross sectional areas of each type segment. R_w is the electric resistance of lead wires measured experimentally. The current I is obtained by ohm's law.

$$
\begin{aligned}
I &= \frac{N(S_p^M - S_n^M)(T_H - T_C)}{R_{tot} + R_L} \\
&= \frac{N(S_p^M - S_n^M)(T_H - T_C)}{R_{tot}(1+m)} \\
&= \frac{N(S_p^M - S_n^M)(T_H - T_C)}{(1+m)\left[N\left\{\frac{1}{A_p}\left(\sum_{i=1}^{N_p}\rho_{p_i}L_{p_i} + \sum_{i=1}^{N_p+1}\rho_{pc_i}\right) + \frac{1}{A_n}\left(\sum_{i=1}^{N_n}\rho_{n_i}L_{n_i} + \sum_{i=1}^{N_n+1}\rho_{nc_i}\right)\right\} + R_w\right]}
\end{aligned} \tag{B.10}
$$

here, m is defined as R_L/R. Thus, output power is estimated as,

$$
\begin{aligned}
P &= I^2 R_L \\
&= \frac{N(S_p^M - S_n^M)^2 (T_H - T_C)^2 \cdot \dfrac{m}{(1+m)^2}}{\left[\dfrac{1}{A_p}\Big(\displaystyle\sum_{i=1}^{N_p} \rho_{p_i} L_{p_i} + \sum_{i=1}^{N_p+1} \rho_{pc_i}\Big) + \dfrac{1}{A_n}\Big(\displaystyle\sum_{i=1}^{N_n} \rho_{n_i} L_{n_i} + \sum_{i=1}^{N_n+1} \rho_{nc_i}\Big) + \dfrac{R_w}{N}\right]}
\end{aligned}
\tag{B.11}
$$

The module efficiency is defined as:

$$
\eta = \frac{P}{Q} \tag{B.12}
$$

where P is output power obtained in Eq. B.11 and Q is the input heat flux which is expressed as [88].

$$
Q = N(\Delta T_{p_1} K_{p_1} + \Delta T_{n_1} K_{n_1}) + N(S_{p_1} T_{p_1} - S_{n_1} T_{n_1}) I - \frac{1}{2} N I^2 (R_{p_1} + R_{n_1}) \tag{B.13}
$$

K_{p_1} and K_{n_1} are the thermal conductances of the p_1 and n_1 elements, respectively. R_{p_1} and R_{n_1} are the electric resistances of the p_1 and n_1 segments, respectively. The efficiency is shown by combining Eq. B.11 and Eq. B.13 when $m = 1$ for the maximum output power,

$$\begin{aligned}\eta &= \frac{P}{Q} \\ &= \frac{\dfrac{N(S_p^M - S_n^M)^2(T_H - T_C)^2}{4R_{tot}^M}}{N(\Delta T_{p_1}K_{p_1} + \Delta T_{n_1}K_{n_1}) + N(S_{p_1}T_{p_1} - S_{n_1}T_{n_1})I - \dfrac{1}{2}NI^2(R_{p_1} + R_{n_1})}\end{aligned} \tag{B.14}$$

where R_{tot}^M is effective electrical resistance of 1-pair.

$$R_{tot}^M = \frac{1}{A_p}\left(\sum_{i=1}^{N_p}\rho_{p_i}L_{p_i} + \sum_{i=1}^{N_p+1}\rho_{pc_i}\right) + \frac{1}{A_n}\left(\sum_{i=1}^{N_n}\rho_{n_i}L_{n_i} + \sum_{i=1}^{N_n+1}\rho_{nc_i}\right) + \frac{R_w}{N}$$

To simplify Eq. B.14 by using Eq. B.10,

$$\begin{aligned}\frac{1}{\eta} &= \frac{N(\Delta T_{p_1}K_{p_1} + \Delta T_{n_1}K_{n_1}) + N(S_{p_1}T_{p_1} - S_{n_1}T_{n_1})\dfrac{(S_p^M - S_n^M)(T_H - T_C)}{2R_{tot}^M}}{\dfrac{N(S_p^M - S_n^M)^2(T_H - T_C)^2}{4R_{tot}^M}} \\ &\quad - \frac{\dfrac{1}{2}N\left(\dfrac{(S_p^M - S_n^M)(T_H - T_C)}{2R_{tot}^M}\right)^2(R_{p_1} + R_{n_1})}{\dfrac{N(S_p^M - S_n^M)^2(T_H - T_C)^2}{4R_{tot}^M}} \\ &= \frac{4R_{tot}^M(\Delta T_{p_1}K_{p_1} + \Delta T_{n_1}K_{n_1})}{(S_p^M - S_n^M)^2(T_H - T_C)^2} + \frac{2(S_{p_1}T_{p_1} - S_{n_1}T_{n_1})}{(S_p^M - S_n^M)(T_H - T_C)} - \frac{R_{p_1} + R_{n_1}}{2R_{tot}^M}\end{aligned} \tag{B.15}$$

The first term in Eq. B.15 can be reduced by using Eq. B.2 $\sim$ B.4,

$$
\begin{aligned}
\frac{4R_{tot}^{M}(\Delta T_{p_1}K_{p_1}+\Delta T_{n_1}K_{n_1})}{(S_p^M-S_n^M)^2(T_H-T_C)^2} &= \frac{4R_{tot}^{M}(\Delta T_pK_p^E+\Delta T_nK_n^E)}{(S_p^M-S_n^M)^2(T_H-T_C)^2} \\
&= \frac{4R_{tot}^{M}\left(\dfrac{K_p^E}{\displaystyle\sum_{i=1}^{N_p}\frac{\kappa_p^E L_{p_i}}{\kappa_{p_i}L_p}+\frac{2\kappa_p^E L_{sub}}{\kappa_{sub}L_p}}+\dfrac{K_n^E}{\displaystyle\sum_{i=1}^{N_n}\frac{\kappa_n^E L_{n_i}}{\kappa_{n_i}L_n}+\frac{2\kappa_n^E L_{sub}}{\kappa_{sub}L_n}}\right)}{(S_p^M-S_n^M)^2(T_H-T_C)^2} \\
&= \frac{4R_{tot}^{M}(K_p^M+K_n^M)}{(S_p^M-S_n^M)^2(T_H-T_C)} \\
&= \frac{4}{Z^M(T_H-T_C)}
\end{aligned}
$$

where, K_p^M and K_n^M are the effective thermal conductance of p-type and n-type legs respectively.

$$
K_p^M = \frac{K_p^E}{\displaystyle\sum_{i=1}^{N_p}\frac{\kappa_p^E L_{p_i}}{\kappa_{p_i}L_p}+\frac{2\kappa_p^E L_{sub}}{\kappa_{sub}L_p}}
$$

$$
K_n^M = \frac{K_n^E}{\displaystyle\sum_{i=1}^{N_n}\frac{\kappa_n^E L_{n_i}}{\kappa_{n_i}L_n}+\frac{2\kappa_n^E L_{sub}}{\kappa_{sub}L_n}}
$$

and Z^M is the module figure of merit which is defined as:

$$
Z^M = \frac{(S_p^M-S_n^M)^2}{R_{tot}^{M}(K_p^M+K_n^M)}
$$

Then, Eq. B.15 can be simplified as:

$$\begin{aligned}\frac{1}{\eta} &= \frac{4}{Z^M(T_H - T_C)} + \frac{2(S_{p_1}T_{p_1} - S_{n_1}T_{n_1})}{(S_p^M - S_n^M)(T_H - T_C)} - \frac{R_{p_1} + R_{n_1}}{2R_{tot}^M} \\ &= \frac{T_H}{T_H - T_C}\left[\frac{4}{Z^M T_H} + \frac{2(S_{p_1}T_{p_1} - S_{n_1}T_{n_1})}{(S_p^M - S_n^M)T_H} - \frac{(R_{p_1} + R_{n_1})(T_H - T_C)}{2R_{tot}^M T_H}\right]\end{aligned}$$

Therefore, the efficiency η is estimated as:

$$\eta = \frac{T_H - T_C}{T_H}\left[\frac{4}{Z^M T_H} + \frac{2(S_{p_1}T_{p_1} - S_{n_1}T_{n_1})}{(S_p^M - S_n^M)T_H} - \frac{(R_{p_1} + R_{n_1})(T_H - T_C)}{2R_{tot}^M T_H}\right]^{-1} \tag{B.16}$$

VITA

EDUCATION

University of Washington, Seattle, USA

Ph.D. Candidacy granted working on Dissertation, Mechanical Engineering

Dissertation: *Design of thermoelectric (TE) modules based on TE materials of high specific figure-of-merit and low-cost materials*

Advisor: Minoru Taya

Sungkyunkwan University, South Korea *February 2005*

M.S. in Mechanical Engineering

Thesis: *Modeling of energy based impact physics and its parallel computing using Linux cluster and MPI*

Advisor: Ja Choon Koo

Sungkyunkwan University, South Korea *February 2003*

B.S. in Mechanical Engineering

Thesis: *Kinematical design and analysis of giant stride*

Advisor: Ja Choon Koo

REPRESENTATIVE PROJECTS

Air Force Office of Scientific Research (AFOSR)-MURI 2007/09 - 2012/08

Energy harvesting/storage system (EHSS)

- Synthesis of nanostructured thermoelectric (TE) materials via advanced powder metallurgy processing route and micro/nano characterization
- Fabrication of TE generators: mono-leg based π-shape, segmented π-shape, and segmented linear-shape TE module
- Development of new integration method into the combustion engine system using Fe based shape memory alloy (Fe-SMA)
- Modeling and FEM analysis of integrated TE generator systems

Tokyo Institute of Technology 2010/09-2010/12

Foreign Young Researcher Program

- Analyzed nanostructures in bulk Mg_2Si alloys synthesized via (a) direct melting method and (b) high energy mechanical alloying followed by spark plasma sintering (using JEM-2011 for TEM and JEM-2100F for STEM, JEOL)

NASA-Jet Propulsion Laboratory 2006/09-2007/09

Spark Plasma Sintering (SPS) processing of thermoelectric materials

- Optimization of the processing route and sintering parameters of TE materials ($CoSb_3$, doped SiGe) by Spark Plasma Sintering (SPS) method
- Development of measurement apparatus for TE properties

Samsung Electronics 2005/03-2006/02

Reliability evaluation of linear compressor

- Modeling of linear compressor based on bond graph method, and program development for the prediction of resonant springs displacement

Korea Science and Engineering Foundation (KOSEF) 2003/03-2005/02

Development of advanced general-purpose computational mechanics system for large scale analysis

- Modeling of an impact physics via energy based bond graph method and comparison with conventional modeling scheme based on continuum mechanics theory
- Development of algorithm and code for numerical analysis of impact physics
- Design of Red Hat based Linux cluster and modification to parallel code by using MPI for parallel computing

Industrial-Educational Cooperation Center 2003/03-2004/02

Design of high efficient winch operated easily by aged people

- Design of foot-operating winch for aged people and kinematic analysis based on RecurDyn

TEACHING EXPERIENCE

Teaching Assistant, Mechanical Engineering, University of Washington

- Sustainable Energy Harvesting and Storage Materials and Systems(ME498) Fall 2011
- Finite Element Analysis (ME478) Summer 2011
- Kinematics and Dynamics (ME230) Spring 2011

Teaching Assistant, Mechanical Engineering, Sungkyunkwan University

- Computer Programming (MATLAB) for Engineer Spring 2004
- Computer Programming (MATLAB) for Engineer Fall 2003

LIST OF PUBLICATIONS

1. **H. S. Kim**, T. Itoh, T. Iida, and M. Taya, Design of linear shaped thermoelectric generator and self-integration using shape memory alloy, in preparation

2. **H. S. Kim**, K. Kikuchi, T. Itoh, T. Iida, and M. Taya, Design of segmented thermoelectric generator based on cost-effective and light-weight thermoelectric alloys, in revision

3. **H. S. Kim**, W. S. Liu, K. Kikuchi, and M. Taya, Thermoelectric properties of n-type magnesium silicide and numerical analysis of module device, *Proceedings of the 18th International Conference on Composite Materials*, Jeju Island, South Korea, Aug. 21-26, 2011

4. **H. S. Kim**, M. S. Choi, K. Kikuchi, and M. Taya, Optimization of thermoelectric modules based on Mg-Si system, *Proceedings of SPIE*, vol. 7288, 72881W2, 2009

5. J. C. Koo, **H. S. Kim**, J. B. Choi, and Y. J. Kim, Application of discrete Hamilton's equation for parallel processing of impact problems, *Key Engineering Materials*, Vol. 298, pp. 716, 2005